Scalable Printed Thermoelectric Generators

Zur Erlangung des akademischen Grades einer

Doktorin der Ingenieurwissenschaften (Dr.-Ing.)

von der KIT-Fakultät für
Elektrotechnik und Informationstechnik
des Karlsruher Instituts für Technologie (KIT)

angenommene

Dissertation

von

M.Sc. Irene Brunetti
geb. in Pisa

Tag der mündlichen Prüfung: 17.12.2024

Hauptreferent: **Prof. Dr. Uli Lemmer**

Korreferent: **Prof. Dr. Martijn Kemerink**

The work described in this thesis was performed between June 2021 and December 2024 at Innovationlab GmbH (Heidelberg, Germany) and Karlsruher Institut für Technologie with secondment at Istituto Italiano di Tecnologia (Milano) between September 2022 to December 2022 and at EURECAT Centre Technologic (Barcelona) between May 2023 to August 2023.

This thesis is part of the work developed within the HORATES Innovative Training Networks project (Marie Skłodowska-Curie Grant Agreement No. 955837) and therefore includes contributions from 6 Early Stage Researches (ERS) who form the Early Stage Researches team (Federico Ferrari, Nathan James Pataki, Matias Nicolas Joglar, Diego Ropero Hinojosa, Angus Hawkey, Aditya Dash). The specific contributions of each ESR are noted throughout the text.

Abstract

Advances in modern electronics have significantly reduced power consumption, paving the way for alternative energy harvesting (EH) to complement traditional batteries. With an estimated 50% of global energy consumption expected to be wasted as heat by 2030, the development of energy harvesting technologies that can convert this waste heat into usable energy is critical to addressing sustainability challenges. Thermoelectric generators (TEGs) are the ideal candidates, as they use the Seebeck effect to convert thermal energy into electrical energy. However, conventional manufacturing processes for TEGs are often expensive and environmentally unfriendly and rely on inorganic materials that are rare, limiting their widespread adoption.

Organic TEGs are emerging as a cost-effective and environmentally friendly alternative due to the good solution processability and abundance of organic materials in nature. Despite significant research into the thermoelectric (TE) properties of organic materials, their practical application within energy harvesting devices remains limited to proof-of-concept lab-scale devices, both for environmental instability, especially for the n-type materials, and absolute poor TE performance far behind the inorganic counterparts. However, recent advances in materials research have created the potential to implement these materials in application-specific devices, which is an important first step toward practical applications.

This thesis explores the development, characterization, and optimization of scalable, low-cost fabrication methods for organic-inorganic TEGs, focusing on the transition from lab-scale prototypes to large-scale production. First, a scalable method for fabricating vertical organic TEGs using industrial machinery is introduced, with device reliability validated through finite element simulations and scalability demonstrated by successfully printing up to 800 thermoelements. Second, the integration of a stable n-type ink into a scalable folded TEG architecture is presented, with performance aligning with numerical simulations. These devices exhibit record performance in the field of organic TEGs and deliver unprecedented stability in harsh environments, meeting the requirements for real-world applications. Finally, the integration of an inorganic scalable device with a vertical architecture and a low-cost, low-power start-up stage is demonstrated. The system effectively boosts the power generated by the printed TEG to drive conventional electronic devices in practical applications.

Kurzfassung

Fortschritte in der modernen Elektronik haben den Energieverbrauch erheblich reduziert und ebnen den Weg für alternative Energiegewinnungsmethoden (engl. Energy-Harvesting-Methoden, EH) als Ergänzung zu herkömmlichen Batterien. Angesichts der Prognose, dass bis 2030 etwa 50% des globalen Energieverbrauchs als Wärme verschwendet werden, ist die Entwicklung von Technologien zum Energy Harvesting, die diese Abwärme in nutzbare Energie umwandeln können, entscheidend für die Bewältigung von Nachhaltigkeitsherausforderungen. Thermoelektrische Generatoren (TEGs) sind dazu die idealen Kandidaten, da sie den Seebeck-Effekt nutzen, um thermische Energie in elektrische Energie umzuwandeln. Allerdings sind die herkömmlichen Herstellungsverfahren für TEGs oft teuer und umweltschädlich und basieren auf seltenen anorganischen Materialien, wodurch ihre weitverbreitete Anwendung eingeschränkt ist.

Organische TEGs gewinnen als kostengünstige und umweltfreundliche Alternative zunehmend an Bedeutung, da organische Materialien gut löslich und reichlich vorhanden sind. Trotz umfangreicher Forschung zu den thermoelektrischen (TE) Eigenschaften organischer Materialien bleibt ihre praktische Anwendung in Energy-Harvesting-Systemen auf Machbarkeitsstudien im Labormaßstab beschränkt, sowohl aufgrund der Umweltinstabilität, insbesondere der n-Typ-Materialien, als auch aufgrund der insgesamt schlechten TE-Leistung im Vergleich zu anorganischen Materialien. Jüngste Fortschritte in der Materialforschung haben jedoch das Potenzial geschaffen, diese Materialien in anwendungsspezifischen Geräten einzusetzen, was einen wichtigen ersten Schritt in Richtung praktischer Anwendungen darstellt.

Diese Dissertation untersucht die Entwicklung, Charakterisierung und Optimierung skalierbarer, kostengünstiger Fertigungsmethoden für organisch-anorganische TEGs und konzentriert sich auf den Übergang von Laborprototypen zu Großserienproduktionen. Zunächst wird eine skalierbare Methode zur Herstellung vertikaler organischer TEGs mit industriellen Verfahren vorgestellt, wobei die Zuverlässigkeit der Bauteile durch Finite Elementsimulationen validiert und die Skalierbarkeit durch den erfolgreichen Druck von bis zu 800 Thermoelementen demonstriert wird. Zweitens wird die Integration eines stabilen n-Typ Materials in eine skalierbare gefaltete TEG-Architektur präsentiert, deren Leistung mit numerischen Simulationen übereinstimmt. Diese Geräte zeigen

Rekordleistungen im Bereich der organischen TEGs und bieten außergewöhnliche Stabilität in rauen Umgebungen, wodurch sie die Anforderungen für reale Anwendungen erfüllen. Schließlich wird die Integration eines anorganischen, skalierbaren Bauteils mit einer vertikalen Architektur und einer kostengünstigen, energiesparenden Startphase demonstriert. Das System steigert effektiv die von den gedruckten TEGs erzeugte Energie, um herkömmliche elektronische Geräte in praktischen Anwendungen zu betreiben.

Contents

List of Publications and Contributions to Conferences

Publications in peer-reviewed journals

- **Brunetti, I**., Dash, A., Scheunemann, D., & Kemerink, M. (2024). Is the field of organic thermoelectrics stuck? Journal of Materials Research, 39(8), 1197–1206. https://doi.org/10.1557/s43578-024-01321-9.

- **Brunetti, I**., Ferrari, F., Pataki, N. J., Abdolhosseinzadeh, S., Heier, J., Koster, L. J. A., Lemmer, U., Kemerink, M., & Caironi, M. (2024). Fully Screen-Printed, Flexible, and Scalable Organic Monolithic Thermoelectric Generators. Advanced Materials Technologies. https://doi.org/10.1002/admt.202302058.

- **Brunetti, I**.* James Pataki*, N., Hinojosa, D. R., Hawkey, A., Karakaya, O., Rainer, C., Khan, M. I., Franke, L., Mallick, M. M., Hernandez-Sosa, G., Kemerink, M., Caironi, M., & Lemmer, U. (2024). A Scalable Fully Printed Organic Thermoelectric Generator for Harsh Environments Enabled by a Stable n-type Polymer. Advanced Materials Technologie. https://doi.org/10.1002/admt.202400968.

- M. Joglar*, **I.Brunetti***, Q.Zhang, L.Franke, A.G.Roesch, Md M.Mallick, A.Moya, U.Lemmer, & C.Delgado Simão. Printed TEG Based Energy Harvesting System Driven by Self-Powered Low-Power Oscillator. (in preparation)

- Franke, L., Georg Rösch, A., Khan, M. I., Zhang, Q., Long, Z., **Brunetti, I.**, Joglar, M. N., Lara, A. M., Simão, C. D., Geßwein, H., Nefedov, A., Eggeler, Y. M., Lemmer, U., & Mallick, M. M. (2024). High Power Density $Ag_2Se/Sb_{1.5}Bi_{0.5}Te_3$ Based Fully Printed Origami Thermoelectric Module for Low-Grade Thermal Energy Harvesting. Advanced Functional Materials. https://doi.org/10.1002/adfm.202403646

Conference contributions

- I. Brunetti, F. Ferrari, N. James Pataky, S. Abdolhosseinzadeh, J. Heier, J. A. Koster, U. Lemmer, M. Kemerink, M. Caironi. Flexible, Scalable, and Reliable Fully Screen-Printed Thermoelectric Generators. MRS Spring Meeting 2024, Seattle, USA. (oral presentation)

- I. Brunetti, F. Ferrari, N. James Pataky, S. Abdolhosseinzadeh, J. Heier, J. A. Koster, U. Lemmer, M. Kemerink, M. Caironi. Flexible, Scalable, and Reliable Fully Screen-Printed Thermoelectric Generators. Flexible, E-MRS SPRING MEETING 2024, Strasbourg, France (oral presentation)

Introduction

"Non temete i momenti difficili. Il meglio viene da lì"

Rita Levi Montalcini

1.1 Motivation

With the widespread of IoT (Internet of Things) devices, the demand for sustainable, cost-effective, and long-lasting power is crucial.[1,2] Energy Harvesting (EH) solutions are emerging as game changers to replace or more reasonably complement batteries in applications where portability, remote control, and power autonomy are critical. Photovoltaics, which harnesses solar radiation, are the most promising and extensively studied EH, achieving conversion efficiencies nearing 50%.[3] Although, as one would logically expect, their operation depends on sunlight. In dark scenarios, alternative solutions have to be examined to surmount this limitation. Piezoelectric and electromagnetic EHs represent viable alternatives,[4,5] wherever there is mechanical energy is available. However, these mechanical generators are composed of moving parts, and their maintenance is often critical, especially in harsh remote-control scenarios.

Another widely available source of energy is heat energy. Just consider that by 2030 is estimated that around 50% of global energy use will be wasted as heat.[6] The heat can be converted into electrical energy using thermoelectric generators (TEGs). The TEGs are free of mechanical parts; thus, they are silent, highly reliable, and require little maintenance compared to Piezoelectric and Electromagnetic EH.

TEGs are typically used in applications such as industrial processes, automotive applications, and remote sensors (including wearables) where sunlight and mechanical movements are not available or reliable. TEGs are particularly advantageous in situations where a temperature gradient is maintained, operating continuously as long as this temperature difference exists. The modularity, flexibility, and compactness of the TEG design, along with their ability to operate at low temperatures, allow the TEG to exploit small and local temperature differences, unlike other standard methods of generating energy from the heat, such as the Rankine cycle.[7,8] These characteristics make these devices very suitable for the IoT world.

The majority of TEGs are manufactured using known processes such as Bulk, Si-based, and MEMS (Micro-Electro-Mechanical System) techniques.

Bulk TEGs, the commercially available Peltier modules, are made by synthesizing high-quality thermoelectric materials, which are then cut, shaped, and doped into single elements to create individual p-type and n-type legs. These elements are afterward assembled with thermal and electrical interconnections and encapsulated to create the TEG modules.[9,10] The cost of producing these devices remains high, despite being already commercialized in mass production. This is due to high-purity materials and the complex, specific manufacturing techniques involved.

Si-based TEGs are made using CVD (Chemical vapor deposition), and ion implantation to create the thermoelectric legs TEG. These techniques are easy to integrate into widespread and well-consolidated complementary metal-oxide-semiconductor (CMOS) technology.[11,12] Typically, poly-Si and poly-SiGe are used in the fabrication of the CMOS-based TEG, due to their reasonable thermoelectric performance. However, the high thermal conductivity of Silicon remains the main limiting factor in exploiting this technology.

MEMS (Micro-Electro-Mechanical Systems) TEGs are often deposited by physical vapor deposition (PVD) and CVD, and typically the fabrication process involves photolithography, dry etching, liftoff, and shadow masks, leading to a high production cost. [13,14]

Alternative to the standard fabrication electronic techniques described above industrial printing techniques are emerging methods for fabricating TEGs.[15–17] These techniques are characterized by low-temperature, vacuum-free (or vacuum-less in some cases), cost-effective equipment, minimal material waste, and the possibility to use sustainable substrates and materials. However, not all materials can be printed. Solution-processable inks with specific rheological properties,[18,19] which vary for each printing technique, are necessary for proper drop generation and to achieve the desired resolution and pattern. Nowadays, the most widespread printing techniques are inkjet printing, screen printing, aerosol jet printing, and direct ink writing (DIW). The main differences between these techniques are production time, printing resolution, and specific requirements of the inks, as described below. Using these new methods to fabricate TEGs boosts the exploration of new cost-effective, flexible conformal, low-weight, and customizable architectures ideal when the heat sources have a curved or irregular surface, such as human skin, demanding TEGs that are conformal, flexible, low-weight, and customizable. These devices could provide a complementary source of energy where other forms of energy generation cannot meet the requirements.

Currently, inorganic materials outperform organic materials in terms of energy generation efficiency.[20] The most used printable inorganic materials for fabricating TEGs are certainly $(BiSb)_2(TeSe)_3$-based,[21] which perform best at medium-temperature gradients (below 450 K) and are among the most suitable to make inks. However, promising chalcogenides Ag_2Se and Cu_2Se have also demonstrated good printability and reasonable performances.[22] Bi, Se, and especially Te have a rare crustal abundance of 0.18,[23] 0.13[23] and 0.001[24] ppm, respectively, and their extraction, processing, and disposal can pose environmental risks. Furthermore, Te and Bi in low to medium concentrations and Se in high concentrations are toxic to humans. These factors limit their mass production in light as societies move towards environmental sustainability.

Printable inorganic materials are still less efficient than bulk materials due to the presence of binders, additives, and solvents that cause high interfacial resistance among the TE particles.[22] Compared to the bulk materials the TE-printed films are less brittle and can be bent slightly, but they are still not as flexible as their organic counterparts.

The organic materials are easily compatible with solution-based fabrication techniques and are ideal candidates for printing flexible, stretchable, and sustainable TEG. Their processability allows for the development of cost-effective devices with diverse architectures, capable of exploiting all thermal gradients by tailoring them for each heat source, ensuring optimal thermal matching.[25–27] However, as anticipated, the thermoelectric performance is significantly lower compared to inorganic materials.

Prototypes of organic TEG with an output power density ranging from 10 to 100 μW cm^{-2},[28] which is required for most IoT technologies, have yet to be realized in practical applications.

Nowadays the research in the organic community is primarily focused on enhancing material performance, aiming to bridge the gap with inorganic counterparts by synthesizing new materials and improving doping quality. While studying the properties of materials is undoubtedly important, it remains distant from practical application.

Recent advancements in organic semiconductors, doping, and processing techniques, are starting to pave the way for application-oriented organic TEGs.[29–31] Nevertheless, the current constraints have limited examples of fully printed organic TEGs to just a few studies, primarily serve as benchmarks for material properties, and are often characterized by low thermocouple density and fill-factor (*FF*) unsuitable for efficient energy harvesting.

There is a need for TEG architecture made using scalable, solution-based deposition techniques that provide high power density, compatibility with various TE active materials, and predictable performance. This demand is becoming even more urgent as new, high-performance organic materials, such as the recently discovered poly(benzodifurandione) PBFDO,[32] are developed and scaled up.

Simultaneously there is a need for the development of suitable low-cost electronics capable of stepping up the low power generated by these devices to minimize the required area and temperature difference. The implementation of a start-up stage is necessary to minimize the minimum input voltage and to power conventional electronic devices.

1.2 Scope of this work

This thesis aims to bridge the gap between not-scalable poorly defined demonstrators to scalable, predictable organic TEGs that could be used for energy harvesting prototyping systems. Specifically, it aims to present new fully printed TEG architectures that are compatible with various printable inks without the use of time-consuming and costly extra-processing steps together with a low-power cost-effective electronic. Large-area techniques will be used to develop prototypes that are close to industrial-scale production taking into account the trade-offs between material performance, manufacturing techniques, and device design. To overcome these challenges, the development of materials and device concepts must carefully reevaluate their compatibility with the manufacturing process.

The scope of this thesis is outlined in the following chapters, which briefly describe the objectives of each section:

- Chapter 2: provides an overview of thermoelectric phenomena through a description of the fundamental thermoelectric parameters: Seebeck coefficient, electrical conductivity, and thermal conductivity. Additionally, it presents the current state of the art in organic thermoelectric materials and solution-processable inorganic materials.
- Chapter 3: gives a background to understand the fundamental principles of a thermoelectric generator and the influence of design parameters on its performance. It describes the fabrication methods employed in this thesis, screen printing and inkjet printing, and the properties that the inks should have for good printability in both cases. Lastly, it presents the current state of the art in printed thermoelectric generators.
- Chapter 4: outlines the development of a scalable method for fabricating vertical organic thermoelectric generators using industrial machinery. The reliability of the devices is validated through finite element simulations, and scalability is demonstrated by successfully printing devices with up to 800 thermoelements.
- Chapter 5: aims to demonstrate the use of the recently reported PBFDO n-type polymer alongside the PEDOT:PSS p-type polymer in a scalable thermoelectric generator. The performance is compared with finite element simulations, and the device is tested under harsh environmental conditions to assess its suitability for real-world applications.
- Chapter 6: investigates a cost-effective, custom energy harvesting system, comprising a scalable inorganic thermoelectric generator and a custom start-up electronic circuit. The aim is to demonstrate its potential for practical applications, with future readiness for integration with organic thermoelectric generators.
- Chapter 7: summarizes the key findings of this work and provides an outlook for future studies on improving the performance of organic thermoelectric generators and energy harvesting systems.

2.1 Fundamental of Thermoelectrics

This chapter will describe the basic thermoelectric parameters for band-like conductive materials and amorphous materials. The basic interrelated parameters relevant to thermoelectric power generation are the Seebeck coefficient (S), electrical conductivity (σ), and thermal conductivity (k). Describing these parameters analytically for amorphous materials (most printed semiconductors) is challenging. Additionally, it will analyze the Figure of Merit (FoM): Power Factor (PF) and zT and describe the state of the art of organic materials and printed inorganic materials.

The analysis of the state of the art of organic materials has been previously published as a journal article in the Journal of Materials Research.[33,a]

2.2 Boltzmann transport equation

Generally, the charge and heat transport in solid semiconductors and conductors can be described by the electrical (j) and thermal (j_q) current density using the Boltzmann transport equation:[34]

$$j \ = L_{11}\,\varepsilon + L_{12}(-\nabla T) \tag{2.1}$$

$$j_q \ = L_{21}\,\varepsilon + L_{22}(-\nabla T) \tag{2.2}$$

Where $\varepsilon = E + \nabla\mu/\mathrm{q}$ is the electric field (electrostatic field and the gradient of the electrochemical potential), and ∇T is the temperature gradient. For band conduction, we can evaluate from the Boltzmann transport equation the parameters L as a function of three tensors $\boldsymbol{\mathcal{L}}_\alpha$ with the relaxation time approximation hypothesis (the system returns to equilibrium after a characteristic time, τ):[35]

$$L_{11} = \mathcal{L}_0 \tag{2.3}$$

$$L_{21} = TL_{12} = -\frac{1}{q}\mathcal{L}_1 \tag{2.4}$$

$$L_{22} = \frac{1}{q^2T}\mathcal{L}_2 \tag{2.5}$$

$$\mathcal{L}_\alpha = \int dE\left(\frac{df}{dE}\right)(E - E_F)^\alpha\sigma(E) \tag{2.6}$$

---

[a] collaboration with M.Sc.Aditya Dash, Dr. Dorothea Scheunemann, Prof. Dr. Martijn Kemerink. (Institute for Molecular Systems Engimeering and Advanced Materials, Heidelberg Germany).
Partner of the Horates project.

Where q fundamental charge, E_F is the Fermi level, f is the fermi-Dirac distribution $f = [1+\exp(E-E_F/k_BT)]^{-1}$, and σ(E) is the transport function:

$$\sigma(E) = \frac{q^2}{4\pi^3}\int \tau(E)\, v(k)v(k)\delta(E - E(k))dk \tag{2.7}$$

Where τ is the relaxation time, and v is the electron velocity.

Knowing the σ(E) it is possible to evaluate all the thermoelectric parameters since:

$$\sigma = L_{11} \tag{2.8}$$

$$S = \frac{L_{12}}{L_{11}} \tag{2.9}$$

$$k_0 = L_{22} \tag{2.10}$$

It has been demonstrated that these relationships are generally true, regardless of the transport in disordered semiconductors where the relaxation time approximation is not valid.[36,37] The following sections describe each parameter in more detail, starting with a conceptual description and progressing to a more detailed one.

2.3 Electrical conductivity

The electrical conductivity σ is a measure of the ability of the materials to conduct electrical current. It can be expressed as follows:

$$\sigma = \frac{j}{E} \tag{2.11}$$

Where j is the current density, and E is the electric field. Following Drude's model and assuming that there is only one type of moving charge q under the action of an electric field, the carriers are accelerated by a force $F=eE$ for a time τ, and the current density can be defined as:

$$j = q\frac{e\tau}{m}nE \tag{2.12}$$

Where n is the density of carriers. Hence, the conductivity can be described by:

$$\sigma = q\frac{e\tau}{m}n = q\mu n \tag{2.13}$$

Where μ is the carrier mobility, and it is a measure of the velocity of charge carrier motion in the material when an electric field is applied. Making qualitative assumption, the conductivity is proportional to the density of the electrons, not surprising since the higher the number of carriers, the more the current density. The conductivity is also inversely proportional to the mass since the mass is inversely proportional to the acceleration of the charge in an electric field. The μ is generally related to the morphology of the materials, while n can be tuned with doping.

In a more realistic and extended description, the μ and n depend on the band structure, the transport mechanism, the physical condition (i.e. temperature) of the materials, and the presence of a crystal, as well as defects and impurities, which can scatter carriers and limit their dispersion.

A general expression for the conductivity can be derived from the Boltzmann transport equation (see equations 2.6,2.7,2.8) in a relaxation-time approximation:[38]

$$\sigma = \int_{-\infty}^{\infty} \sigma(E)(-\frac{df}{dE})\, dE \tag{2.14}$$

Where $\sigma($E) is the transport function described by equation 2.7. $\sigma($E) has the same unit of electrical conductivity and depends on various factors such as the doping transport model, the applied force, and doping concentration.

In an isotropic metal-like conductor material the transport function corresponds to:[39]

$$\sigma(E) = \frac{e^2}{3}\tau(E)v^2(E)g(E) \tag{2.15}$$

Where the $g(E)$ is the density of the state. For a single parabolic band model $g(E)$ is proportional to $E^{1/2}$, τ is often considered proportional to $E^{-1/2}$(case of phonon scattering), and v^2 scale with E. Hence, $\sigma($E) scales proportionally with E.[40] By considering -df/dE as a selection function we can qualitatively describe equation 2.14 for a metal-like conductor. In a Metal -df/dE is a delta function center in the fermi level, well above the transport edge, and it selects the transport function in a range of $4k_BT$ around the fermi level (Figure 2.1a). Whereas in a doped semiconductor, the fermi level is just above the band edge, and the band edge has the function of cutting out the carrier usually would take part in the conduction (Figure 2.1b).

Considering τ only dependent on energy, the electrical conductivity can be described as:

$$\sigma = \frac{e^2}{3}(gv^2\tau)_{E=E_F} \tag{2.16}$$

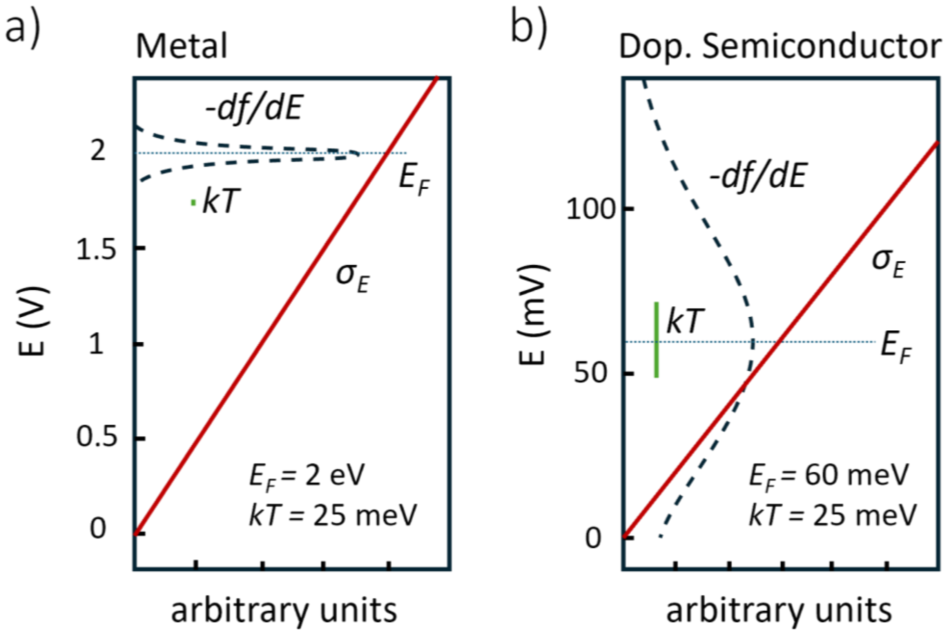

Figure 2.1: a) Energy dependence of the transport function (red line) and the selection function (blue dotted line) for a metal. b) Energy dependence of the transport function (red line) and the selection function (blue dotted line) for a doped semiconductor.

Using the parabolic dispersion and the effective mass $m*$, it became:

$$\sigma = \frac{n\,e^2\tau}{m^*} \tag{2.17}$$

It resulted in the Drude expression for $m^* = m$. For a more detailed derivation refer to.[41]

The time approximation is not generally valid for disordered materials, such as organic semiconductors, however, H. Fritzsche[36] showed that equations 2.2 and 2.14 are valid regardless of the transport mechanism. It should be remembered that the main difference in charge transport in amorphous organic materials compared to crystal inorganic semiconductors and metals is that the carriers are not delocalized in the solid but are fully or partially localized. This precludes band conduction, the carriers rather move by a thermally activated tunneling process known as hopping. Establishing an analytical unique expression to describe the electrical conductivity of this class of materials is a nearly impossible task, given their spectrum of morphological possibilities, ranging from ordered molecular crystallites to semi-crystalline solids to near-amorphous polymers. A more detailed analysis can be found in the available literature.[34,42,43] These works present different models, the Mott-Martens/Zuo,[44,45] the Schmechel-Ihnatsenka,[46,47] and the Kang-Snyder.[43]

2.4 Seebeck coefficient

In a thermodynamic system, ideal and closed, subjected to an external temperature gradient, the uncharged mobile particles are subject to a steady drift. The hot particles have a higher average mean velocity than the cold particles. Hence, the hot particles have longer free paths than the cold ones, leading to a higher concentration of particles at the cold end by establishing a gradient. This phenomenon is known as the Soret effect or thermophoresis.[48] When this process occurs in a system with charged particles, the gradient will produce a repulsive electrostatic force and, consequently, an electric potential, that drives the charges back toward the hot end, developing a dynamic equilibrium with a zero net flux of the charged particles. This phenomenon called the thermoelectric effect, was discovered through the observation of a current resulting from the difference in electrostatic forces of two metals when their junctions were kept at different temperatures.[49]

For a single material, the ratio between the voltage generated (or thermal voltage ΔV) and the temperature difference (ΔT) applied to the materials is the S, and can be described as:

$$S = -\frac{\Delta V}{\Delta T} \tag{2.18}$$

The negative sign is due to the convention that the electric field points in the direction of decreasing electric potential. Thus, if the majority of the carriers in the materials are holes (p-type material) there will be a positive charge at the cold end and S will be positive, while if the carriers are mainly electrons (n-type material) there will be a negative charge at the cold end and the S will be negative.

The S (or thermopower) is an intrinsic property of the material, and it is connected to the entropy of the charge carriers in a material with a temperature gradient. Charge carriers move from the hot side (high entropy) to the cold side (low entropy) of the material, creating a steady-state voltage.

The classic theory does not explain why several metals, such as silver, gold, and aluminum which are known to be electron conductors, have a positive Seebeck coefficient. This discrepancy is due to the application of the free electron gas model, which does not consider the band-dependent effective mass (m^*) of the particles.

As anticipated in the previous section, the Seebeck coefficient can be described macroscopically, derived from the Boltzmann equation in the relaxation time approximation[38] (equations 2.6-2.9-2.7) independently from the transport process (H. Fritzsche[36]), with the following formula:

$$S = -\frac{1}{qT}\int (E - E_F)\frac{\sigma(E)}{\sigma}\left(-\frac{df}{dE}\right)dE \; = -\frac{1}{qT}\int (E - E_F)\frac{\sigma'(E)}{\sigma}dE \qquad (2.19)$$

In this case, the selection function is (E-E_F)(-df/dE) and has a dipole moment shape (see Figure 2.2).

In a metal, since the fermi level is deep inside the band, the dipole moment induces the cancellation between the carrier below and above the fermi level, minimizing the value of the S. This is the reason why, despite their high electrical conductivity, these materials are not considered effective thermoelectric materials.

In a doped semiconductor, where the Fermi level is just above the band edge, the multiplication of the transport function and the selection function results in one lobe being larger than the other, maximizing the value of S (Figure 2.2). These materials are considered the best TE materials, as they exhibit a trade-off between the σ and S.[40]

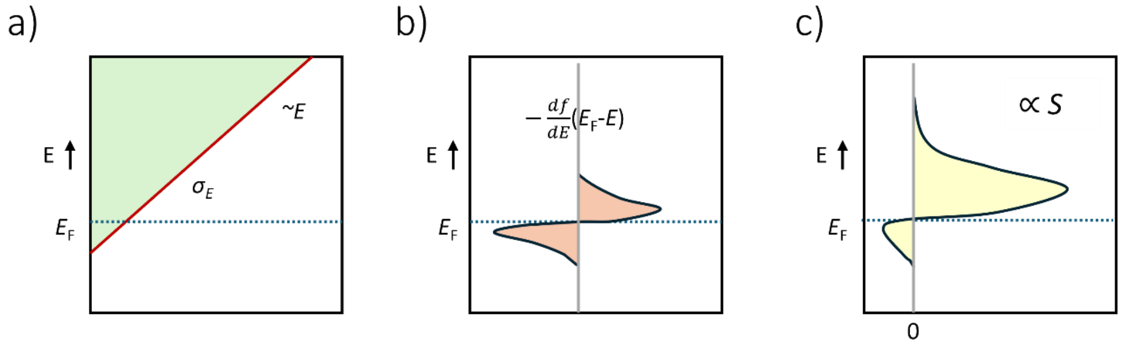

Figure 2.2: a) Energy dependence of the transport function for a doped semiconductor. b) Selection function of the Seebeck coefficient. c) Product between the transport function and the selection function. The yellow area is proportional to the Seebeck coefficient. The blue dashed red line represents the Fermi level.

In an isotropic metal-like conductor (parabolic band and simple phonon scattering), the current is determined only by the carriers with energies near E_F, and equation 2.19 can be simplified using the Sommerfeld expansion:[50]

$$S = -\frac{\pi^2 {k_B}^2 T}{3q}\frac{d}{dE}\ln\left[\sigma(E)\right]\Big|_{E=E_F} = \frac{8\pi^2 {k_B}^2}{3qh^2} m^* T\left(\frac{\pi}{3n}\right)^{\frac{2}{3}} \qquad (2.20)$$

In which h is the Planck constant. This formula is known as the Mott expression It is possible to note that S is inversely proportional to the n, therefore extremely high charge carrier densities are responsible for a low S value, another way of seeing the trade-off between the S and the σ.

Equation 2.20 is also valid for inorganic crystalline semiconductors but cannot usually be used in hopping systems (large amounts of printable semiconductor materials).

In a system where the E_F is far from the energy of the mobile charges, and only delocalized states over a specific mobility edge E_C contribute to the charge transport (narrow-band materials), the $\sigma(E)$ can be approximated with a step function where $\sigma(E)$ is 0 for $E < E_F$ and constant for $E \geq E_C$. Since the derivate ($\sigma'(E)$) of the step function is a Dirac delta ($\sigma'(E) = \theta\ (E-E_C)$), the Seebeck coefficient in disordered or amorphous materials can be expressed as:[34,43,50]

$$S = -\frac{E_C - E_F}{q\,T} + A \qquad (2.21)$$

Where A is a constant that depends on the conductivity distribution function (A is often ignored). In these systems, simplifying, the Seebeck coefficient is therefore proportional to the distance of the Fermi level from the band.

2.5 Thermal conductivity

The thermal conductivity k is a measure of the ability of the materials to conduct the heat. Heat can be defined as the transfer of thermal energy from one particle to its neighboring, where the thermal energy is defined by the microscopic vibration of the particles. In general, heat transfer can occur by radiation, convection, or conduction, but it has been shown that conduction is the main mode of heat transfer in solid materials. In solids, heat is carried by both lattice vibrational waves (phonons) and free electrons. Therefore, the total thermal conductivity can be defined as:

$$k = k_{lat} + k_{el} \tag{2.22}$$

Where the k_{lat} and k_{el} are the thermal conductivities due to the lattice vibration (phonons) and due to the electron, respectively.

In a crystalline material, k_{lat} derives from the vibrational wave-like aspect of the phonon transmitted through the structures, which move from a high to a low-temperature zone. Generally, k_{lat} can be described with the Debye equation:

$$k_{lat} = \frac{C_p\, v\, l}{3} \tag{2.23}$$

Where C_{p} is the volumetric heat capacity, v is the average phonon velocity, and l is the phonon mean free path.

Instead, the k_{el} is due to the free electron motion. The electrons on the hot side acquire kinetic energy and diffuse toward colder areas, where they collide and transfer some of their kinetic energy to the atoms as vibration. This contribution becomes more pronounced as the number of free electrons increases.

Metals are known to be good heat conductors; indeed their thermal conductivity is generally very high (hundreds of W/mK). In metals, the electrons are not easily scattered and have higher velocities, therefore their contribution to the total thermal conductivity (k) is much bigger than the contribution of the phonons. The electrons in this case are responsible for both electrical and thermal conduction, and the two conductivities are proportional to each other, following the Wiedemann-Franz law:

$$L = \frac{k_{el}}{\sigma T} \tag{2.24}$$

Where T is the absolute temperature, and L is the Lorentz number. This formula can also be derived once again from the Boltzmann equations in a relaxation-time approximation:

$$k_0 = \frac{1}{q^2 T}\int (E - E_F)^2\, \sigma(E)\left(-\frac{df}{dE}\right)dE \quad \text{with} \quad k_{el} = k_0 - S^2\sigma T \tag{2.25}$$

Where k_0 represents the electrical thermal conductivity when there is no electrochemical potential gradient inside the sample. In metal-like conduction, analogous to the conditions described for the calculation of the Seebeck coefficient and the electrical conductivity, the fermi level is deep inside the band and *df/dE* is negligible except for a small region around E_{F}. Thus, k_{el} can be expressed with the Sommerfeld expansion: [41]

$$k_{el} = \frac{\pi^2}{3}\left(\frac{k_B}{q}\right)^2 \sigma T + o\left(\frac{k_B T}{E_F}\right)^2 \tag{2.26}$$

Neglecting the second term, the $k_{el} = L_0\sigma T$, where the Sommerfeld value L_0 is 2.44×10^{-8} Ω W/K^2 and is similar to the Lorentz number described by equation 2.24.

In this case, the selection function is $(E\text{-}E_F)^2(\text{-d}f/\text{d}E)$. As shown in Figure 2.3 (for the case where the Fermi level is just above the band edge), the two lobes combine, and the k_{el} is closely related to the σ (see Figure 2.1).

For amorphous materials, the typical situation is represented by $k_{lat} >> k_{el}$. Furthermore, it must be considered that due to the structural disorder, the thermal energy will not propagate fast toward the material (Figure 2.4). Most of the initial kinetic energy is dissipated into the atoms of the disordered structure, causing k values advantageously low.

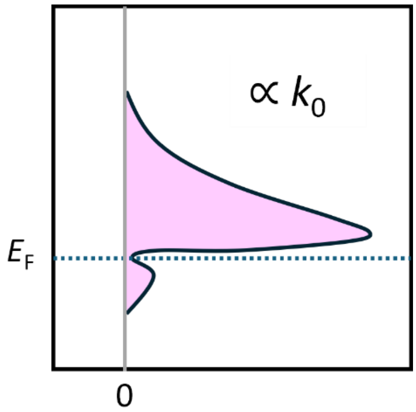

Figure 2.3: Product between the transport function and the selection function. The purple area is proportional to the electrical thermal conductivity. The blue dashed red line represents the Fermi level.

Scheunemann et al.[37] demonstrated that equation 2.25 is in good agreement with the k_{el} of disordered organic semiconductors experimentally measured. However, for this class of materials, the Lorenz number can be very different from the Sommerfeld value, and it can range over quite a wide range of values, depending on the localization length, energetic disorder, and carrier concentration.

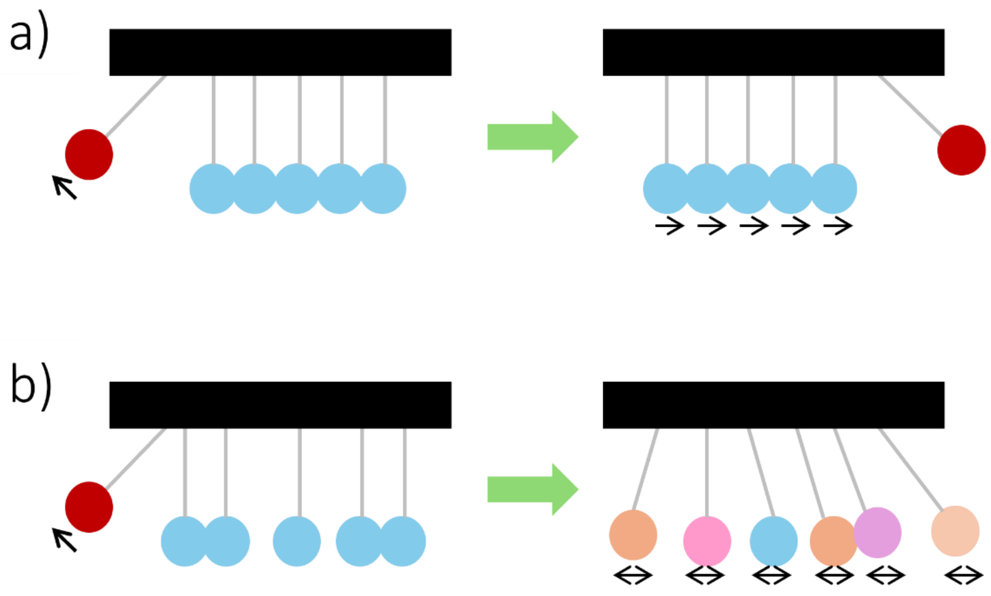

Figure 2.4: Comparison between the thermal energy propagation in a) crystalline materials and b) polymers, using the Newton pendulum analogy.

2.6 Thermoelectric materials figure of merit

As discussed previously Seebeck, electrical conductivity and thermal conductivity depend on the same transport function σ(E) and are strictly correlated with each other. To take this dependence into account, a general Figure of Merit (FoM) used to evaluate the quality of the TE materials is the dimensionless zT:

$$zT = \frac{\sigma S^2}{k} T = \frac{PF}{k} T \tag{2.27}$$

Where PF is the power factor. The zT of the material is related to the maximum efficiency of the thermoelectric device (TEG) figure of merit ZT.

The maximum efficiency of a material is often described as:

$$\eta_{max} = \frac{\Delta T}{T_h} \frac{\sqrt{1+zT}-1}{\sqrt{1+zT}+1} \tag{2.28}$$

Where the first term is the Carnot efficiency $\Delta T/T_h$ and the second term is a factor smaller than 1, that tends to 1 when zT approaches infinity.[51] To maximize the zT parameter, the S and the σ (PF) must be maximized, while the k should be minimized, as shown in Equation 2.27. In detail, S should be maximized to enhance the conversion of heat into electric power, while, the σ should be maximized to reduce the resistance of the device and minimize Joule heating, thereby maximizing electric power. Additionally, k should be minimized to avoid thermal shorting and maintain a large ΔT between the hot and cold sides, maximizing the power as well.

The Thermoelectric materials should behave as electrical conductors but as thermal insulators, a challenging condition as explained in the previous sections. In metal-like conductors S and σ generally have an opposite trend with respect to the density of carrier n (equations 2.17 and 2.20). Furthermore, when the k_{el} is dominant, k increases as n increases. Figure 2.5 shows the behavior of S, σ, k as a function of the carrier density concentration. All the TE parameters associated with zT are functions of n, leading to an optimal zT value at a specific n, suggesting that doped semiconductors (carrier concentration 10^{19}-10^{20}) are the best candidates. These materials have the E_F near the band edge, as discussed graphically in the sections above.

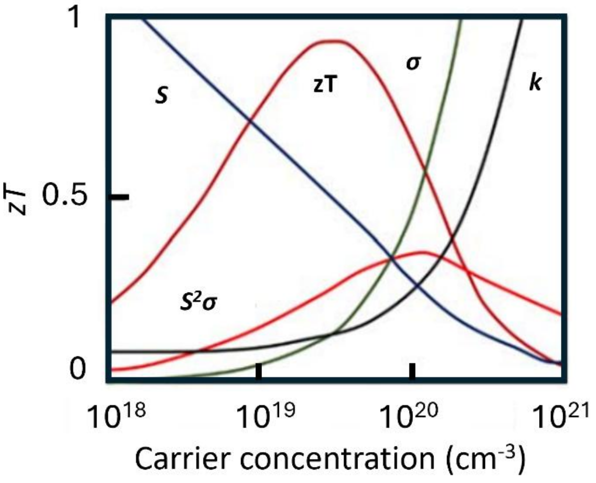

Figure 2.5: Variation of the TE parameters S, σ, and k as a function of the carrier concentration. The red and light red curves represent the zT and PF ($S^2\sigma$). Figure adapted from[52] Licence BB-CY.

Advancements in band structure engineering, microstructural design, novel doping processes, and nano-structuring techniques[53] have enabled the attainment of zT values of inorganic doped semiconductors (p-type) exceeding 2 (around 700 °C).[54]

As a general rule, zT should be around 1 to consider the materials relevant for application.[55] Furthermore, as can be seen in Figure 2.5, the peak of the zT is not in correspondence with the peak of the *PF* but is shifted towards a metallic zone because the *PF* ignores the increase of $k_{el.}$

For organic conductors, as explained in the previous chapters, the situation is somewhat different, since describing charge transport in these systems is not trivial. This is due to the range of possible morphologies, from ordered molecular crystals to semi-crystalline solids and near-amorphous polymers. Furthermore, it is very difficult to calculate the carrier density because Hall measurements are not reliable in localized systems. In general, however, it can be said that in organic materials, as in inorganic materials, the conductivity generally increases monotonically with increasing doping concentration, and hence with increasing carrier concentration, while the Seebeck coefficient decreases monotonically with it. As shown in these qualitative works using PEDOT:PSS poly(3,4-ethylenedioxythiophene): poly(styrenesulfonic acid) (used in this thesis in Chapters 4 and 5), PEDOT:Tos, and doped P3HT, which are among the most commonly used organic semiconductors.[56–58]

An even broader consideration can be made by examining the trend of the Seebeck coefficient *versus* electrical conductivity, without knowing the value of the carrier density. Glaudell et al.[59] (Figure 2.6) discovered a universal trend for p-type organic semiconductors, expanded for n-type materials by others,[59,60] whereby the *S* can be expressed as:

$$S = \frac{k_B}{q}\left(\frac{\sigma}{\sigma_\alpha}\right)^{-\frac{1}{4}} \tag{2.29}$$

Where σ_α is an unknown constant conductivity independent of carrier concentration (fitting parameter). The surprising correlation between *S* and σ, $S \alpha \sigma^{-1/4}$, valid for different polymers and dopants, seems to indicate that the transport is mainly dominated by the polymers themselves rather than by the specific doping methods.

Since $S \alpha \sigma^{-1/4}$, and thus the $PF \alpha \sigma^{-1/2}$, the *PF* is maximized when the σ is maximized. However, it has been demonstrated this is not always true, as seen in PEDOT-based materials.[56,57] In these cases, the maximum *PF* is observed for a specific value of σ. Additionally, it seems that some polymers with high conductivities (e.g. in Figure 2.6 for $>10^2$-10^3 S/cm) deviate moderately from this trend.

Multiple models have been proposed to explain the trend of S *versus* σ, e.g., in terms of transport edge and transport parameter s (without any specific physical meaning) by Kang and Snyder,[43] and in terms of hopping by Zuo et al.[42]

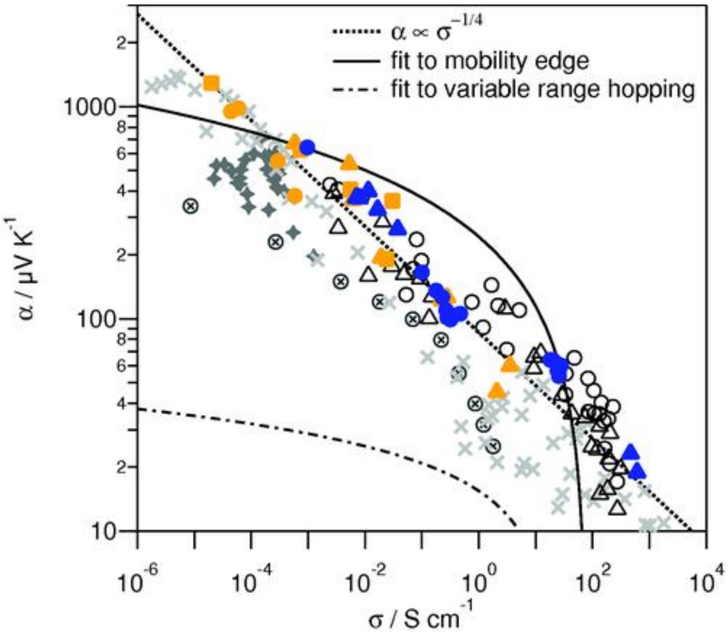

Figure 2.6: Seebeck coefficient (here represented by α), and electrical conductivity of various p-type polymers and dopants. Figure reprinted from[59] Licence CC-BY.

To maximize the zT, we have to consider the thermal conductivity k, a property that has not yet been thoroughly studied. Below we briefly present two studies that focus on theoretical and experimental analysis of the k of organic materials. In the first, Scheunemann et al.[37] demonstrated that weakly disordered organic materials with a high carrier concentration (high σ) show a lower Lorenz number, minimizing the k_{el}. Even though, in this class of materials, as explained earlier, k_{lat} dominates k_{el}, so k_{el} does not have much influence on the value of k, however, k_{el} will dominate as electrical conductivities increase, which is necessary for the material to be used effectively in applications. In the second, Rodrigueez-Martinez et al.[61] described a detailed analysis of k of several polymers, in which the k_{lat} is dominant, by providing specifically designed rules for minimizing (or maximizing) the k of the polymers. In long-range ordered polymers the charge and thermal transport are closely correlated, k increases with stiffer backbones, higher molecular weights, and heavier repeat units. Instead, in amorphous polymer the k the thermal and charge transport seems to be decoupled, since the k is decreasing with the μ. Suggesting further studies on stable and more effective doping of short-range ordered polymers, which could bring a real advancement in the organic thermoelectric field.[61]

2.7 State of the art of organic materials

Although the more complete figure of merit (FoM) to describe thermoelectric materials is the zT factor (Equation 2.17), the discussion will initially be limited to the analysis of the power factor (PF) (Equation 2.27), not taking into account the k. This is due to a lack of data points resulting from the difficulties in measuring and the absence of standard methods to measure the k in thin films, common in the field of solution-processable materials.

The International Network on Hybrid and Organic Thermoelectrics created an up-to-date open-access database, with the most relevant n-type and p-type organic TE materials.[62] To summarize the status (2024) and the trends over the past years of organic TE materials, we reported figures of the S, σ, and PF *versus* the years of publication for p-type (black squares) and n-type organic materials (red squares).[33] Analyzing the p-type (Figure 2.7a-c), we can surprisingly notice that the PF is not showing any upward trend over time, despite the growing interest (and increasing number of publications) in organic TE. The σ appears to be limited below a certain threshold, whereas the S shows a trend that, with some optimism, could be regarded as increasing sing. On the other hand, the PF is not increasing, suggesting that the well-known relation between S and σ, $S \; \alpha \; \sigma^{-1/4}$ is once again observable (Figure 2.8a), and as a consequence also the $PF \; \alpha \; \sigma^{-1/2}$ (Figure 2.8b). The best σ of the n-type materials are on average almost an order of magnitude lower than the p-type counterpart (Figure 2.7d-f). Indeed, the PF of the n-type is in the same range as that of the p-type, suggesting that the reduction in conductivity is compensated by higher Seebeck coefficients.

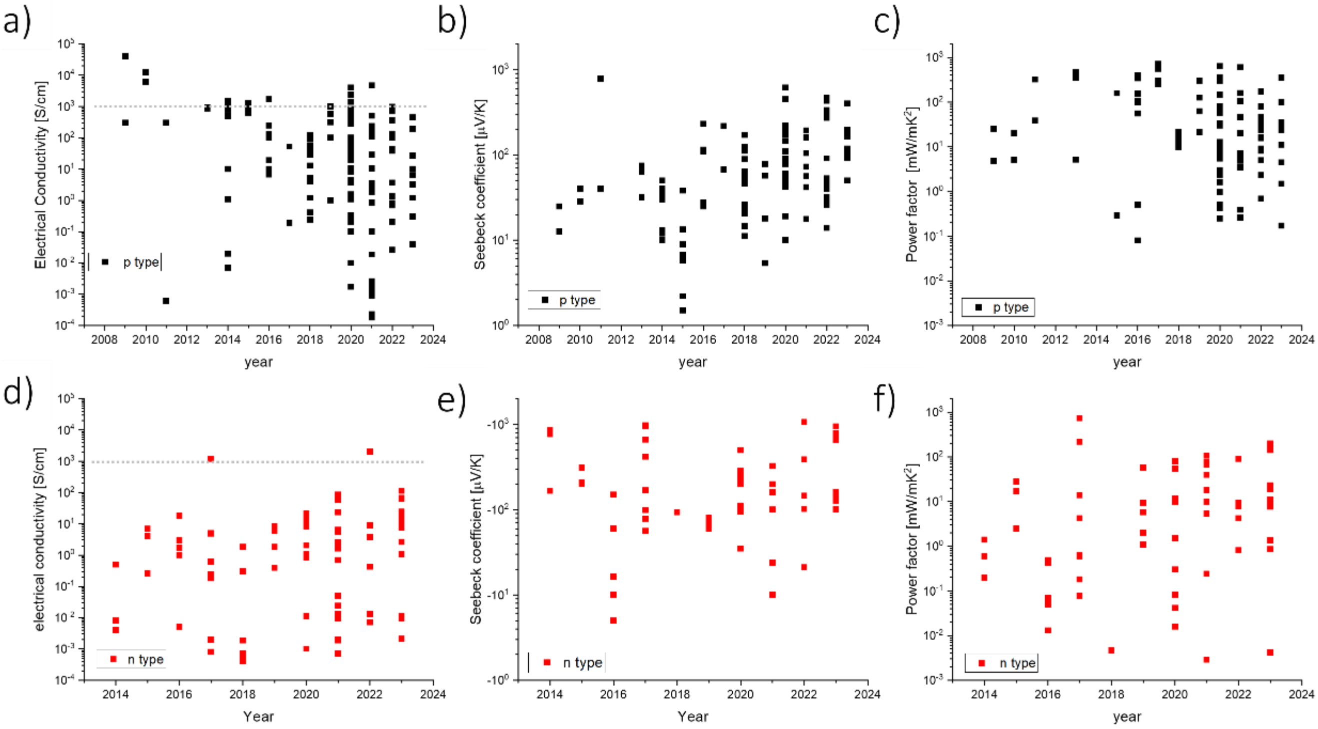

Figure 2.7: a) Electrical conductivity b) Seebeck coefficient c) Power factor of p-type organic materials as a function of the year of the publication (black squares). d) Electrical conductivity e) Seebeck coefficient f) Power factor of n-type organic materials as a function of the year of the publication (red squares). Figure reprinted from Licence CC-BY. [33]

The relationships $S \alpha \sigma^{-1/4}$ and $PF \alpha \sigma^{-1/2}$ also hold in this case (Figure 2.8c,d). The n-type conductivity and power factor, again with some optimism, seem to have a slight upward trend, suggesting a step forward towards the most commonly used p-type, which are preferred mainly for their air stability (also after the doping process). For completeness, even if we could evaluate only a few data, the *zT*, and the value of the *k* of the n-type and p-type materials are reported in Figure 2.9.

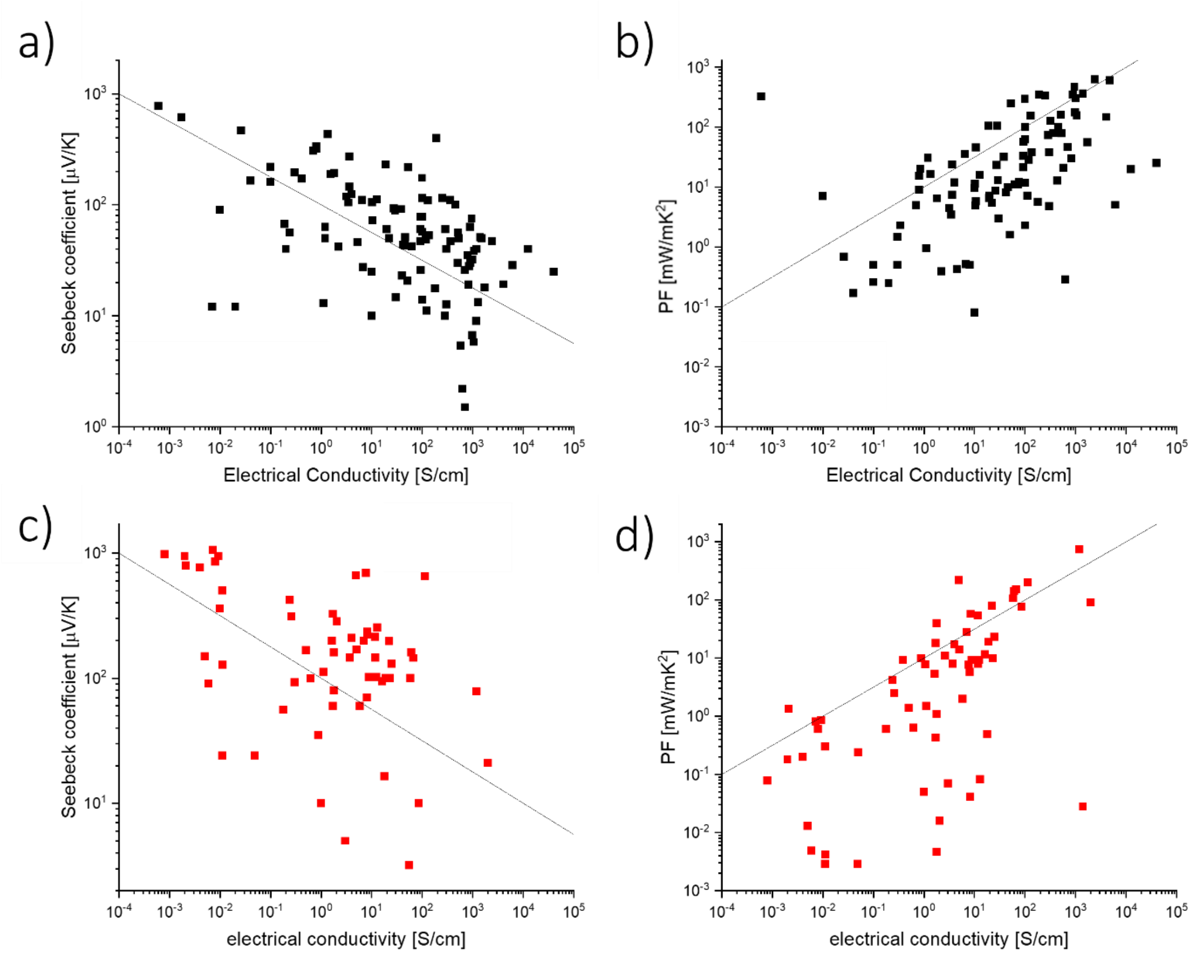

Figure 2.8: a) Seebeck coefficient and b) Power Factor of p-type organic materials as a function of the electrical conductivity (black squares). c) Seebeck coefficient and d) Power Factor of n-type organic materials as a function of the electrical conductivity (red squares). The grey dotted lines are the $S \alpha \sigma^{-1/4}$ and $PF \alpha \sigma^{-1/2}$ fitting. Figure reprinted from Licence CC-BY.[33]

Consistently, also the zTs are not showing any upward trends. Furthermore, it is possible to notice that the k are almost independent with respect to the σ, implying that the thermal conductivity is dominated by k_{lat}, as expected in disordered systems. A rough estimate using the Wiedemann-Franz form and the Sommerfeld value k_{el} (equation 2.24) for conductivity of 10^4 S/cm, realistically the best value for p-type, at $T = 300$ K should give a $k_{\text{el}} \sim 7$ W/mK, which is far below all the values in Figure 2.9 except for the CNTs (Carbon Nanotube) reported in.[63] This could be explained by the hypothesis that L for the highly doped semiconductor is far below L_0,[37] as described in sections 2.5 and 2.6.

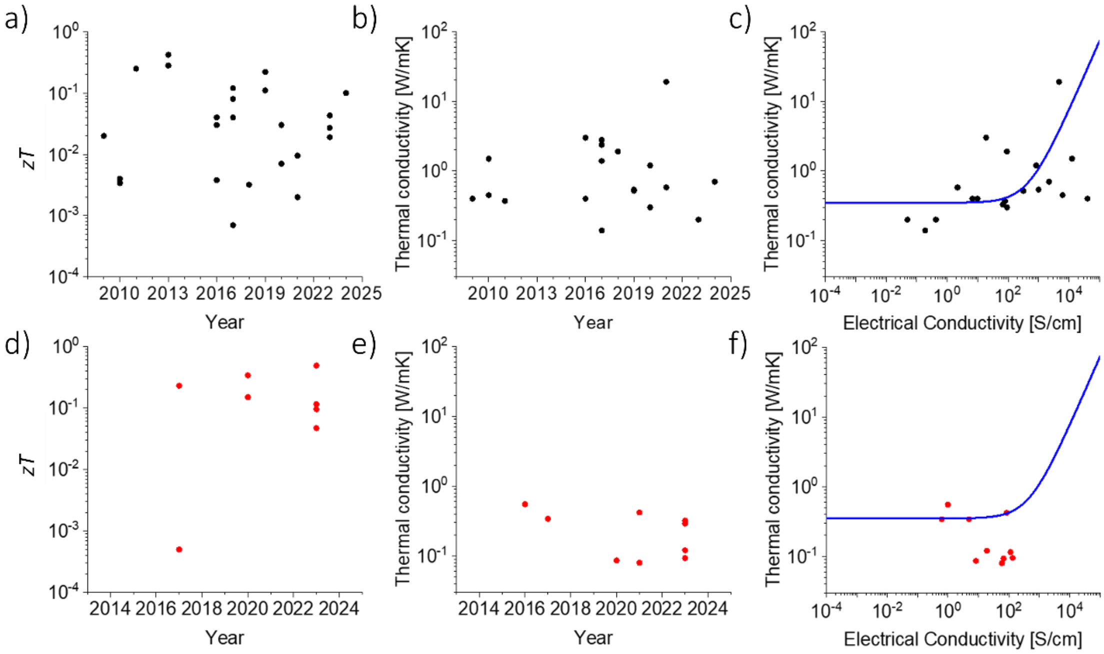

Figure 2.9: a) zT and b) thermal conductivity as a function of the year of the publication and c) thermal conductivity as a function of the electrical conductivity of the p-type organic materials (black dots). d) zT and e) thermal conductivity as a function of the year of the publication and f) thermal conductivity as a function of the electrical conductivity of the n-type organic materials (red dots). The blue lines are the value of $k = k_{el} + k_{lat}$, with k_{el} evaluated with the Wiedemann-Franz law (with $L = L_0$) and $k_{lat} = 0.35$ W/mK. Figure reprinted from Licence CC-BY. [33]

Overall, there has been no systematic improvement in organic TE parameters over time, and to break this trend, the field of organic TE needs a predictive and universally applicable theory to understand where there is room to increase zT and PF. Considering that the mobility, μ, of a good crystal is around 10 cm^2/V s and the charge carrier density of a (monomer) site density is typically $n = N_0 \sim 10^{21}$ cm^{-3}, the conductivity can be expressed as the equation 2.13 and results to be 10^3 S/cm (grey dashed line in Figure 2.7a,d), which is not far from the best values of the organic p-type TE. Increasing conductivity may therefore be a complicated path.

One possibility to improve the TE performance of a material would be to overcome the trade-off between σ and S, or with k_{el}, or to further investigate the relationship between these TE properties (σ, S, k_{el}) and k_{lat}, which seems to be the main contribution of thermal conductivity in the organic field.

To conclude this analysis, it must be said that the FoMs shown are not all the information we need to understand whether materials are suitable for use in an application, as the TE parameters are often measured under optimum conditions and in special environments (e.g. nitrogen atmosphere). It also does not take into account solvents, the ability to produce large area inks, and the cost of production. From this point of view, great progress (not visible in the comparison above) has been made, especially on the n-type side, with the recently discovered polymer PBFDO (DMSO-based), which has good environmental stability a very high electrical conductivity of around 2000 S/cm, and a modest $S \sim -21$ μV/K[32]. The k of this material has been measured for the first time in this thesis (see Chapter 5). This material is very promising and, hopefully, can be optimized with post-processing and structural variations. This new polymer is also easy and cheap to synthesize, also on a large scale, and appears to be suitable for printing, making it an ideal candidate for use in a TE device (see Chapter 5). Whereas for the more established p-type PEDOT (water-based) remains the best candidate for use in a device, showing good thermoelectric properties, being cost-effective, with good stability and good adaptability to the solution processes. Furthermore, also the 2D materials have attracted much attention,[64] due to their large σ, and a large PF. However, processing 2D materials into high-performance inks suitable for the large-area printed techniques has been quite difficult, due to the degradation of the performance after adding the additives. Significant progress in processability has been made in recent years,[65–67] and in 2022, Abdolhosseinzadeh S. et al. presented a graphene ink[68] with high performance and good printability, which has better thermoelectric properties compared to PEDOT, measured for the first time in the context of this thesis (Chapter 4), presenting a new opportunity for the realization of TE devices.

2.8 State of the art of inorganic materials

The state of the art of the inorganic materials has been limited to printable TE materials (at RT) to ensure a consistent comparison with solution-processable organic materials. This focus is motivated by the common goal shared by printable inorganic TE and organic TE materials, which is the possibility of creating cost-effective, shape-conformable thermoelectric generators (TEGs). Typically, printed inorganic TE materials are more cost-effective and have better mechanical properties than their bulk counterparts, although they have lower TE performance. Among inorganic materials, bismuth telluride and antimony telluride are widely targeted for printed TEGs due to their excellent performance around room temperature and their solution processability.

As discussed above the complete FoM to describe thermoelectric materials is the *zT* factor (Equation 2.27), also in this case the discussion will initially be limited to the analysis of the *PF* (Equation 2.27), not taking into account the *k*. To summarize the status of the printed inorganic materials we reported the *S*, σ, and PF *versus* the years of publication for p-type[69–77] (black dots) and n-type[78–85] (red dots) of the most relevant paper of the last 10 years.

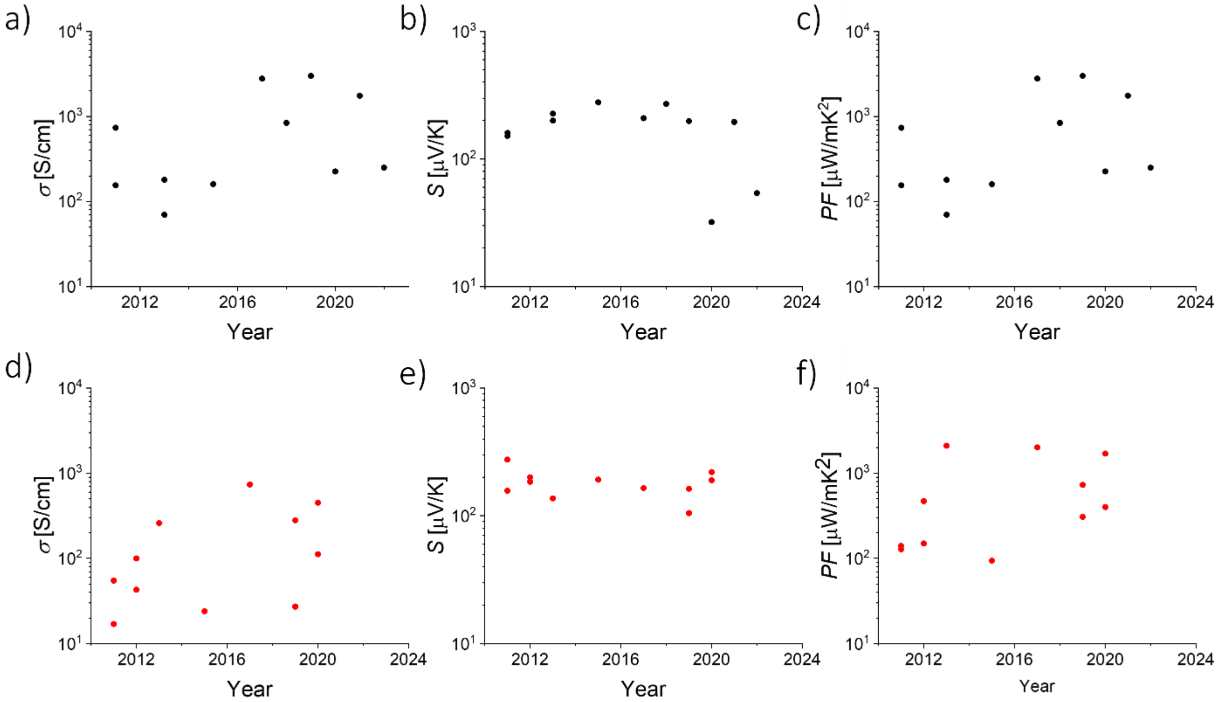

Figure 2.10: a) Electrical conductivity b) Seebeck coefficient c) Power factor of p-type inorganic materials as a function of the year of the publication (black dots). d) Electrical conductivity e) Seebeck coefficient f) Power factor of n-type inorganic materials as a function of the year of the publication (red dots). Figure reprinted from Licence CC-BY.[33]

The power factor of p-type and n-type materials appears to have a slightly increasing trend, especially in the case of n-type. Meanwhile, as we can see, the Seebeck coefficient is nearly constant and very similar to the values of bulk inorganic materials (around 250 µV/K). The increasing trend of the *PF* is due to the electrical conductivities, which increase over the years, getting close to the value of the bulk materials (~2000 S/cm). The

PF is an order of magnitude higher than that of the organic material. For inorganic materials, as shown in Figure 2.10 the *S* coefficient of p-type and n-type is essentially constant to the conductivity (slightly decreasing trend), until a $\sigma \sim 1000$ S/cm, in contrast with what is happening for the organic. Consequently, *PF* is increasing (almost) linearly with the conductivity (Figure 2.11).

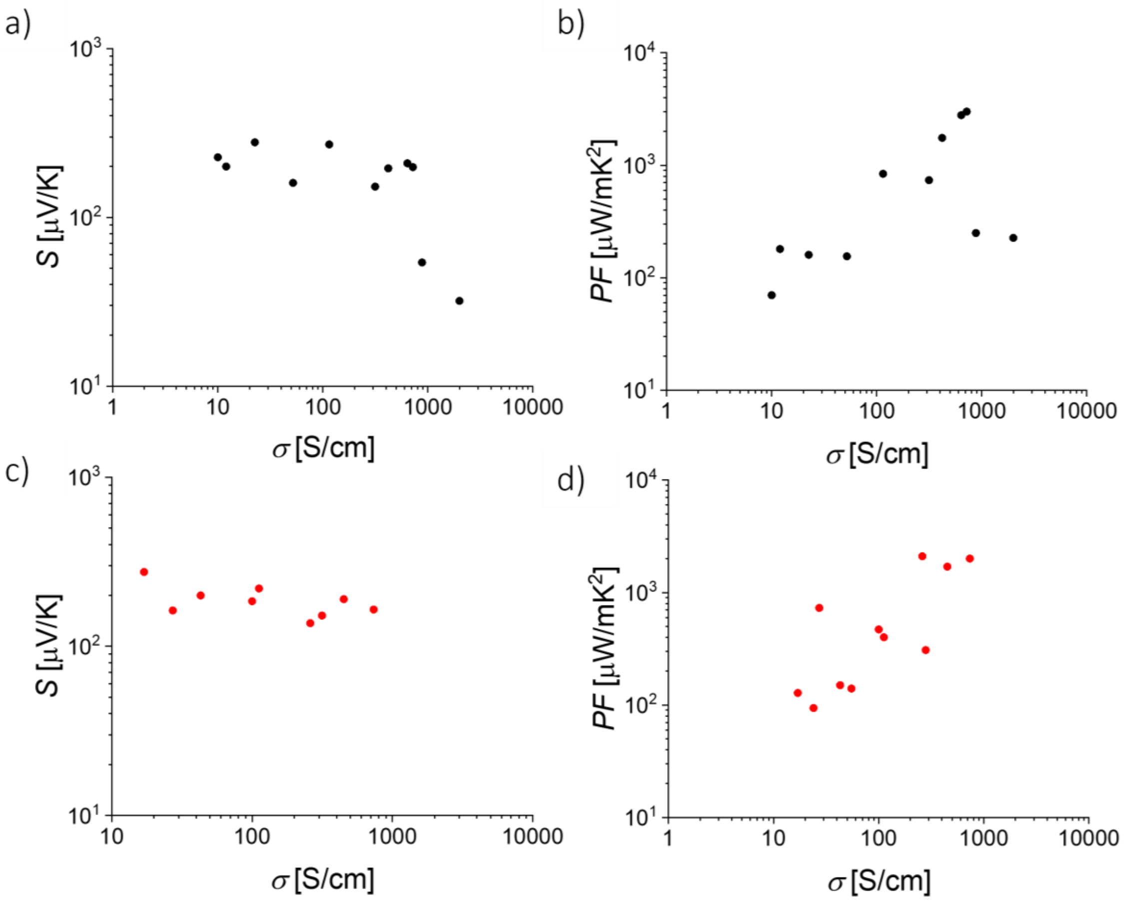

Figure 2.11: a) Seebeck coefficient and b) Power Factor of p-type inorganic materials as a function of the electrical conductivity (black dots). c) Seebeck coefficient and d) Power Factor of n-type inorganic materials as a function of the electrical conductivity (red dots). Figure reprinted from Licence CC-BY.[33]

For integrity, we reported the *zT* of the analyzed inorganic printable TE materials, even though we were only able to evaluate a few values, due to the lack of reported measured *k*. The values of the *zT* and the *k* of the n-type and p-type inorganic materials are shown in Figure 2.10

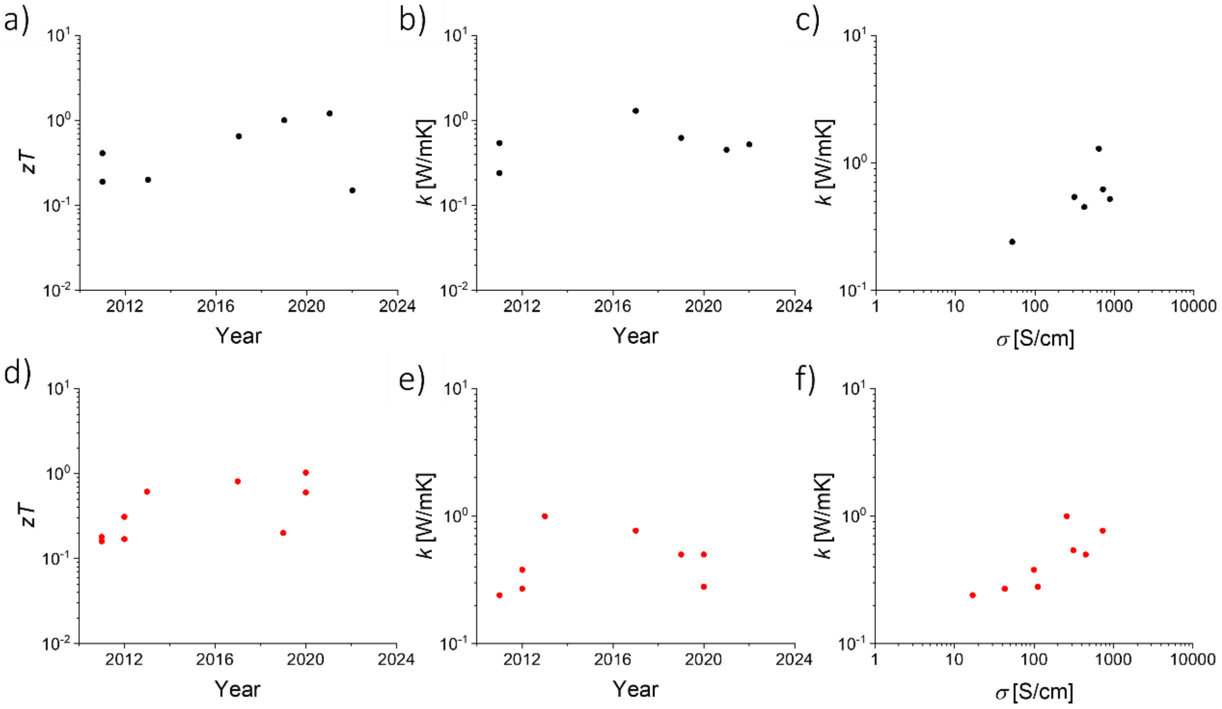

Figure 2.12: a) zT and b) k as a function of the year of the publication and c) k as a function of the σ of the p-type inorganic materials (black dots). d) zT and e) k as a function of the year of the publication and f) thermal conductivity as a function of the σ of the n-type inorganic materials (red dots). Figure reprinted from Licence CC-BY. [33]

The zTs are slightly increasing getting near to 1, which is, as anticipated, the limit for practical application, with the current record for printed TE inorganic materials (p-type) at 1.2.[77]

The zTs of the inorganic materials are one order and a half higher than the organic materials, this is because they have, as already discussed, higher PFs and thermal conductivities are just slightly higher (<1). The thermal conductivities are significantly lower than the inorganic bulk materials, due to the addition of additives, blinders, and solvents, necessary to improve the printability of the ink, which at the same time are responsible also for lower σ. In this case, the k seems to be the mix of the contribution of k_{el} and k_{lat} (~ 0.3 W/mK), since for a conductivity of 10^3 S/cm, using the Sommerfeld value L_0, and the Wiedemann-Franz law (equation 2.24) we obtain $k_{\mathrm{el}} \sim 0.7$ W/mK, and consequently a $k \sim 1$ in line with the value shown in Figure 2.10c,f.

In summary, the printed materials have a *S* similar to the bulk materials, with lower electrical conductivity, and lower thermal conductivity. This results in very similar *zT* values, considering that bulk materials have a *zT* around 0.6-1.5.[86] Highlighting the potential to make flexible and conformable printed devices with high performance, comparable to those made with expensive manufacturing processes. However, is worth remembering that this discussion is only based on an evaluation of the properties of the materials and does not take into account the evaluation of the printability of the ink, and the ambient stability, which are often overlooked in articles that show records of *zT* values, and are key aspects in a potential application.

To conclude the comparison between the inorganic printed TE and organic materials, we can say that the organic materials have *zT*s that are still too low to compete with the inorganic counterparts in terms of power generation. For instance, the Bi_2Te_3, shows at room temperature a zT~1, with a high *S* around 200 µV/K, a high σ near 1000 S/cm, and a modest thermal conductivity $k \sim 1$ W/mK. While some of these thermoelectric properties can be achieved with organic materials, particularly for p-type, they are not all present together in the same material. This suggests that overcoming the trade-off between σ and *S* and *k* could be key to improving overall performance, instead of trying to optimize the single parameter. Additionally, organic materials have better mechanical performance and processability, as well as being more cost-effective, environmentally friendly, and less rare. These aspects could not be taken into account in this analysis but are described and explained in the Introduction Chapter.

3.1 Thermoelectric Device

This chapter presents the working principle of the device. The analysis considers material properties as well as device-specific factors such as geometry and design and their effect on the overall performance of the device. It also discusses the two printing fabrication techniques used in this thesis, screen printing and inkjet printing, and the properties that the inks should have for good printability, in both cases. Finally, the state of the art of printed organic and inorganic TEGs is summarized.

3.2 Working principle

The basic unit of the TE devices is known as thermocouples. A thermocouple consists of a n-type material and a p-type material, hence with a S with opposite signs, connected electrically in series and thermally in parallel. When a thermocouple is connected to a load (Figure 3.1a), as the materials have opposite charge carriers, a current flows across the load, producing electrical power. In this configuration, the thermocouple is working as a thermoelectric generator TEG.

From an electrical perspective, a TEG can be represented as an ideal voltage source with an internal resistance (see Figure 3.1b). It provides a voltage proportional to the equivalent Seebeck coefficient and the ΔT:

$$V_{oc} = (S_p - S_n)\,(T_h - T_c) = S_{pn}\,\Delta T \tag{3.1}$$

Where S_p and S_n are the Seebeck coefficient of the p-type and n-type materials, respectively, and T_h and T_c are the hot side temperature and the cold side temperature.

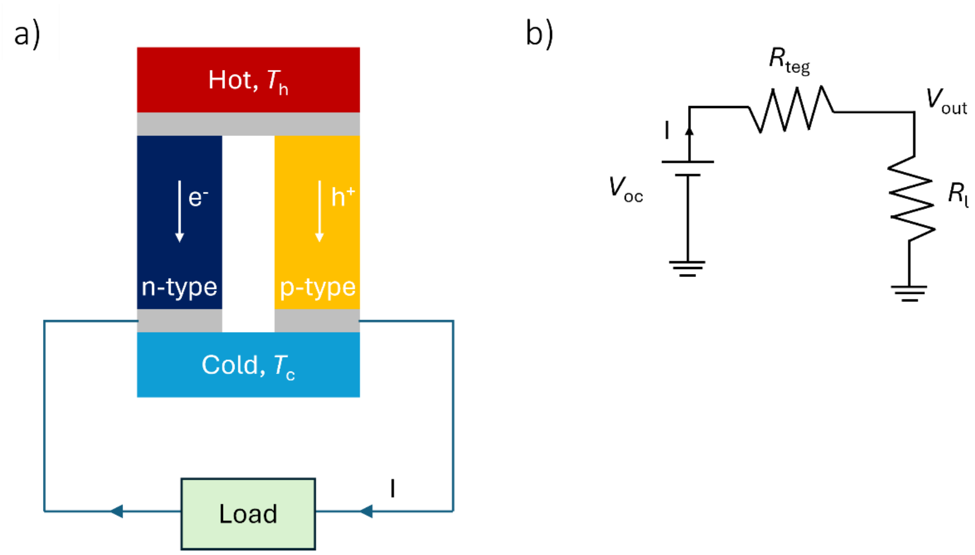

Figure 3.1: a) Graphical representation of a thermocouple operating as a thermoelectric generator. b) Electrical scheme of a thermoelectric generator.

The current can be evaluated as:

$$I = \frac{S_{pn}\,\Delta T}{R_p + R_n + R_l} = \frac{S_{pn}\,\Delta T}{R_{tot}} \tag{3.2}$$

Where R_p and R_n are the resistances of the p-type materials and the n-type materials, respectively, while R_l is the load resistance. Defining m the ratio between R_l and R_{teg}=(R_p+R_n):

$$m = \frac{R_l}{R_{teg}} \tag{3.3}$$

Then I and V_{out} can be described as:

$$I = \frac{V_{OC}}{R_{TEG}(1+m)} \quad \text{and} \quad V_{out} = V_{OC}\frac{m}{(1+m)} \tag{3.4}$$

Knowing that the power is the product between the current and the voltage, P_{out} results:

$$P_{out} = V_{out} I = \frac{V_{OC}{}^2}{R_{TEG}} \frac{m}{(1+m)^2} \tag{3.5}$$

Equation 3.5 is maximized for $m_{op} = 1$, $R_l = R_{teg}$ (electrical impedance matching with the load), and maximum P_{out} can be described as:

$$P_{out\ max} = \frac{1}{4}\frac{V_{OC}{}^2}{R_{teg}} = \frac{1}{4}\frac{(S_{pn}\,\Delta T)^2}{R_{teg}} \tag{3.6}$$

From equation 3.6 we can see how the P_{out} increases with the increase (absolute value) of the Seebeck coefficient of the materials and with the decrease of the resistances. The Seebeck coefficient is a TE property of the material itself. On the other hand, the resistance depends on the resistivity of the material (inversely proportional to the electrical conductivity), but also on the length (l_i) and the cross-sectional area (A_i) of the TE element. It can be defined as:

$$R_i = \rho_i \frac{l_i}{A_i} = \frac{l_i}{\sigma_i A_i} \tag{3.7}$$

Thus, it is possible to minimize the resistance by modifying the geometrical factors and increasing the electrical conductivity of the materials.

In addition to maximizing power, the efficiency η of the device should be optimized. The η is defined as the ratio between the P_{out}, that is the thermal energy effectively converted by the TEG, and the input heat flux ($\dot{Q}_{in}$). Describing the TEG from a thermal perspective (dashed blue box in Figure 3.2) based on the mono-dimensional (1-D) heat flux approximation in the stationary state,[87] we can assume that the heat flux is conserved at each node. Under these hypotheses, the heat input flux (at the hot junction), and the heat output flux (at the cold junction) can be described as:[88]

$$\dot{Q}_{in} = K_{pn}\Delta T - \frac{1}{2} R_{teg} I^2 + S_{pn} T_h I \tag{3.8}$$

$$\dot{Q}_{out} = K_{pn}\Delta T + \frac{1}{2} R_{teg} I^2 + S_{pn} T_c I \tag{3.9}$$

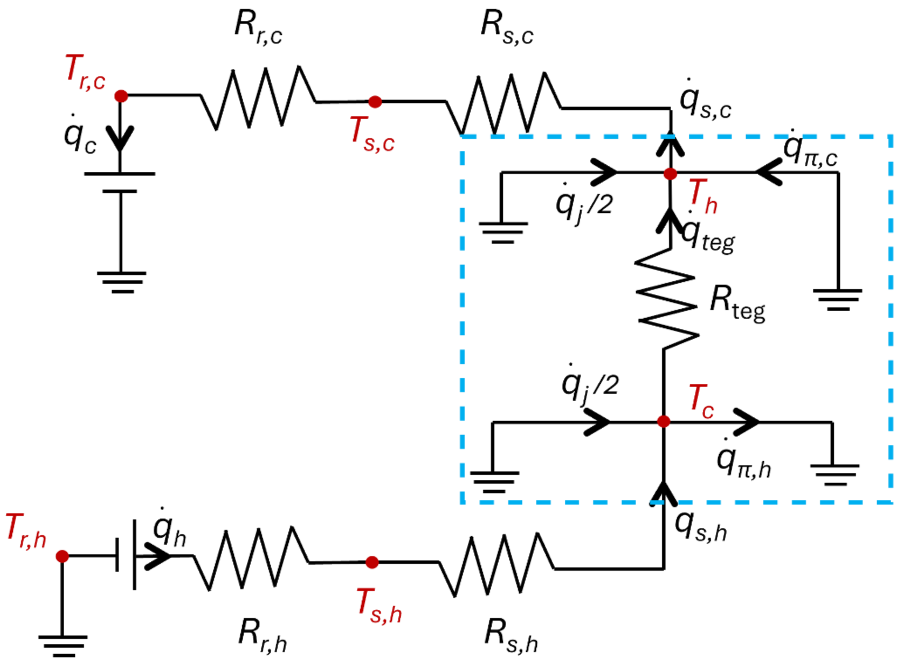

Figure 3.2: Thermal scheme of a thermoelectric generator based on the mono-dimensional (1-D) heat flux approximation in the stationary state. The resistances are the thermal resistances (inverse of the thermal conductances), while the temperatures and the heat flux are equivalent to the electric voltages and currents. The resistance outside of the blue dashed box represents the top and bottom substrates ($R_{s,h}$ and $R_{s,c}$) and the coupling between the hot source and the cold sink, and the environment.

The first heat term of equations 3.8 and 3.9 takes into account the heat flow caused by the temperature gradient (Fourier's law), which is proportional to the thermal conductance. The second heat term of equations 3.8 and 3.9 takes into account the Joule effect[89] and the third term the Peltier effect.[90] The equivalent thermal conductance K_{pn}= (K_p+K_n) can be expressed as a function of the thermal conductivity, in a dual way with electrical resistance:

$$K_i = k_i \frac{A_i}{l_i} \tag{3.10}$$

The η can be then evaluated:[91]

$$\eta = \frac{P_{out}}{\dot{Q}_{in}} = \frac{\Delta T}{T_h} \frac{m}{1+m-\frac{\Delta T}{2T_h}+\frac{(1+m)^2}{T_h Z}} \tag{3.11}$$

Where Z is the FoM of the device:

$$Z = \frac{{S_{pn}}^2}{K_{pn}R_{teg}} \tag{3.12}$$

The FoM Z can be optimized for maximizing η, $m_{o\eta} = \sqrt{1 + ZT_m}$, where $T_m = (T_h + T_c)/2$ (thermal impedance matching with the heat source and heat sink). Resulting in a maximum η:

$$\eta_{max} = \frac{T_h - T_c}{T_h} \frac{\sqrt{1+ZT_m}}{\sqrt{1+ZT_m} - \frac{T_c}{T_h}} \tag{3.13}$$

Thus, to maximize at the same time the η and P_{out}, both the conditions, thermal and electrical matching have to be satisfied, and $m_{op} = m_{o\eta} = \sqrt{1 + ZT_m}$.

3.3 Distinction between the ZT of devices and zT of materials

It is not always valid to assume that the *ZT*, of the devices corresponds directly to the *zT* of the materials (equation 2.27), which is independent of the device design.

The maximum device efficiency η_{max} is generally defined by equation 3.13, where Z is the FoM of the device and depends on the geometric dimensions (equation 3.12). The first term is the maximum efficiency system (Carnot efficiency) and the second term, which depends on the thermoelectric properties S, σ, and k, and the geometric dimensions is responsible for the reduction of the efficiency (the efficiency increases with the increasing of the *ZT*).

Only under the assumptions that the thermoelectric material properties S, σ, and k remain constant with temperature, which is typically a large approximation if applied when ΔT is large, the heat flow is one-dimensional with no additional losses, and the n-type and p-type legs are perfectly matched, the material FoM *zT* and the device FoM *ZT* are the same.[51] Only in this case equation 2.27 (evaluated at $(T_c+T_h)/2$) and equation 3.12 (evaluated between T_h and T_c) are equivalent, and Z is independent of the geometric dimensions:[51]

$$Z_{opt} = \frac{{S_{pn}}^2}{(\sqrt{\rho_p k_p} + \sqrt{\rho_n k_n})^2} \tag{3.14}$$

In conclusion, the assumption that the material FoM *zT* is directly equal to the device FoM *ZT* is only valid under ideal conditions, which are rarely met. Therefore, careful consideration of device geometry and a thorough analysis of the TE material properties across a wide temperature range are essential to accurately evaluate the efficiency of thermoelectric devices.

3.4 Design optimization of printed TEGs

In the previous section 3.1, we described a TEG made up of a single thermocouple assuming that the ΔT across the device is known. In a more accurate description of the system, closer to a real application, a printed TEG consists of several thermocouples, n, connected thermally in parallel and electrically in series, and we only know the external temperature difference $\Delta T_{\mathrm{ext}} = T_{\mathrm{r,c}} - T_{\mathrm{r,h}}$ (Figure 3.2). In addition, due to manufacturing constraints, a real printed structure requires a substrate to carry it and, in some cases, an insulator to electrically isolate the thermoelements, which inevitably affects the power output.

To understand how to change the device design to maximize the performance, we still need to make simplifying assumptions. Firstly, we assume that ΔT is relatively small, and the thermoelectric properties of the materials (S, σ, k) are constant. Secondly, since the thickness of the device of the printed materials is much smaller than the characteristic dimensions, the heat exchange through the lateral surfaces can be neglected (no heat losses). Finally, we assume that the electrical and thermal resistances of the metal interconnections and the electrical contact resistances between the thermoelectric material and the metal interconnections are also negligible (further consideration of this hypothesis is provided in Chapter 4). In addition, the temperatures of the cold and hot reservoirs are considered to be constant (assuming infinite heat capacity).

To conduct this analysis, we examine the vertical device represented in Figure 3.3a. Note that the same analysis can be extended to folded planar architectures (Figure 3.3c), including all types of TEG presented in this thesis.

The geometric design parameters that can be tuned with printing are the areas and thicknesses of the materials, with some limitations due to manufacturing techniques (discussed further). Figure 3.3a shows the cross-sectional lateral view of the device, while Figure 3.3b the top view of a thermocouple. The area of thermoelectric materials of a single thermocouple and the total area of the single thermocouple can be expressed as follows:

$$A_{pn} = A_p + A_n \quad \text{and} \quad A_{pni} = A_p + A_n + A_{in} \tag{3.15}$$

Where A_p and A_n are the areas of the p-type and n-type materials, respectively, while A_i is the area of the insulator. Thus, we can define the number of thermocouples per unit area as:

$$n = \frac{1}{A_{pni}} \tag{3.16}$$

And the Fill Factor (*FF*), which is the ratio between the area occupied by the TE materials and the total area of the device:

$$FF = \frac{A_{pn}}{A_{pni}} \tag{3.17}$$

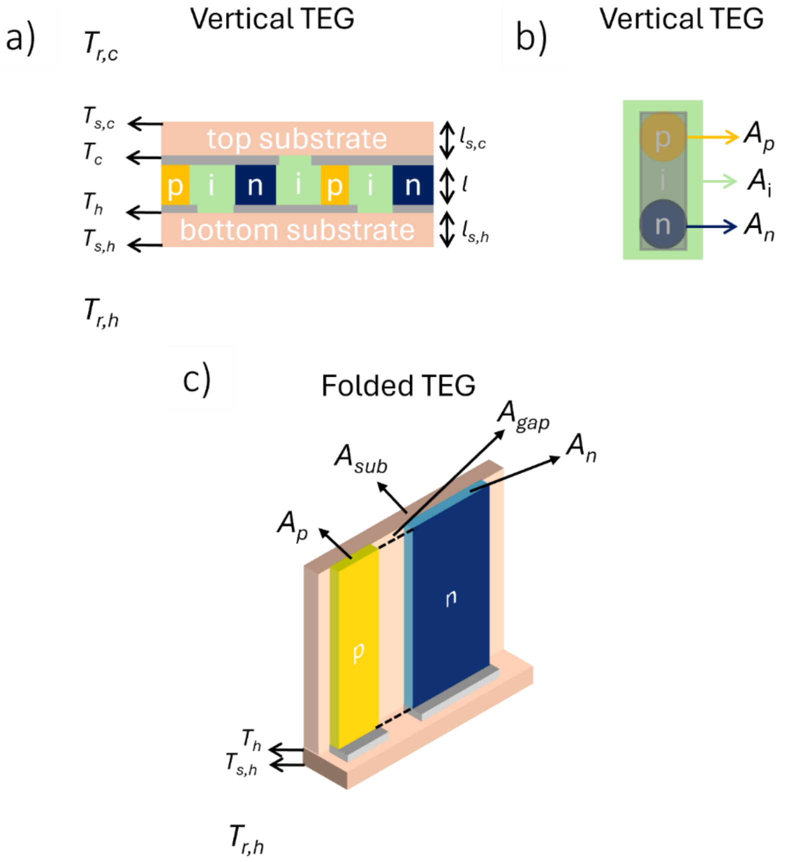

Figure 3.3: a) Lateral view of a vertical TEG. b) top View of a thermocouple. c) Adaptation of the model for the folded TEG.

The p_{density}, i.e. the power generated per unit of area, can then be described by reference to equation 3.5 (with $nR_{pn} = R_{teg}$):

$$p_{density} = i_{density} v_{out} = \frac{v_{oc}^2}{A_{pni}{}^2 n\, R_{pn}} \frac{m}{(1+m)^2} = \frac{FF\ S_{pn}{}^2}{\rho_{pn}\, l} \frac{m}{(1+m)^2} (T_h - T_c)^2 \tag{3.18}$$

Where v_{out} is the voltage on the load per unit area and i_{density} is the current flowing per unit area, while ρ_{pn} is the weighted average electrical resistivity of a thermocouple $\rho_{\text{pn}} = (\rho_{\text{p}}/A_{\text{p}} + \rho_{\text{n}}/A_{\text{n}})A_{\text{pn}}$, and l is the length of the thermoelectric material parallel to the heat flow (here we assume an equal length of the p- and n-type element).

However, $T_{\text{h}} - T_{\text{c}}$ is only still an unknown fraction of the external temperature $T_{\text{r,h}} - T_{\text{r,c}}$ (Figure 3.3) and depends on the l, as well as the substrate, the cold-hot reservoir, and the thermal coupling with the environment.

To obtain an expression of p_{density} as a function of the known $T_{\text{r,h}} - T_{\text{r,c}}$ we need to consider also the thermal behavior of the TEG. As already analyzed in section 3.1 the TEG can be represented with an electrical equivalent scheme of the thermal issue, Figure 3.2, with the resistance representing the thermal resistance (inverse of the thermal conductance). Note $R_{\text{r,h}}$ and $R_{\text{r,c}}$ are introduced to take into account the thermal coupling with the environment. This scheme was presented by Beretta et. al.[92] building on the scheme originally presented by Yazawa et. al.[93]

The effective temperature $T_{\text{h}} - T_{\text{c}} = \Delta T$ is a non-linear function of the external difference of temperature $T_{\text{r,h}} - T_{\text{r,c}} = \Delta T_{ext}$ since we have to consider the Fourier conduction and the Peltier and Joule effect. Considering the hypotheses described above it is possible to express the heat in every section of the model: the coupling with the environment, the bottom substrate, the TEG, and the top substrate (Figure 3.2). This non-linear system is thoroughly described and solved using iterative methods in the works.[88,92,94]

In this thesis, we will not discuss the complete solution but we will focus on analyzing the simplified linear model presented by Beretta et al.,[92] which allows us to make reasonable design choices, sacrificing some accuracy but gaining in terms of computational complexity.

Starting from equations 3.8 and 3.9, with the hypothesis of small ΔT, the heat dissipated per unit of area due to the Joule effect can be neglected, as it depends on $(\Delta T)^2$:

$$\dot{q}_j = \frac{FF\, S_{pn}{}^2 (\Delta T)^2}{\rho_{pn}(1+m)^2 l} \tag{3.19}$$

This term is always much smaller than the Peltier and Fourier conduction terms. The Peltier term, on the contrary, is not always negligible, since it depends on ΔT. The Peltier heat per unit of area can be described as:

$$\dot{q}_{\pi,i} = \pm \frac{FF\,{S_{pn}}^2 \Delta T}{\rho_{pn}(1+m)l} T_i \quad \text{where } T_i = T_h, T_c \tag{3.20}$$

And the Fourier contribution per unit of area:

$$\dot{q} = \frac{k_{pni}}{l} \Delta T \quad \text{where } k_{pni} = \frac{k_p A_p + k_n A_n + k_{in} A_{in}}{A_{pni}} \tag{3.21}$$

k_{pni} is the average thermal conductivity of the whole thermocouple. Analogously, the $k_{\mathrm{pn}} = (k_{\mathrm{p}}A_{\mathrm{p}}+k_{\mathrm{n}}A_{\mathrm{n}})\,/A_{\mathrm{pn}}$ is the average thermal conductivity of the thermoelectric material.

Thus, the Peltier terms can be discarded only if:

$$FF \frac{ZT_i}{(1+m)} \ll \frac{k_{pni}}{k_{pn}} \tag{3.22}$$

With this additional approximation, thermal losses from thermoelectric conversion within the device are not considered, and the heat flux leaving the cold reservoir is assumed to match the heat absorbed from the hot reservoir, simplifying the system in Figure 3.2 to a series of resistances. Therefore, the ΔT is linearly related to the ΔT_{ext} (simple thermal resistance divider):

$$\Delta T = \frac{\Delta T_{ext}}{1 + \frac{k_{pni}}{l} \frac{1}{h_{eq}}} \tag{3.23}$$

Where $h_{\mathrm{eq}}^{-1} = h_{\mathrm{r,h}}^{-1}+h_{\mathrm{s,h}}^{-1}+h_{\mathrm{s,c}}^{-1}+h_{\mathrm{r,c}}^{-1}$, the equivalent heat transfer coefficient ($h_{\mathrm{i}} = k_{\mathrm{i}}/l$ or $h_{\mathrm{i}}=K_{\mathrm{i}}/A_{\mathrm{i}}$ equation 3.10). From this relation, we can see that increasing the l thermal resistance of the thermocouple becomes dominant with respect to everything else, and the $\Delta T \rightarrow \Delta T_{ext}$ maximizes the efficiency. However, by substituting the ΔT in equation 3.18 the p_{density} can be expressed as follows:

$$p_{density} = \frac{FF\ {S_{pn}}^2}{\rho_{pn}\, l} \frac{m}{(1+m)^2} \frac{(\Delta T_{ext})^2}{(1 + \frac{k_{pni}}{l} \frac{1}{h_{eq}})^2} \tag{3.24}$$

From which it is clear that p_{density} is maximized for a specific l_{opt}, and m_{opt}:

$$l_{opt} = \frac{k_{pni}}{h_{eq}} \quad \text{and} \quad m_{opt} = 1 \tag{3.25}$$

Similarly to the electrical matching (equation 3.6), thermal matching occurs when ΔT_{ext} is twice ΔT. Therefore, the maximum p_{density} can be evaluated as:

$$p_{density\,max} = \frac{Z}{16} \left(\frac{FF\, k_{pn}}{k_{pni}}\right) h_{eq} (\Delta T_{ext})^2 \tag{3.26}$$

Where $Z = S_{pn}^2/(\rho_{pn}\, k_{pn})$. Note that Z is not independent of the A_{pn} for the definition given before of ρ_{pn} and k_{pn}, it is independent of the l, because we assumed $l_p = l_n$. Unfortunately, co-optimization with respect to m, l, A_p/A_n does not yield an analytical expression. However, $p_{\text{density max}}$ can be optimized solely in terms of Z by selecting a specific leg ratio. In particular:

$$\frac{A_p}{A_n} = \sqrt{\frac{k_p \rho_p}{k_n \rho_n}} \tag{3.27}$$

Under this condition, Z is:

$$Z_{opt} = \frac{S_{pn}{}^2}{(\sqrt{\rho_p k_p} + \sqrt{\rho_n k_n})^2} \tag{3.28}$$

That is the same expression found in equation 3.14, making Z independent of the geometric factor. Furthermore, if $k_p \approx k_n$ and $\rho_p \approx \rho_n$ then equation 3.28 becomes easier and the Z is maximized for $A_p = A_n$.

Equation 3.26 allows the evaluation of the impact of the design parameters on the power provided by the TEG. Beginning with the most straightforward consideration, if $k_i = 0$ then $k_{pni}A_{pni} = k_{pn}A_{pn}$, and the first term in brackets becomes unity. As a result, the p_{density} is independent of the FF. However, for printed TEG this assumption is not justified. If $k_i \neq 0$, the k_{pni} can be described as $k_{pni} = k_{pn}(FF) + k_i(1\text{-}FF)$ and can range from k_{pn} to k_i, when $FF = 1$ and $FF = 0$, respectively. Thus, as the FF increases, the $p_{\text{density max}}$ increases, but the l_{opt}, also increases. In contrast, tuning the h_{eq} can increase the $p_{\text{density max}}$ and decrease the l_{opt}, allowing for the use of less thermoelectric material and reducing costs. The upper limit of h_{eq} is determined by the lowest heat transfer coefficient section (equation 3.23). Therefore, the primary focus should be on carefully selecting the thickness and the thermal conductivity of the substrates and optimizing the thermal coupling with the environment.

Another important parameter to consider is the voltage provided by the TEG, V_{out} as it often needs to exceed a certain threshold value to be effectively amplified by an electronic booster circuit (for further discussion, see Chapter 6). Considering the thermal and electrical match (4 in the denominator), the $V_{\text{out max}}$ can be expressed as shown in Equation 3.29:

$$V_{out\,max} = \frac{S_{pn}\Delta T_{ext}}{4A_{pni}} A_{TEG} = \hat{V}_{out} \tag{3.29}$$

Where $\hat{V}_{\text{out}}$ is the required value, and A_{TEG} is the total area of the TEG. To find the effective number of thermocouples N needed to provide a specific $V_{\text{out max}}$ then:

$$N = \frac{A_{TEG}}{A_{pni}} = \hat{V}_{out} \frac{4}{S_{pn} \Delta T_{ext}} \tag{3.30}$$

Where A is the total area of the TEG. If A_{pni} is fixed from the technological resolution limits, then we need N thermocouples, and the device must have a certain A_{TEG}. Clearly, if A_{pni} is reduced, for example by changing the printing technology, then A_{TEG} is also reduced, simplifying the heat dissipation.

3.5 Role of the substrate and metal interconnections

Besides the choice of thermoelectric materials and the geometrical design, we must carefully select the insulating substrate that supports the device. The choice of the correct substrate plays a crucial role since it also determines the ΔT, as reported in the previous section 3.4. The thermal conductivity of the substrate k_{sub}, and the thickness of the substrate, which are directly related to the heat transfer coefficient, have to be chosen to maximize the power density. With regard to the two architectures discussed in this thesis, there is one main distinction that can be made.

In the vertical architecture, conceptually similar to the Peltier elements (see Figure 3.3a,b), the substrate acts as an in-series thermal resistance between the heat source/sink and the thermoelectric material, increasing the thermal contact resistance. In the folded architecture (see Figure 3.3c) the substrate acts as parallel thermal conductance between the thermoelement, causing unwanted thermal losses. Thus, a thinner substrate is generally preferred in both vertical and folded architectures, as it minimizes thermal resistance and unwanted heat losses, respectively.[94] On the other hand, in a vertical architecture, where the substrate acts as a thermal bridge in series with the thermoelectric material, a high k_{sub} is essential to ensure efficient heat transfer and maximize the ΔT. While, in a folded architecture, a low k_{sub} is desired to prevent heat from bypassing the thermoelectric material, thereby minimizing thermal losses and avoiding thermal short-circuiting.

The main types of flexible substrates currently available are polymer foils, glass fibers, and passivated metal foils, each offering different properties that make them suitable for multiple applications. Polymer foils are lightweight, and highly flexible, but are not good thermal conductors, glass fibers offer excellent thermal stability, and passivated metal foils offer high thermal conductivity but lower flexibility.

In addition to the substrate, the role of the metal interconnection also impacts the thermal behavior of the device, particularly in vertical architectures. The model proposed by previous works,[88,92,94] presented in the previous section 3.4, does not take into account the later heat conduction, transversal to the leg. These works assume that the metal interconnections thermally short-circuit the thermoelement and that the ΔT drops across the legs, n-type and p-type, are the same. This assumption is valid only depending on the size, thickness, distance between the legs, and thermal properties of the materials. Figure 3.4a shows the complete thermal equivalent circuit that should be considered taking into account the presence of the thermal resistance of the metal interconnections *(*R_{int}) and the lateral heat conduction, in contrast to the simplified scheme presented in Figure 3.3**.** If the materials have standard values of k, the device thickness is in the order of μm, which is common for printed layers, and the device size is in the order of mm^2, Figure 3.4a must be modified. Figure 3.4b shows how a TEG could be represented in this case. The ΔT drops across the legs here could be almost independent (depending on the thermal conductivities of the materials and their dimensions). More detailed considerations will be described in Chapter 4.

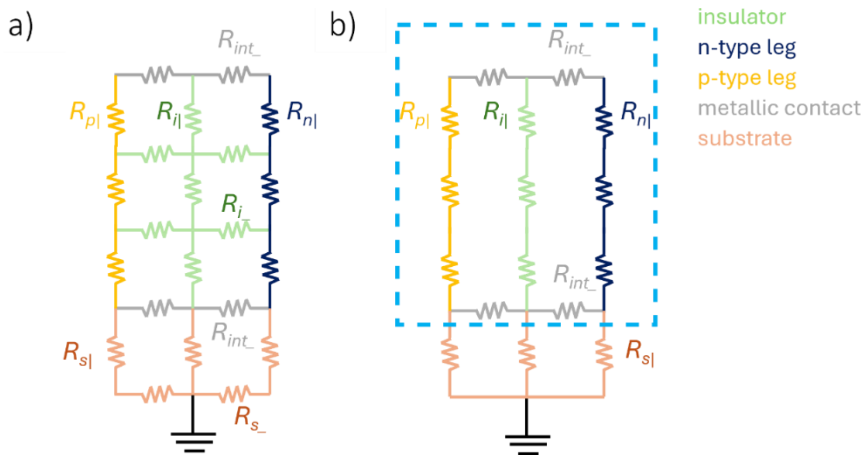

Figure 3.4: a) Thermal scheme of a thermoelectric generator considering the role of the metal interconnections and the lateral heat conduction. b) Thermal scheme of a thermoelectric generator considering the role of the metal interconnections and the lateral heat conduction, assuming standard values of materials k (for metal interconnections, TE legs, insulator, and substrate), a device thickness in the order of μm, and size in the order of mm^2. The resistance with different colors represents different materials.

3.6 Printing technique

The flexible TEG can be fabricated using solution-processable TE materials, introduced in Chapter 2*,* which are often suitable for producing inks with specific rheological properties that can be deposited using various low-temperature techniques.[95,96] These methods are much less complex than vacuum evaporation processes and require simpler and less energy-consuming equipment for both laboratory and industrial scenarios.

In basic research (lab scale), samples are often prepared using simple deposition techniques such as spin coating[97] and blade coating.[98] In these methods, a shearing force is applied to a drop of solution on a substrate, creating a thin layer of liquid that forms a film as the solvent rapidly evaporates. In spin-coating the solvent evaporated due to the centripetal force generated by the spinning motion of the substrate. Angular velocity, acceleration, and time are the key parameters for controlling film thickness and morphology. Although simple, spin coating lacks the fine control of film properties required in production lines, i.e. uniform thickness, and is limited to flat and small surfaces. On the other hand, blade coating is a direct writing technique capable of depositing large-medium area thin films using a running blade to spread the ink over the substrate. Although it does not allow the creation of real patterns. Spin coating and blade coating are effective techniques for exploring material properties and gaining preliminary insights into the printing process, however, they are not suitable for producing application-oriented TEGs, the object of this thesis.

For industrial-scale production, high-throughput methods such as screen printing, and drop-on-demand methods such as inkjet printing have been adapted for both organic and inorganic TE inks. It is important to note that each printing technique requires inks with specific rheological characteristics. The choice of coating technique therefore depends on the ink and the desired device architecture.

3.6.1 Inkjet printing technique

Inkjet printing offers a digital drop-on-demand approach that is valuable for high-resolution and low-cost device manufacturing.[99] This technique controls the formation and ejection of ink droplets through the nozzle of a cartridge (Figure 3.5b), enabling precise deposition with high resolution and minimal ink waste. It is a cost-effective alternative to traditional microfabrication techniques such as photolithography, and it is compatible with metallic, dielectric, and semiconductor inks.

Inkjet printing is a non-contact technique that controls digitally the deposition of each drop in the absence of masks. A resolution that can be achieved with regularity is typically 30 μm. Furthermore, since this technique does not require the use of masks, the pattern and the architecture of the device can be tailored easily and at no cost by simply modifying the layout in a bitmap file.

Not all inks are suitable for inkjet printing, they must meet some specific physical properties e.g. viscosity, surface tension, density, and volatility to be jetted through the nozzle. Additionally, the ink must be also chemically compatible with the cartridge, and it must be suitable for the substrate in terms of wettability and adhesion, while the substrate must withstand any post-treatment required to achieve the desired functional material. Furthermore, the ink should be stable, ensuring a long print, since the printing should be reliable over time, with no clogging or damage in the printhead.

We can give general guidelines as to the characteristics an ink should have to be considered printable. To begin, the size of the particles ejected from the nozzle should be at least 20-100 times smaller than the size of the nozzle,[100] depending on how long the printing stability is needed. Frequently, the formation of aggregates with higher size than single particles causes the printhead clogging. The pre-treatment of the ink with filters and disaggregation methods can help to avoid the mentioned clogging. Note that there are currently only two nozzle sizes (maximum 2.4 pl) on the market, due to the *Fujifilm* monopoly, this drastically reduces the number of printable inks. In terms of viscosity (η), considering most of the inks behave as Newtonian fluids,[101] a range (at operating temperature) of about 10-12 mPa-s is required for good printability, but they are still printable with a η of up to 30 mPa-s.[102] Shear-thinning non-Newtonian fluids,[101] where the viscosity of the fluid decreases at higher shear rates, are also printable (PBFDO presented in Chapter 5). In this case, the viscosity at a low shear rate (~1 s^{-1}) for optimal printing is usually higher, up to 20-25 mPa s.[103] To reduce the viscosity a standard approach is to add a lower viscosity co-solvent and/or increase the printing temperature of the cartridge. Another important parameter is the surface tension γ, i.e. the force per unit length applied along the surface of a liquid, it is important for the formation of the droplet. γ must be high enough to prevent dripping from the nozzles, yet low enough to facilitate the formation of droplets. A standard range value of the surface tension for the drop formation is 30-50 mN/m.[100] Playing with the solvent and the temperature of the cartridge is also a standard way of adjusting the surface tension.

The printability of the drop can be predicted from the value of a general parameter Z_{print} which considers the viscosity, surface tension, and density of the ink, together with the nozzle size. This parameter is the inverse of the Ohnesorge Oh parameter and it is dependent on the Weber We and Reynold Re numbers. These parameters can be expressed as:

$$Re = \frac{\rho v d}{\eta} \tag{3.31}$$

$$We = \frac{\rho v^2 d}{\gamma} \tag{3.32}$$

$$Z_{print} = \frac{1}{Oh} = \frac{Re}{\sqrt{We}} = \frac{\sqrt{\rho \gamma d}}{\eta} \tag{3.33}$$

Where v is the velocity of the droplets, d is the nozzle diameter, and ρ the density of the ink. The ink has a good printability for $1<Z_{print}<10$.[104,105] When $Z_{print}<1$ the ink is too viscous, while for $Z_{print}>10$ there are satellite droplets, and the placement and printing of high-resolution structures become complicated. Z_{print} is independent of v, but the drop must have enough energy to overcome the surface energy of the ink at the nozzle, so the drop cannot be ejected below a certain velocity limit.[106] For this even if $1<Z_{print}<10$, we must also limit the printability to $We > 4$. Moreover, if the momentum of the droplet is too large when it impacts the substrate the droplets will splash. This limit also depends on the roughness of the substrate, for flat or smooth surfaces, the condition for good printability can be described as follows:[107]

$$We^{1/2}Re^{1/2} < 50 \tag{3.34}$$

All the previous conditions can be summarized with the Re vs. We graph shown in Figure 3.5a. A parameter that is not included in this analysis is the volatility of the ink. The solvent of the ink should evaporate after printing a layer on the substrate, but it should not dry in the nozzle, as this could cause clogging.

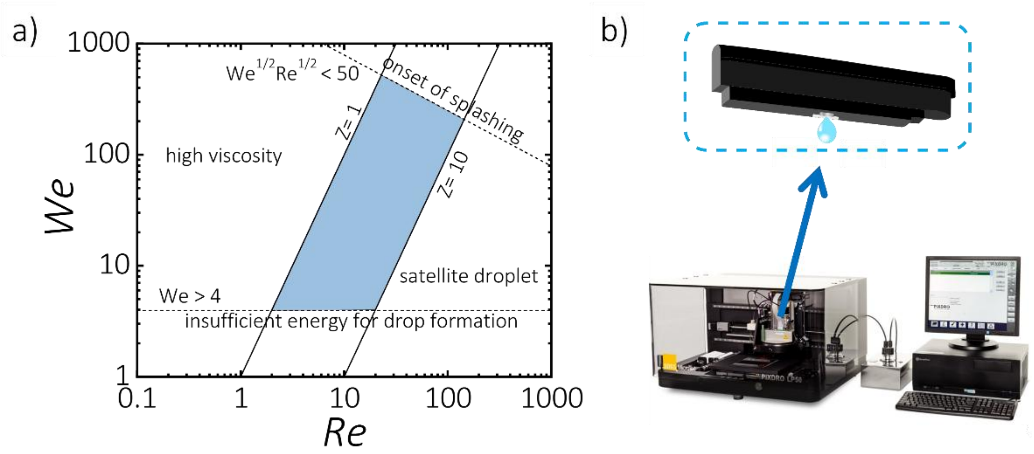

Figure 3.5: a) Weber number as a function of Reynold number. The blue area represents the area of good printability. b) Pixdro printer machine and a sketch of the cartridge showing the drop-on-demand deposition of an ink droplet.

According to these requirements, the printer parameters should be adjusted to optimize droplet generation for optimal printing on the substrate. In this thesis has been used a PixDro inkjet printer (Figure 3.5b). The main settings that can be adjusted are:

- Jetting frequency (depending on the viscosity of the ink)
- Drop speed (principally changing the signal Waveform)
- Cartridge temperature (depending on the viscosity of the ink)
- Dot per inch *DPI* (depending on the desired resolution)
- Printing velocity (depending on the desired resolution)

Finally, it is important to point out that the γ affects also the wettability of the substrate,[108,109] i.e. how uniformly the liquid spreads and how well it adheres, influencing the quality of the printed film. The wettability of the substrate can be modified by changing its surface tension with some treatment directly on the surface e.g. chemical coating, plasma etching, and temperature treatment (even during the printing).

3.6.2 Screen printing technique

Screen printing is a versatile and widely used technique that employs a patterned screen to transfer ink layer by layer to a substrate through the pressure of a squeegee.[110] It is effective at producing thick, uniform films and is compatible with a wide range of materials, making it ideal for the mass production of electronic devices.

Screen printing is an additive printing process and is very cost-effective, especially when considering its ability to print large areas up to square meters simultaneously.[111,112] This technique is the best solution for printing architectures with resolutions above 500 µm, ranging from square centimeters to square meters in size.

In contrast with inkjet printing, screen printing is a contact printing technique and requires stencils. Each printing layer requires a different screen, with a stretched mesh. The mesh on the substrate side is coated with an emulsion with a negative desired layout, which defines the areas where the material is to be deposited (see Figure 3.6). The mesh is needed to hold the emulsion and to control the quantity of the ink passing through. The Screens can be designed using standard layout tools. The ink is distributed on the screen in areas where the emulsion is absent, ensuring it does not leak through.[113] During the printing phase, a metal flood bar distributes the ink over the mesh, followed by a plastic squeegee that presses the mesh at a certain angle, forcing the ink through the screen onto the surface (see Figure 3.6). The ink is transferred only where the emulsion is open, with the desired layout (ss Figure 3.6). After the printing phase, the screen elastically returns to its initial position.

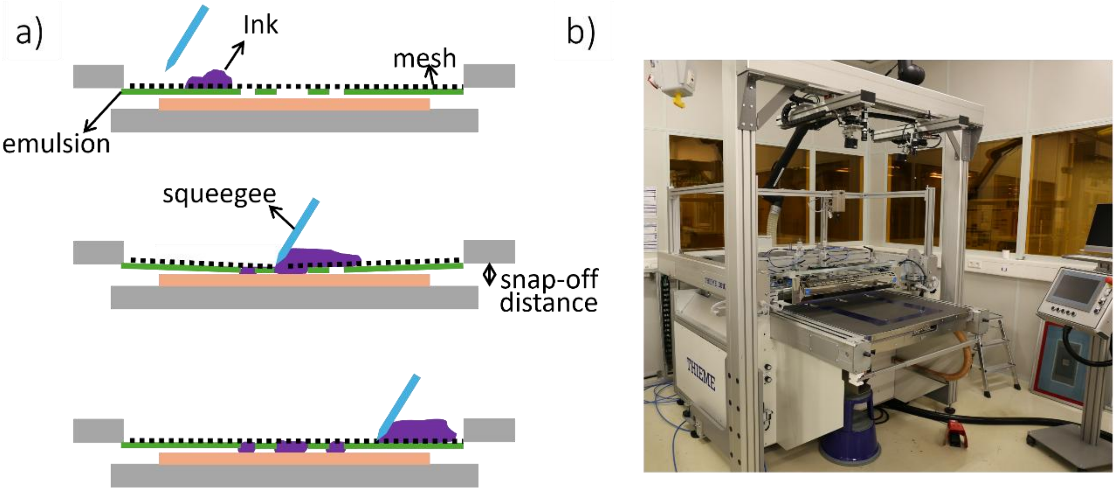

Figure 3.6: a) Schematic of the screen printing phase. The ink is spread on the screen with a squeegee and it passes through the mesh openings where the emulsion is absent. b) Photograph of the Thieme industrial screen printing machine used in this thesis.

For achieving high-quality printed films with the screen-printing technique, we need to carefully adjust the mesh, the print setup, and various printing parameters and select inks with appropriate properties.[113]

Regarding the mesh, the principal characteristic we can tune is the mesh count of the screen, which refers to the number of threads per inch (TPI) and determines the level of detail that can be achieved. Lower mesh counts allow more ink to pass through, suitable for low-resolution designs, while higher mesh counts are ideal for fine detail. In the printer setup process, both the angle and the squeegee pressure are critical, applying the right amount of pressure and holding the squeegee at the optimum angle ensures that ink is transferred accurately without smearing.[111,114] Also the off-contact distance, the gap between the screen and the substrate, must be precisely adjusted to prevent smearing or incomplete prints (Figure 3.6). Among the printing parameters, the velocity plays a key role in the quality and thickness of the printed layer.[113,114] Usually, the thickness of the layers decreases as the speed of the squeeze increases since the lower ink passes through the mesh. The homogeneity of thickness is regulated by the thickness of the emulsion, typically in the range of 10-30 μm.

Apart from the mesh selection and the print setup, tuning the properties of the ink is essential for successful printing. In particular, its viscosity and particle size determine how it flows through the screen and onto the substrate. The particle size of the ink should be less than one-third of the open mesh apertures to avoid clogging and ensure a smooth print.[115] The distance between two threads of the mesh can be comparable with the diameter of the nozzle of the inkjet printing cartridge. Finer particles are used for high-resolution detail, while larger particles are better for large layouts, without high-resolution details.

The viscosity of the ink is also a crucial parameter that must be carefully adjusted to achieve a high-quality printed film.[102,113] The ideal inks are the shear-thinning non-Newtonian inks, as they have higher viscosity without any shear rate applied and do not penetrate the mesh. During the print, when the squeegee passes their viscosity decreases, allowing them to penetrate the mesh. Commercially available screen-printed inks have $\eta < 3$ Pa s for a shear rate around 1000 s^{-1}, [116] that is the standard shear rate reached when the paste passes through the mesh in the screen-printing process. It is also possible to screen print a Newtonian ink, adjusting the parameters of the print, in this case, the η should be around 10 Pa s, around four orders of magnitude more than the inkjet printables ones.[102,116,117] Inks with higher viscosity can be printed as well, tuning printing parameters, and with mesh with larger TPI, decreasing the resolution. Balancing these ink properties with the printing settings is the key to achieving optimum printed layers depending on the desired architecture. It is often necessary to try different mesh counts to achieve the optimal balance between resolution, ink deposition, and printing speed.

The rheological properties of the screen-printable paste are typically adjusted with solvent, binder, and additive. The binder acts as a glue that holds the particles together and ensures adhesion to the substrate once the ink has dried. The solvent is mainly responsible for adjusting the viscosity of the ink, making it fluid enough to pass through the screen mesh during printing. It evaporates after application, allowing the ink to solidify on the surface. Sometimes inks also contain additives that have different functions, such as adjusting flexibility, preventing screen clogging, and increasing the stability of the ink.

The wettability of the substrate is less critical than for inkjet printing because of the lower resolution of the screen printing.[108,109] Nonetheless in any case, in some cases, it is necessary to modify the surface tension of the substrate with some treatment directly on the surface of the substrate, e.g. chemical coating, plasma etching, and temperature treatment.

3.7 State of the art of organic printed TEG

Although many studies focus on the synthesis and optimization of organic TE materials, little has been done on device design. Most printed organic TEGs in the literature primarily demonstrate the TE properties of materials through simple proof-of-concept devices.[118,119] These initial demonstrations, while valuable for showcasing the potential of organic TE, rely on approaches that lack the scalability required for practical applications. The majority of the printed organic TEGs remain confined to small-area devices ($A_{\mathrm{TEG}} << \mathrm{cm}^2$) and a limited number of thermocouples.[120–126] As a result, organic TEGs tend to exhibit low absolute power outputs in the order of pW.[122,125,127]

Making comparisons between printed organic devices is not trivial, as articles often report only power densities without specifying the absolute power measured or the challenges in scaling up the devices. Alternatively, they may report only the absolute power output without specifying the area of the TEG. Neither P_{density} nor P_{out} takes into account the

ΔT_{ext} applied to the device, a key factor for a fair comparison, as device power increases with ΔT_{ext} (equation 3.18). One of the most comprehensive methods for comparing devices is the normalized power density $P_{\text{norm density}}$ (TEG power factor) which involves calculating the power per unit area at $\Delta T_{ext} = 1\text{K}$:

$$P_{norm\ density} = \frac{Pout}{A_{TEG}\, \Delta T_{ext}^{\ 2}} = \frac{P_{density}}{\Delta T_{ext}^{\ 2}} \tag{3.35}$$

For a more equitable comparison, only works presenting printed organic TEGs and providing all the necessary information to calculate this parameter were selected (Figure 3.7). As can be seen from Figure 3.7, this parameter varies significantly, ranging from 1×10^{-7} to 0.01 $\mu\text{W K}^{-2}\text{cm}^{-2}$, indicating that further research is needed to optimize it. Given the wide range of this parameter, we analyzed how much of the variation could be attributed to the differences in the thermoelectric properties of the materials or the quality of the device structure. We decided to plot the $P_{\text{norm density}}$ vs. Z_{opt}. Considering the Z_{opt} as the equivalent quality factor of the materials (equation 3.14). The higher the Z_{opt} the higher the normalized power should be for the same quality of device structure. Figure 3.7 shows the $P_{\text{norm density}}$ vs. Z_{opt} of printed TEGs organic (red squares) and hybrid organic/inorganic TEGs (blue circles). It is important to note that this section considers also devices with non-printed steps, which usually improve performance, but also significantly increase production costs.

As can be observed in the case of organic TEGs, despite the significant improvement in the properties of thermoelectric materials, the $P_{\text{norm density}}$ does not show the same progress, highlighting that the devices have not been optimized to maximize the power output. This shows significant potential for improving device performance by better exploiting the TE properties of materials.

Progress toward practical applications, TEGs should also be compared based on shelf life, production cost, scalability, reproducibility, and portability. The shelf life is not reported for any printed organic TEG and rarely for non-printed organic TEG, such as textile TEG. This is due to the general instability of n-type TE materials as described in Chapter 2.

Chapters 4 and 5 present two types of organic TEGs with features consistent with the thermoelectric properties of the materials, demonstrating scalability with devices containing up to 800 thermocouples, and excellent environmental stability along with a record normalized power density among organic TEGs.

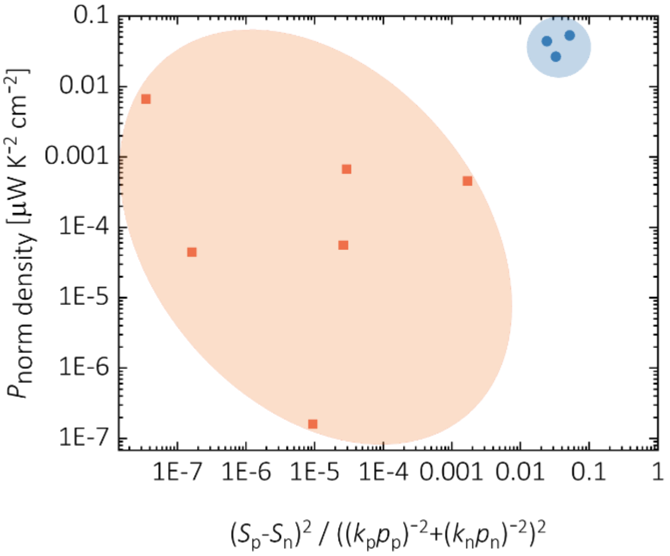

Figure 3.7: State of the art of organic printed TEG. Power provided by the TEG normalized for 1 cm^2 and ΔT=1K as a function of Z_{opt}. The red squares are the organic printed TEG,[122,125,126,128,129] while the blue circles are the hybrid printed TEG.[83,130,131]

3.8 State of the art of inorganic printed TEG

Research on inorganic TEG devices is more developed, as the performance of inorganic materials is better and more stable, producing higher power output. In recent developments, printable thermoelectric materials have been successfully employed for the production of printed TEGs, offering high versatility in processing and adaptability across various printing techniques and applications.[22,120,132] Due to the ability to create thick layers with these materials, screen printing[72,75,77,81,83,84,133–137] and dispenser printing[69–71,73,78,138–140] are the most commonly utilized methods in the literature. Additionally, techniques such as 3D printing, inkjet printing, and aerosol-jet printing have demonstrated high resolution.[74,141–149]

Figure 3.8 shows the $P_{\text{norm density}}$ of state of the art of printed thermoelectric devices. It was not possible to refer solely to fully printed thermoelectric devices due to a lack of fully printed devices in the literature. As can be seen at present, printed inorganic devices have roughly 2 orders of magnitude higher power than printed organic ones. Given the presence of significantly different architectures, such as radial, vertical, folded, and wrapped structures, we decided to present a comparison between $P_{\text{norm density}}$ and P_{out} for a ΔT_{ext} = 1K to understand the role of the areas of the device.

Figure 3.8 shows that the $P_{\text{norm density}}$ remains more or less constant, while the P_{out} for a 1K temperature difference increases, suggesting that the power increase is often due solely to the increase in the number of thermocouples, and not to the optimization of materials or architectures, which can still be improved.

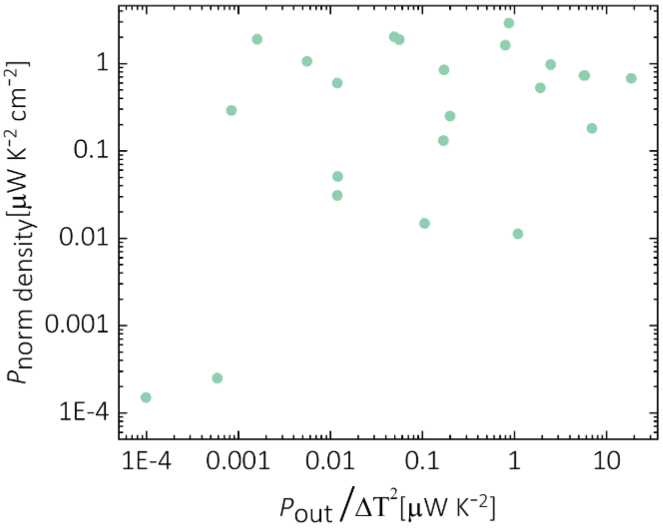

Figure 3.8: State of the art of inorganic printed TEG. Power provided by the TEG normalized for 1 cm^2 and ΔT =1K as a function of the power output for a ΔT= 1K. Expand the analysis of the state of the art comparison shown in the ref[150] (licence CC BY-NC 4.0).

Regardless, with a $P_{\text{norm density}}$ of 1 μW K^{-2} cm^{-2} is already possible to obtain a P_{out} of 30 μm per cm^2 at ΔT = 30 K enough to power a low-power start-up circuit. Despite this, not many studies show the device powering a start-up circuit and being used in an application, probably due to the scaling difficulties, especially of the non-printed manufacturing steps, reliability, durability, and integration challenges. In Chapter 6, a fully printed vertical structure capable of powering a customized PCB (Printed Circuit Board) will be presented, demonstrating a cost-effective energy harvesting system.

4.1 Fully Printed Vertical, Scalable Organic TEG

This chapter presents a scalable method for fabricating TEG using a fully screen-printed process, demonstrating both its reliability and adaptability. The architecture is first validated using the well-known p-type material PEDOT:PSS and silver ink. Then, a recently reported additive-free graphene ink[68] *is used alongside silver to fabricate a TEG with improved performance. The ultra-light graphene-based TEG delivers 15 nW of power at a* $\Delta T = 29.5$ *K. Numerical simulations using COMSOL Multiphysics are used to confirm the reliability of the TEGs.*[b] *Following the successful free-additive graphene-silver 1×1 cm² demonstration, the architecture is scaled up to 10×10 cm² devices consisting of 800 thermocouples. The fabrication process is carried out at an industrial scale in ambient conditions, allowing multiple TEGs to be printed simultaneously. This significantly reduces both production time and cost and represents a major step forward in the development of organic TEGs.*

The results presented in this chapter have been previously published as a journal article in Advanced Materials Technologies.[151]

4.2 Introduction

As described in Chapter 2 organic materials are well suited for flexible TEGs due to their ease of solution processing, natural abundance, lightweight, and great mechanical properties. However, despite the ongoing improvements in the TE properties of organic materials, device architectures have not fully exploited these advances.

Only a few works in the field of organic thermoelectric have presented studies on architectures and fabrication methods of truly scalable devices (further discussion in section 3.7).[120,129,152–154]

The devices presented are generally proof-of-concept demonstrations, aimed at showing the feasibility of creating a device. These proof-of-concept TEGs generally provide power outputs considerably below the predicted performance based on the FoM (zT) of the constituent materials and are often fabricated using methods that are not suitable for scaling. In particular, fully printed TEG have a limited area ($A_{\mathrm{TEG}} \ll \mathrm{cm}^2$) and a low number of thermocouples up to 60 thermocouples (Table 4.1),[122,125,127,155] further limiting their power output.

---

[b] performed by M.Sc.Federico Ferrari supervised by prof. Dr. Jan Anton Koster (Groningen university). Partner of the Horates project.

Table 4.1. Number of thermocouples integrated into a fully printed organic TEG and the printing technique used to fabricate it.

Refs	**Number of thermocouples**	**Printing technique**
[31]	10	3D print
[32]	6	Dispenser print
[33]	60	Drop cast
[34]	4	Inkjet print
[35]	20	Inkjet print
[18]	1	3D print
[36]	9	Spray coat
This work	800	Screen print

4.3 TEG structure design

A π-shape vertical structure,[156] with the legs perpendicular to the heat flow, was chosen to increase the number of thermocouples per unit area and enhance the P_{density}, while simultaneously improving thermal contact with the heat source and sink. This design is also better suited to real-world applications where it is more likely to capture heat flow effectively compared to a planar configuration. The monolithic TEG architecture was reproduced via a full-screen printing process using metallic, insulating, and semiconducting inks. To ensure scalability and reproducibility, all the fabrication steps were carried out using an industrial high-throughput screen printing machine (Thieme 3010S Vision). Given the limited availability of air-stable TE organic n-type materials,[157] as described in section 2.7, we decided to replace the n-type legs with conductive Ag interconnections.

The TEGs presented in this work, are fabricated by simply printing five different layers on top of each other, as shown in Figure 4.1b-f (device with n=8). The first screen-printed layer is the silver bottom contact (3 μm thick), necessary for interconnecting the thermoelectric legs (Figure 4.1b), followed by an insulating layer with circular holes that define the thermoelectric legs (Figure 4.1c). The legs are alternately filled with p-type and silver ink to form the p-TE legs (Figure 4.1d) and the metallic legs (Figure 4.1e), respectively. Finally, the top contact (3 µm thick) is printed to connect all the thermoelements (Figure 4.1d).

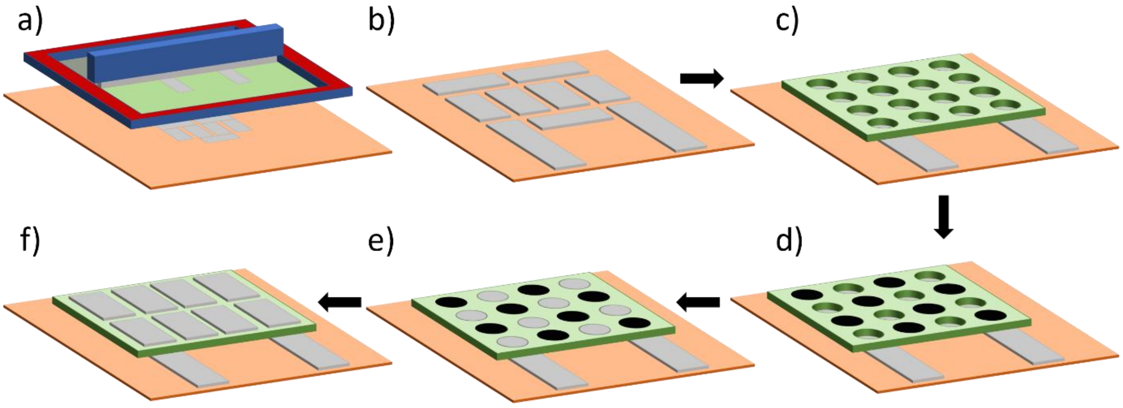

Figure 4.1: a) Sketch drawing of the screen-printed technique. b) Printed bottom silver contact layer. c) Printed insulator layer. d) Printed p-type material (Graphene, PEDOT:PSS) legs layer. e) Printed silver legs layer. f) printed top silver contact layer. Figure from [151] Licence CC-BY.

The top and the bottom contacts (Figure 4.1b,f) are made using the commercially available Ag ink *LOCTITE*® ECI 1010 E&C purchased from *Sigma-Aldrich*, while the insulator is the UV-curable Bectron DP8446 purchased from *Elantas* (Figure 4.1c). A flexible 25 µm Kapton substrate supplied by *DuPont Teijin Films* was chosen to ensure good flexibility and mechanical strength.

Using this method and the same basic thermocouple cell, TEGs with $n = 4$, $n = 8$, and $n = 800$ vertical thermocouples and an area of 0.5 cm^2, 1 cm^{2,} and 100 cm^2 respectively, were fabricated. Figure 4.2 shows the layouts of the five stacked layers of an 8-thermocouple TEG. The silver top and bottom contacts (red and blue rectangles) have dimensions of 4500 µm × 2000 µm and are spaced 500 µm apart. The insulator (depicted in purple) measures 1 × 1 cm, and the wells have diameters of 1500 µm, spaced 1000 µm apart. The dimensions and the spacing of the elements were chosen to optimize the yield of the printing process. All the layers were printed at RT, and the annealings of the printed layers were fast and at low temperatures (<100°C), highlighting how these devices can be produced under standard conditions and with low-cost treatments. Lastly, to electrically insulate the devices, a thin layer of parylene (1 µm) was deposited using the commercially available SCS PDS 2010 Labcoter® 3. The geometry factor *FF* (equation 3.17) of the presented architecture is 0.28, which is reduced by half (*FF* = 0.14) if the n-type organic TE material is replaced by metal interconnections since the silver does not have any contribution to the power output.

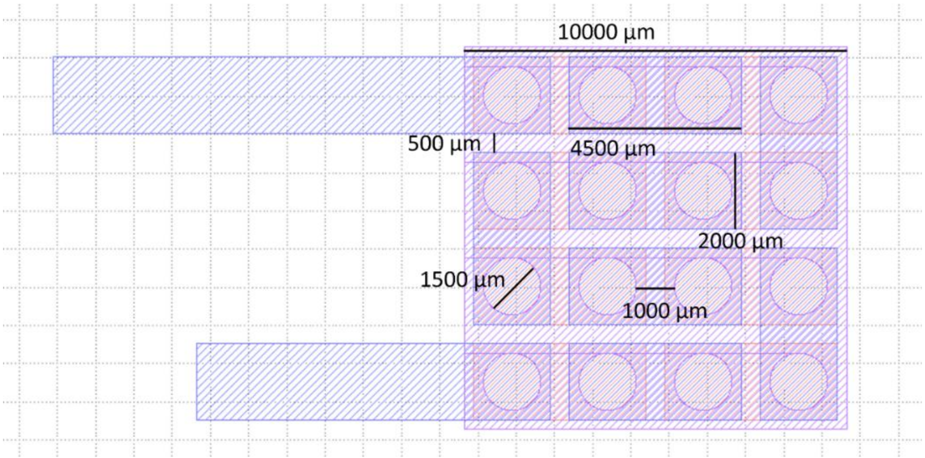

Figure 4.2: Layout of a TEG with 8 thermocouples. Figure from [151] Licence CC-BY.

4.4 Validation of the structure: PEDOT:PSS-Ag TEG

Firstly, the fully printed TEG architecture was validated using PEDOT:PSS, the most commonly used p-type material. The Clevious™ SV4 PEDOT:PSS ink, purchased by *Heraeus*, was used to print the p-TE legs, Figure 4.1d.

4.4.1 Thermoelectric characterization of the PEDOT:PSS

The initial step involved thermally and electrically characterizing the PEDOT ink. As described in Chapter 2, for a complete characterization of a TE material, it is necessary to measure electrical conductivity (σ), thermal conductivity (k), and the Seebeck coefficient (S). The in-plane electrical conductivity was measured using the standard 4-probe method with a 2612B Keithley SourceMeter, and it was found to be 37 S/cm for a screen-printed 4×4 cm square with a thickness of 10 µm, measured with a *Dektak* profilometer. The in-plane Seebeck coefficient was measured using a *Quasi-Static* method with a system carefully described in ref[158] (provided by the Istituto Italiano Technologia during the secondment) and it was found to be 12 µV/K. Furthermore, the thermal conductivity $k = 0.5$ W/mK was measured using the *Linseis* TFA at temperatures up to 80°C, as shown in Figure 4.3. Resulting in a $zT = 3\times10^{-4}$.

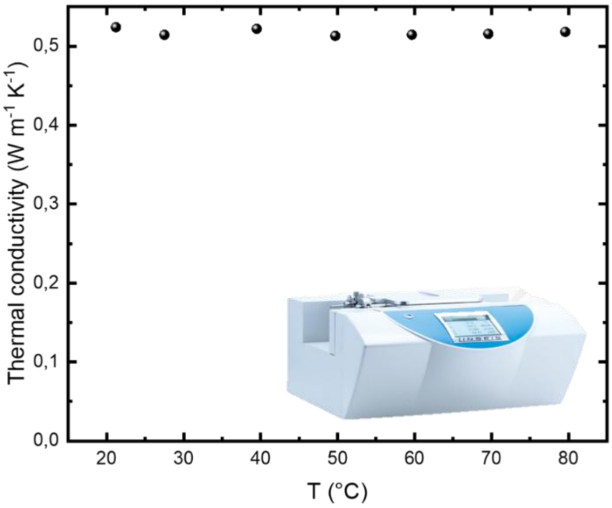

Figure 4.3: Thermal conductivity of PEDOT:PSS as a function of the temperature. Measured with the *Linseis* TFA instrument. Figure from [151] Licence CC-BY.

4.4.2 Characterization of the PEDOT:PSS-Ag TEG

Two variants of the PEDOT:PSS-Ag TEG were fabricated following the steps described above, with n=4 (*P4*) and n=8 (*P8*) thermocouples. Figure 4.4 shows both types of devices, *P4* (Figure 4.4a) and *P8* (Figure 4.4b), respectively. The TEGs had Ag and PEDOT:PSS legs with a thickness of 14 µm thick. The R_{TEG} for the *P4* measured 10.1 Ω, while the R_{TEG} of the *P8* measured 19.2 Ω, perfectly scaled to the number of thermocouples.

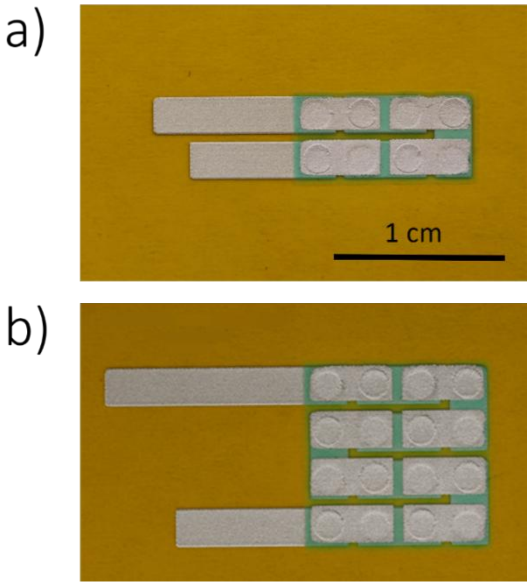

Figure 4.4: a) Picture of the *P4* (4-thermocouples PEDOT:PSS-Ag device). b) Picture of the *P8* (8-thermocouples PEDOT:PSS-Ag device). Figure adapted from [151] Licence CC-BY.

To characterize the devices, the V_{oc}, (open-circuit voltage described by equation 3.1), was measured at different ΔT_{ext}, while the P_{out} was measured at different temperatures as a function of the applied load resistance (R_{load}). The V_{oc} and P_{out} of the TEGs were evaluated with an accurate system described in detail in ref[159] (provided by the Istituto Italiano Tecnologia during the secondment). In short, the voltage and power provided by the device were measured with the device pressed between two copper blocks in a vacuum system to reach an equilibrium, with no convection. The temperature of one copper block was controlled by a water-cooling system and the other by heaters. After setting the desired temperatures, the temperatures of the two copper blocks reached thermal equilibrium, depending on the thermal mass of the device, and the device had a certain ΔT_{ext} across its end. The voltage and power measurements using this setup were taken 5 minutes after reaching this equilibrium. We reported effective ΔT_{ext} ranging from 5K to 25K, to reflect realistic conditions in an IoT scenario. It is important to clarify that here the ΔT_{ext} is the temperature between the top of the parylene and the bottom of the substrate, hence the temperature applied externally to the device. Considering the ΔT across the device as a small temperature difference, the linear approximation discussed in section 3.4 is guaranteed by the measurement setup used.[159] Thus, we were able to consider ΔT between the silver top contact and the silver bottom contact as linearly dependent on ΔT_{ext}, and V_{oc} as linearly proportional to ΔT_{ext}, as demonstrated in Figure 4.5a-b for both *P4* and *P8*. Furthermore, it was possible to observe that the V_{oc} of *P4* and P8, were one-half of the other, as expected since V_{oc} is also proportional to n. The P_{out} also follow the ideal behavior (Figure 4.5c-d) described by equation 3.5 with the maximum value ($P_{out\ max}$, equation 3.6) obtained when the load resistances were matched to the internal resistance. The $P_{out\ max}$ provided by the *P4* was consistently half of that provided by the *P8* at every ΔT_{ext}, further verifying the correct scaling of the P_{out} of the TEGs. Table 4.2 reports the values of the $P_{out\ max}$ for $\Delta T_{ext} = 5$K and $\Delta T_{ext} = 25$K for better comparison.

Table 4.2. $P_{out\ max}$ of the *P4* and the P8 for varying ΔT_{ext}. Note that the $P_{out\ max}$ of the *P4* was measured at 9.3 K and 22.7 K, while the $P_{out\ max}$ of the *P8* was measured at 9 K and 25 K.

TEG	**$P_{out\ max}$ $\Delta T_{ext} \approx$ 9 K [nW]**	**$P_{out\ max}$ $\Delta T_{ext} \approx$ 22 – 25 K [nW]**
P4	0.15	0.93
P8	0.24	1.75

To verify the reproducibility of this architecture, the V_{oc} of two *P8* ($P8_1$, $P8_2$) devices was measured over two consecutive days. Figure 4.6 shows that the V_{oc} varies only marginally, both for the same device on two consecutive days and when between different devices.

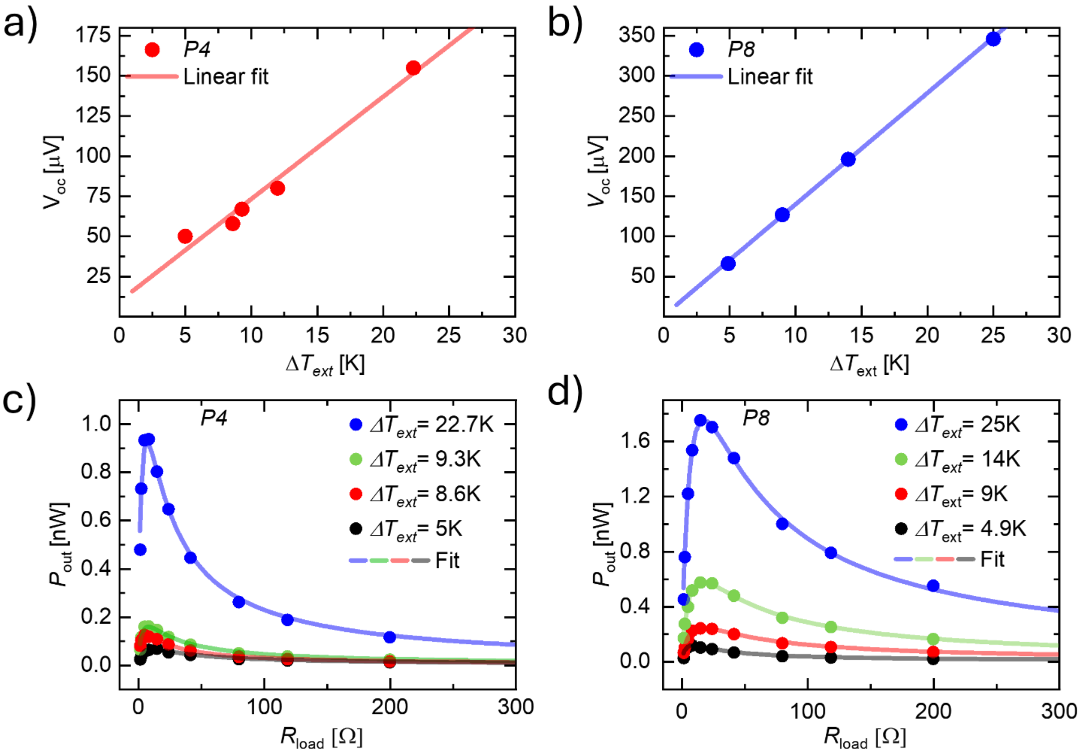

Figure 4.5: a) Open circuit voltage of the *P4* as a function of the ΔT_{ext}. b) Open circuit voltage of the *P8* as a function of the ΔT_{ext}. c) Power output of the *P4* as a function of the resistive load for different ΔT_{ext}. d) Power output of the *P8* as a function of the resistive load for different ΔT_{ext}. The fittings in panels a) and b) are linear fitting, while in panels c) and d) rational polynomials. Figure from [151] Licence CC-BY.

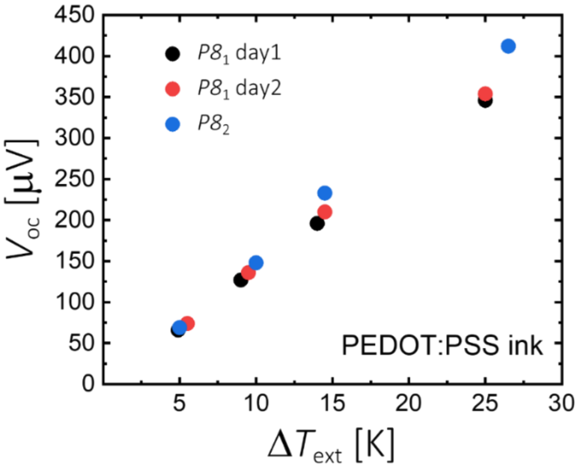

Figure 4.6: Open circuit voltage of the $P8_1$ as a function of the ΔT_{ext} measured on two consecutive days (black dots and red dots), along with the open circuit voltage of $P8_2$ as a function of the ΔT_{ext} (blu dots). Figure from [151] Licence CC-BY.

4.5 Free additive graphene-Ag TEG

After verifying the fully printed architecture with the commercially available Clevious^{TM} SV4 PEDOT:PSS ink, the same architecture was replicated using a new p-type ink additive-free graphene (provided by Swiss Federal Laboratories for Materials Science and Technology) recently presented in the article.[68] In this ink formulation, van der Waals interactions replace the additives to overcome processing challenges, while largely preserving the electrical properties of the material. For further details refer to.[68] The TE performance of the ink was for the first time characterized in this work.

4.5.1 Thermoelectric characterization of the graphene ink

The thermal and electrical properties to evaluate the zT of the screen-printable graphene ink were measured to allow a consistent comparison with the PEDOT:PSS. Firstly, The in-plane S of a screen-printed film 10 cm×2 cm with a thickness of 5 μm was measured, with a custom-built setup. The printed film was placed into electrical contact with the junction of a K-type thermocouple. The junction was specifically kept at the same temperature using a metal block, while another metal block was used to stabilize the temperature at the other ends (see Figure 4.7a). The ΔT at the ends, i.e. the temperature difference between the two blocks, was calculated by measuring the voltage across the thermocouple and evaluating the ΔT with the NIST (National Institute of Standards and Technology) conversion table.[160] For each ΔT, the voltage differences between Chromel and graphene (red dots) and between Chromel and Alumel (blue dots) were measured. The S was then calculated by subtracting the S of Chromel and Alumel from the linear fittings of the ΔV vs ΔT (Figure 4.7b). The measurement on each branch was repeated three times.

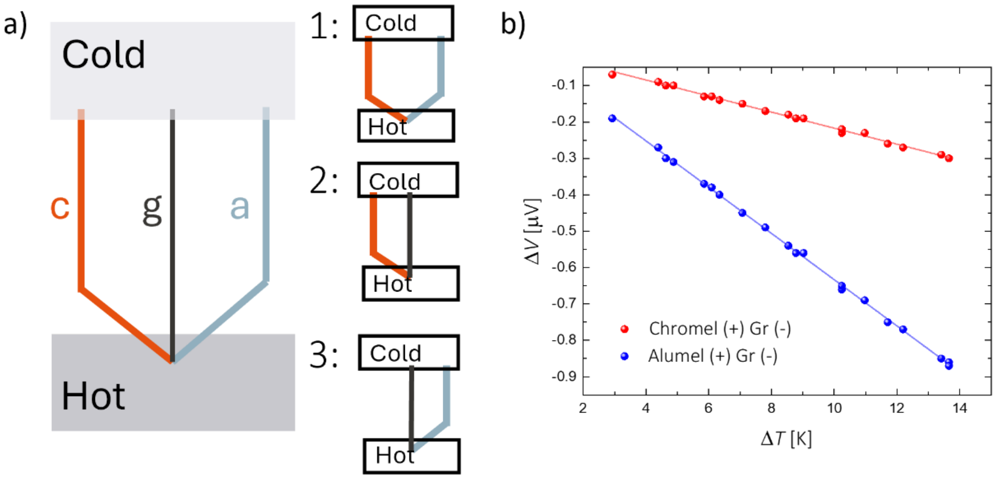

Figure 4.7: a) Sketch of the Seebeck coefficient setup. Step 1. Measurement of ΔV between the Chromel wire (red) and Alumen wire (light blue) to evaluate the ΔT. Step 2. Measurement of ΔV between the Chromel wire and the sample. Step 3. Measurement of ΔV between the Alumen wire and the sample. b) Measurement of ΔV between the Chromel wire and the screen-printed line of graphene (blue line), and ΔV between the Alumen wire and the screen-printed line of graphene (red line). The fits in panel b) are linear fits. Figure from[151] Licence CC-BY.

The two *S* values obtained from the two branches were averaged to determine the final *S* of graphene, obtaining an S = 48 ± 0.42 μV/K. Note that this method was previously demonstrated with silver wires and silver screen printed films.

The in-plane σ was measured using the 4-probe method with a 2612B *Keithley* SourceMeter. The measurement was carried out for printed films (4×4 cm square) with different thicknesses (measured with the *Dektak* profilometer). The resulting average σ was 41 S/cm (Figure 4.8a). Finally, the in-plane k was measured using the *Linseis* TFA at temperatures up to 180°C. As shown in Figure 4.8b, k remained stable with a value of around approximately 0.3 W/mK.

In summary, the screen-printable graphene ink demonstrated a $S = 48$ μV/K, a $k = 0.3$ W/mK, and an $\sigma = 41$ S/cm, showing an increase of more than one order of magnitude in $zT = 8\times10^{-3}$, compared to $zT = 3\times10^{-4}$ for PEDOT:PSS.

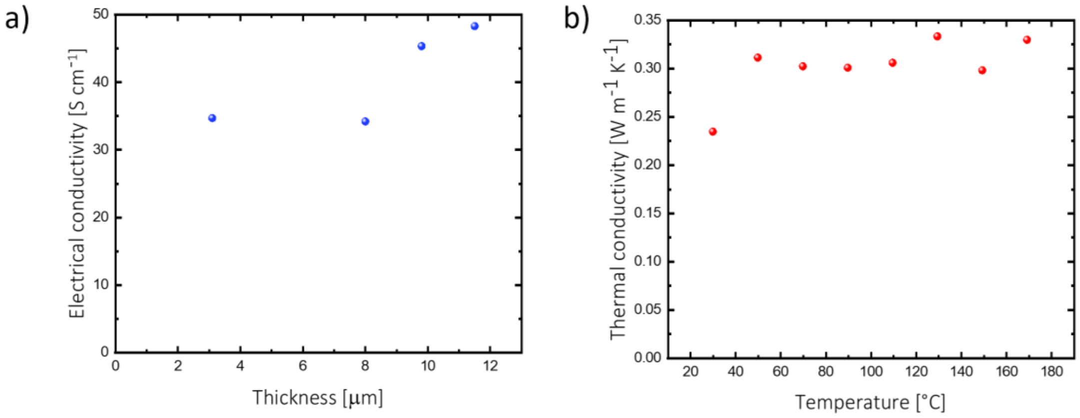

Figure 4.8: a) Electrical conductivity of printed samples as a function of the film thickness. b) Electrical conductivity of the graphene as a function of the temperature using the *Linseis* TFA instrument. Figure from [151] Licence CC-BY.

4.5.2 Characterization of the graphene-Ag TEG

The graphene ink was used to fabricate a 1×1 cm² TEG consisting of 8 thermocouples graphene-Ag (*G8*), mirroring the architecture of the PEDOT device (Figure 4.4b), but with legs 9 µm thick. The *G8* had an internal resistance of 14 Ω.

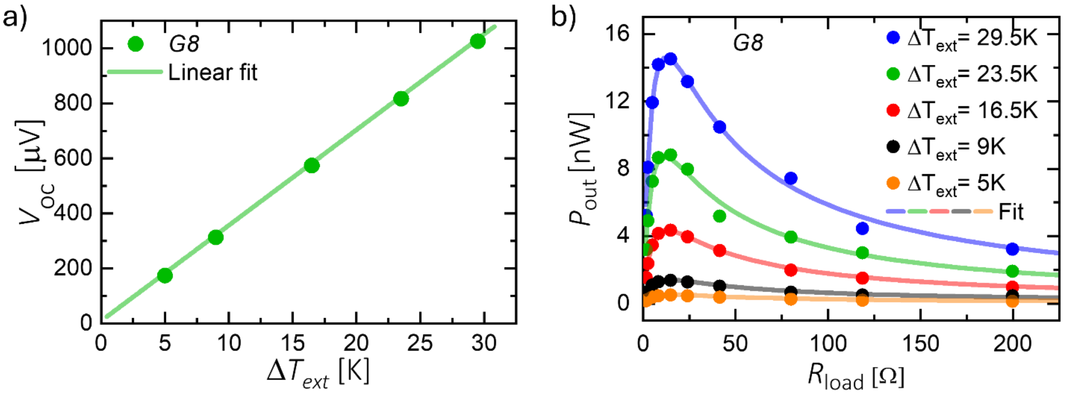

Figure 4.9: a) Open circuit voltage of the *G8* as a function of the ΔT (green dots) with a linear fit (green line). b) Power output of the *G8* as a function of the resistive load for different ΔT_{ext} (dots). The fittings (lines, Fit) in the graph are rational polynomials. Figure from [151] Licence CC-BY.

The V_{oc} and the P_{out} were measured with the same setup employed for the characterization of the PEDOT:PSS TEGs. Figure 4.9 shows that, in both cases, the measured parameters followed the ideal behavior observed also for *P8* and *P4*. This optimal performance underscores both the reliability of the additive-free graphene ink and the screen-printing fabrication method. The $P_{\text{out max}}$ provided by the *G8* is significantly higher than the $P_{\text{out.max}}$ provided by the *P8*, as shown in Figure 4.10, particularly at $\Delta T = 25$ K $P_{\text{out max}}$ of *G8* is 5.5 greater.

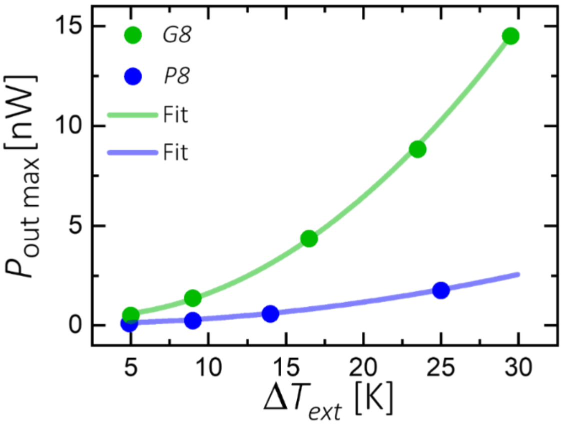

Figure 4.10: Maximum power output of the 8G (green, dots) and the P8 TEG (blue dots), as a function of the ΔText. The fits (lines, Fit) in the graph are exponential. Figure from[151] Licence CC-BY.

The *8G* provided a P_{max} at $\Delta T = 29.5$ K of 15 nW, resulting in a $P_{\text{norm density}}$ (equation 3.35) of 1.7×10^{-5} µW cm^{-2} K^{-2} among the highest for the fully-printed organic TEG. Moreover, this device exhibits a lightweight structure, with a power output of 1 µW per g, and remarkable flexibility up to a bending radius of 1 cm with a maximum resistance change of 2% (Figure 4.11), which are necessary conditions for the use of this device in a real application.

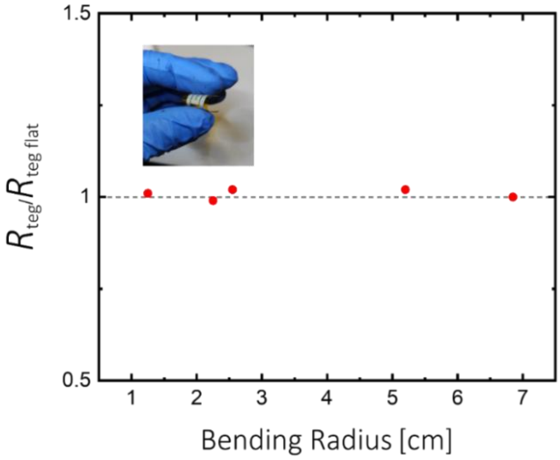

Figure 4.11: Resistance ratios of the screen-printed 8G TEG as a function of the bending radius. Figure from[151] Licence CC-BY.

4.6 Finite-element method simulations

Predicting device performance is one of the fundamental characteristics for the design and optimization of devices, however, it is often not implemented in the world of organic TEGs. In this work, simulations were performed using COMSOL Multiphysics to verify the performance of printed devices. All simulations were carried out using the heat transfer in solids and electric currents interfaces from the thermoelectric Multiphysics package[161] (detailed information can be found in refs[162]). The simulations were conducted by forcing temperatures on two surfaces: the silver top contact (298K) and the bottom of the substrate (298K + ΔT_{ext}), allowing heat to flow freely between the two. Additionally, to recreate the open-circuit condition, one terminal of the device was electrically grounded, while the current was forced to 0A at the other terminal. Figure 4.12 shows the geometries of the simulated devices, which are identical to the printed ones.

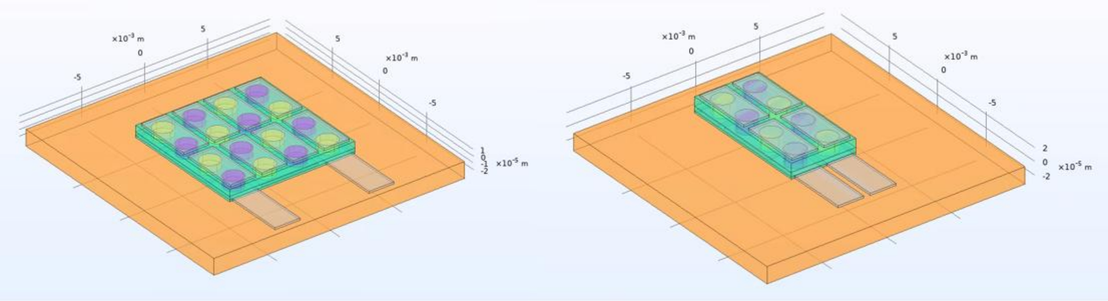

Figure 4.12: Geometries of simulated TEG generators with 8 thermocouples (on the left) and 4 thermocouples on the right. Note that the z-axis is scaled by a factor of 50 to provide a clearer view of the device structure. Figure from[151] Licence CC-BY.

Table 4.3: Material properties used in the simulations.

Material	**σ[S cm^{-1}]**	**k[W m^{-1} K^{-1}]**	**S [μV K^{-1}]**
Graphene	41	0.3	48
PEDOT:PSS	37	0.5	12
Silver	$6.0\text{x}10^{5}$ [92]	400 [92]	1.5[92]
Kapton	/	0.12[163]	/
Insulator	/	0.3[164]	/
Parylene C	/	0.09[165]	/

The simulations were performed with a graphene leg thickness of 8 µm a PEDOT:PSS leg thickness of 13.75 µm (based on the average thickness and peak-to-valley height of the printed films), and a silver contact thickness of of 3µm (the surface roughness was negligible in this case). The dimensions and TE performance parameters used in the simulation are described in Figure 4.2, and Table 4.3, respectively.

The simulation results result were in good agreement with the experimental data, as shown in Figure 4.13. The measured open V_{oc} for both the PEDOT:PSS and graphene-based devices showed an excellent fit with the simulations, with maximum errors of 6.1% and 10.2% respectively.

The strong agreement between the performance of the real devices and the simulated ones highlights the potential for accurately predicting TEG performance using the proposed fully screen-printed fabrication method. Further finite element simulations were performed to identify the current limitations of thermoelectric conversion and to optimize the design and material selection.

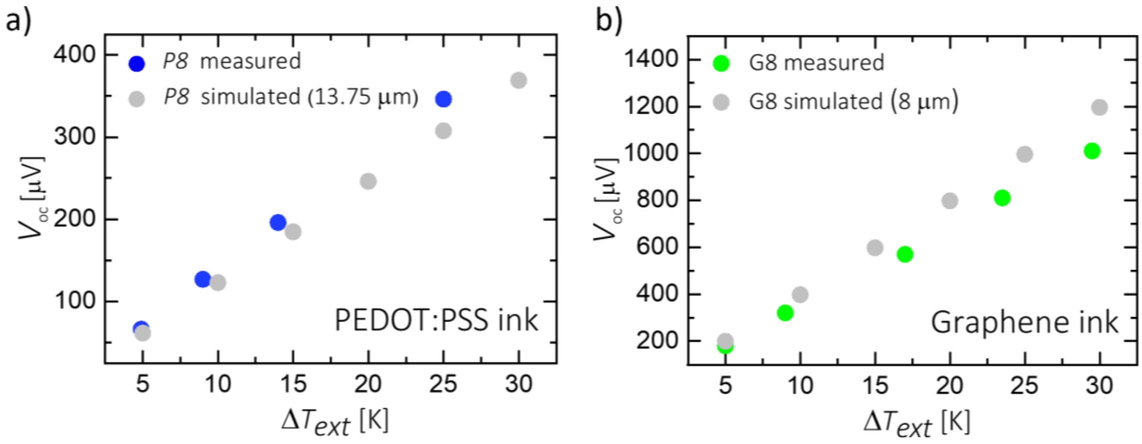

Figure 4.13: a) Measured open circuit voltage of the P8 as a function of ΔText (blue dot) and simulated open circuit voltage of a P8 with a leg thickness of 13.75 µm (grey dot). b) Measured open circuit voltage of the G8 as a function of ΔText (green dot) and simulated open circuit voltage of a G8 with a leg thickness of 8 µm (grey dot). Figure from[151] Licence CC-BY.

First, it was observed that the equivalent circuit model proposed by Beretta,[92] discussed in section 3.4 (Figure 3.2), was not applicable in this case, as the thermal resistance of the device contacts proved to be non-negligible and the ΔT across the legs were almost independent. To gain a deeper understanding of the performance of the device, we introduced a revised equivalent thermal circuit (section 3.5). This new model was developed by calculating the thermal conductance, K, from simulations as the ratio of the heat flux imposed at one end of the segment to the temperature difference measured across the segment. Starting from a complex model (Figure 3.4a), the K values were calculated for horizontal ($K_{//}$) and vertical ($K_{\perp}$) heat flows across all segments. Specific thermal resistances were determined to be negligible, this enabled the construction of the simplified model presented in Figure 3.4b. The proposed model is valid for devices with a standard value of k (see Table 4.3), a thickness on the order of micrometers, and an area size of mm^2. Using this new thermal equivalent, the effect of the substrate on device performance was investigated by simulating the temperature profile along the frontal plane of a *G8* at $\Delta T = 25°C$ with substrate thicknesses of 25 μm and 5 μm. The results shown in Figure 4.14a demonstrated the substrate acts as a thermal barrier, influencing the ΔT across the thermoelectric legs. To analyze the influence of the substrate thickness on the ΔT across legs, we defined a temperature difference, ΔT_{sim}, across the leg:

$$\Delta T_{sim} = (\Delta T_{ext} - \Delta T_{sub-sim}) = \frac{V_{oc-sim}}{n\, S_{pn}} \tag{4.1}$$

Where the $\Delta T_{\mathrm{sub\text{-}sim}}$ is the simulated temperature difference across the substrate and the $V_{\mathrm{oc\text{-}sim}}$ is the simulated open circuit voltage. The different combinations of substrate and graphene leg thicknesses were simulated (Figure 4.14b), demonstrating that increasing leg thickness reduces the influence of the substrate on the ΔT_{sim}. This effect is particularly noticeable with thinner substrate and thicker legs, where ΔT_{sim} closely aligns with ΔT_{ext}. Therefore, decreasing substrate thickness appears to be an effective strategy for enhancing TEG performance.

Furthermore, to assess the influence of the thermal conductivity of the p-type material, silver, insulator, and substrate on the device performance, the $V_{\mathrm{oc\text{-}sim}}$ of a *P4* was simulated as a function of the thermal conductivity of each material (Figure 4.15). In each simulation, the k values of the other materials were held constant, as shown in Table 4.3.

The normalized $V_{\mathrm{oc\text{-}sim}}$ was calculated relative to the $V_{\mathrm{oc\text{-}sim}}$ of the *P4* obtained using the nominal k values.

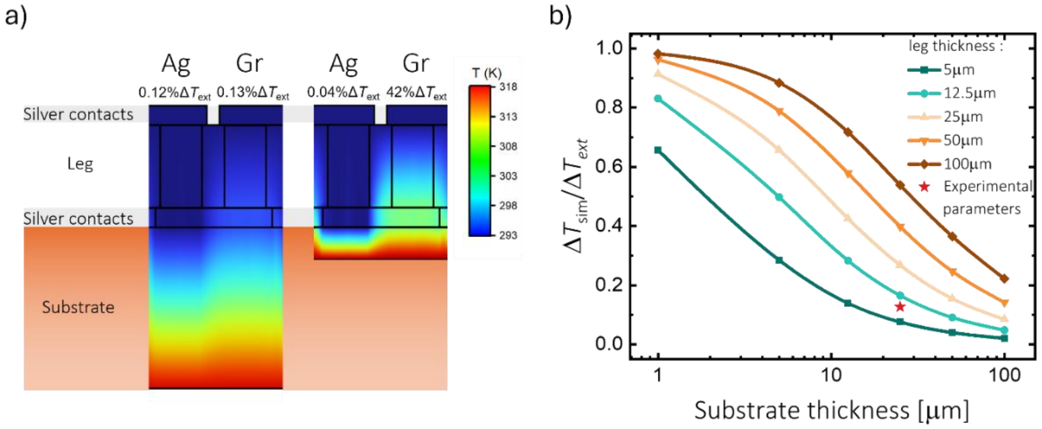

Figure 4.14: a) Temperature distribution along the cross-section of 2 graphene-based devices with a substrate thickness of 25μm (left) and 5μm (right). The temperature drops along the silver and graphene legs are independent of each other. On top of the leg is reported the ΔT drop across the leg. b) Simulated ΔT (ΔTsim) for different combinations of additive-free graphene leg thicknesses and substrate thicknesses. The ΔT is normalized to the ΔText. Figure from [151] Licence CC-BY.

It was observed that the $V_{\text{oc-sim}}$ remains relatively stable when the thermal conductivity of silver varies between 0.1 W m^{-1} K^{-1} and 1000 W m^{-1} K^{-1}. This stability occurs because, at high k, the silver legs are thermally short-circuited (see Figure 4.14a and Figure 4.15c), which limits the formation of a significant temperature gradient across them and thus does not affect the $V_{\text{oc-sim}}$. The $V_{\text{oc-sim}}$ is mainly influenced by the p-type material legs, whose lower thermal conductivity, in contrast to that of silver, allows the development of a thermal gradient (see Figure 4.14a and Figure 4.15b). In the hypothetical scenario of low k of the silver, which would allow a significant thermal gradient, the $V_{\text{oc-sim}}$ would also be affected by the k of the silver. However, due to the very low S of the silver, the changes would not be as significant as those caused by variations in the thermal conductivity of the other materials. The $V_{\text{oc-sim}}$ increases more noticeably when the thermal conductivity of the p-type material and the insulator decreases, while a higher thermal conductivity of the substrate allows for a larger thermal gradient. For example, employing a substrate with a thickness of 25 μm and a thermal conductivity of 0.8 W m^{-1}·K^{-1}[166] could produce a power output up to 15 times greater than that of the Kapton substrates used in the current devices.

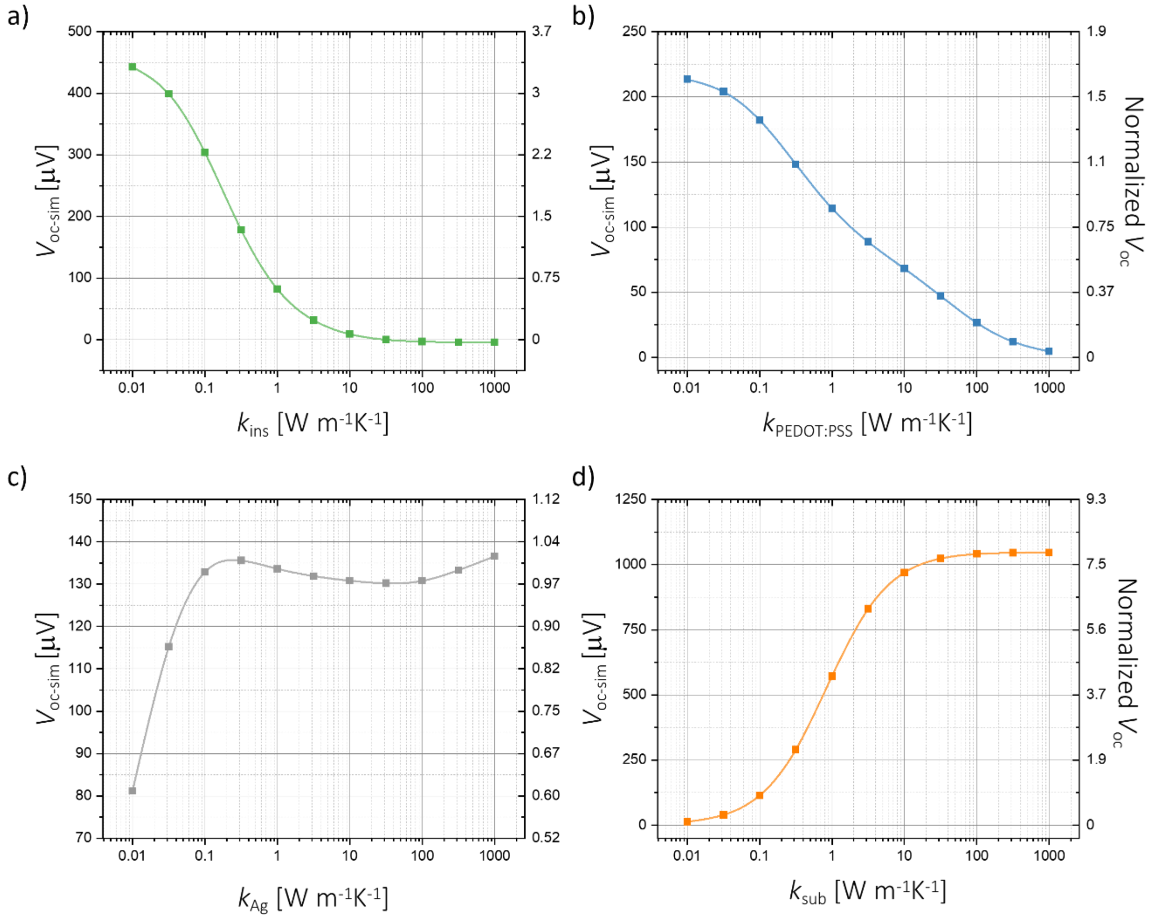

Figure 4.15: Simulated open circuit voltage (Voc-sim) of a P4 when a ΔText = 25 K is applied, as a function of the thermal conductivity of a) the insulator, b) the p-leg, c) the silver and d) the substrate. The open circuit voltage on the left y-axis has been normalized with respect to the open circuit voltage of the P4 device obtained with the nominal values of the k. (reported in Table 4.3). Figure from[151] Licence CC-BY.

Finally, also the thickness of the active material has a significant influence on the $V_{oc\text{-}sim}$, if the thickness increases the power increases until the leg resistance starts to dominate. However, this effect only becomes significant for thicknesses exceeding 50 µm (Figure 4.16), a range that is difficult to achieve with screen printing.

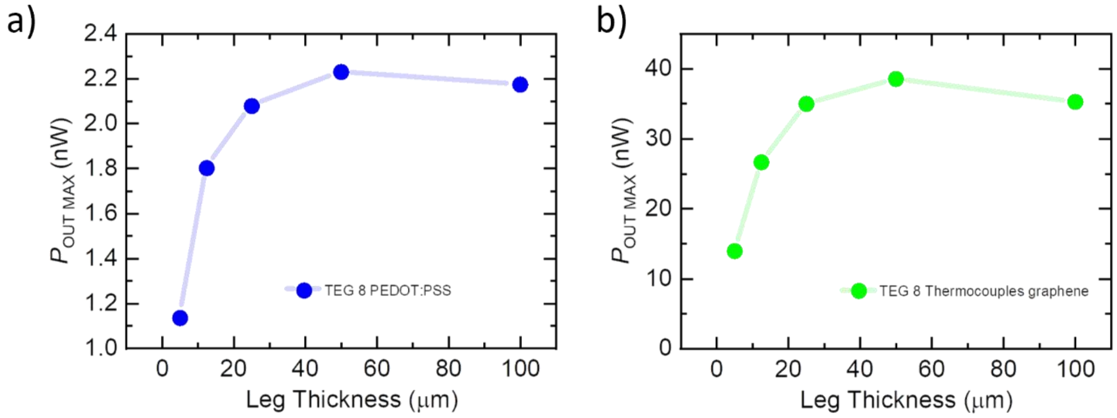

Figure 4.16: a) Simulated maximum power output of a P8 as a function of the leg thickness. b) Simulated maximum power output of a G8 as a function of the leg thickness. The maximum power output was obtained using the simulated open circuit voltage and the value of the internal resistance, which increases proportionally to the thickness, following equation 3.6 since the contact resistance of the device is negligible. Figure from[151] Licence CC-BY.

4.7 Scaled-up free additive graphene-Ag TEG

To demonstrate the scalability of the TEGs produced using the previously described fabrication method, a new batch of devices was screen printed. Figure 4.17 shows graphene-based TEGs n =800 thermocouples with leg thicknesses of 10 µm and 20 µm, each measuring 10 × 10 cm² (*G800 10 µm, G800 20 µm*). For comparative purposes, new TEGs with n = 8, having identical leg thicknesses (*G8 10 µm*, *G8 20 µm*), were also screen-printed. As expected, the internal resistances of the *G800* TEGs increased proportionally with the number of thermocouples and leg thicknesses (Figure 4.18a). The *G8 10 µm* had an internal resistance of 3.4 Ω, and the *G8 20 µm* had an internal resistance of 7.5 Ω, while the *G800 10 µm* and *G800 20 µm* showed internal resistances of 325 Ω and 735 Ω, respectively. This resulted in a percentage error in the R_{teg} of the *G800 10 µm* and *20 µm* of 5% and 2% compared to the R_{teg} of the *G8 10 µm* and *20 µm* multiplied by 100, highlighting the high consistency of the scaling process.

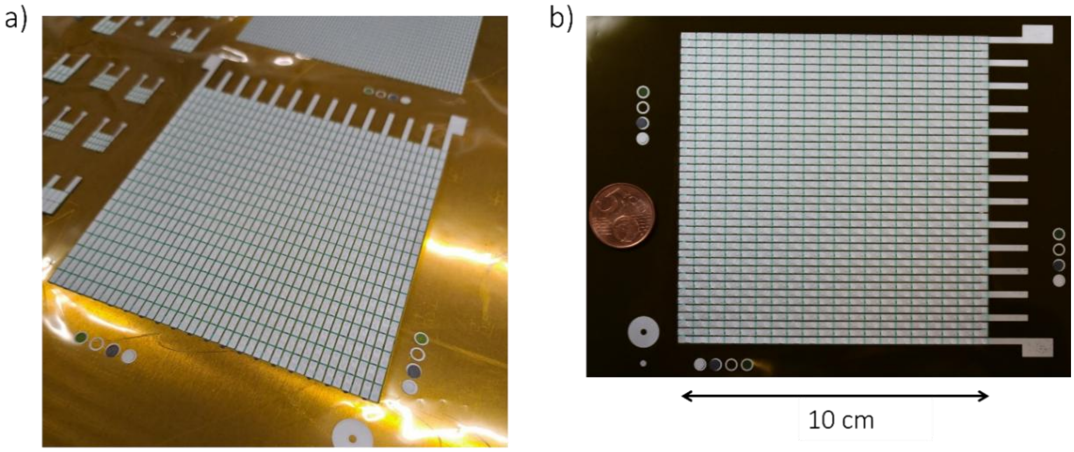

Figure 4.17: Pictures of the *800G* TEG (800-thermocouples graphene-Ag device). Figure adapted from[151] Licence CC-BY.

To further demonstrate the correct behavior and the scaling of the devices the V_{OC} of *G800 10 μm*, *G800 20 μm*, G8 10 *μm,* and G8 20 *μm* were measured as a function of ΔT_{ext} (see Figure 4.18b). The V_{oc} of the *G8* TEGs was found to be 100 times lower than that of the *G800* TEGs at the same ΔT_{ext}. In particular, at $\Delta T_{ext} = 40$ K, the V_{oc} of the *G8* 10 μm, multiplied by 100, was 3.7 mV, showing a 5.1% error compared to the V_{oc} of the *G800 10 μm*. While at $\Delta T_{ext} = 40$ K the V_{oc} of the *G8 20 μm*, multiplied by 100, was 6.8 mV, with a 1.5% error compared to the V_{oc} of the *G800 10 μm*.

We can conclude that both types of TEGs (*10 μm*, *20 μm*) demonstrated excellent scalability, in terms of internal resistance and the V_{oc} provided. As a result, the $P_{\text{out max}}$ of the devices was also scalable. The $P_{\text{out max}}$ for the *G800 20 μm* was 16 nW, which is 106 times greater than the $P_{\text{out max}}$ of the *G8 20 μm* (0.15 nW). For the *G800 10 μm* and *G8 10 μm*, the power ratio was 102, with $P_{\text{out max}}$ values of 10.2 nW and 0.1 nW, respectively.

The two *G800* devices were measured every month for three months to evaluate their behavior over time. Figure 4.19 shows that the V_{oc} of the devices remained unchanged for both thicknesses of the legs. Additionally, the total resistance of the devices after 3 months deviated by only 3.3% and 4.6% for the *G800 10 μm* and *G800 20 μm*, respectively.

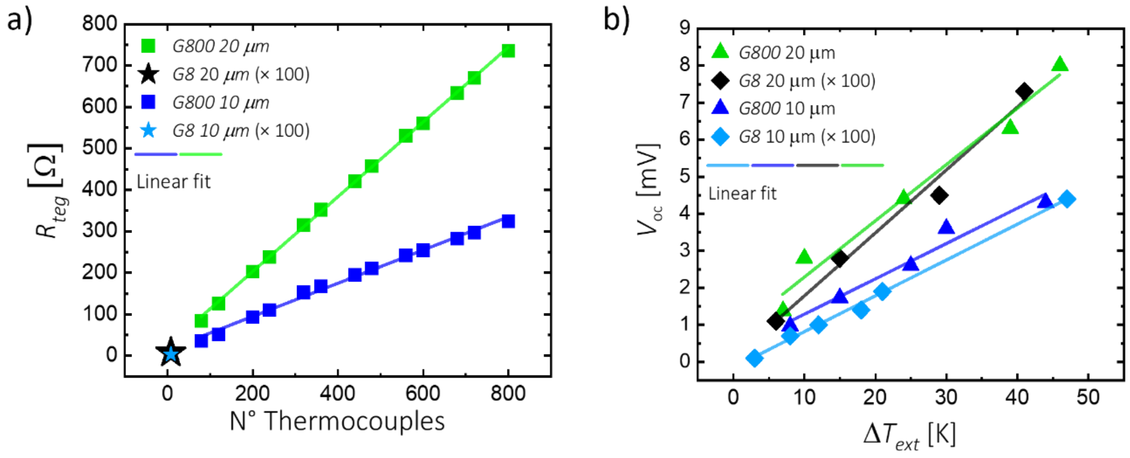

Figure 4.18: a) Mesured internal resistance of the *G800 10 µm* (blue squares) and the *G800 20 µm* (green squares) as a function of number of thermocouples, and internal resistance of the *G8 10 µm* (light blue star) and the *G8 20 µm* (black star). b) Measured open circuit voltage of the *G800 10 µm* (blue triangle), the open circuit voltage of the *G8 10 µm* (light blue rhombus) multiplied by a factor 100, the open circuit voltage of the *G800 20 µm* (green triangle) and the open circuit voltage of the *G8 20 µm* (black rhombus) multiplied by a factor 100 as a function of ΔT_{ext}. The fits in the panels are linear. Figure adapted from[151] Licence CC-BY.

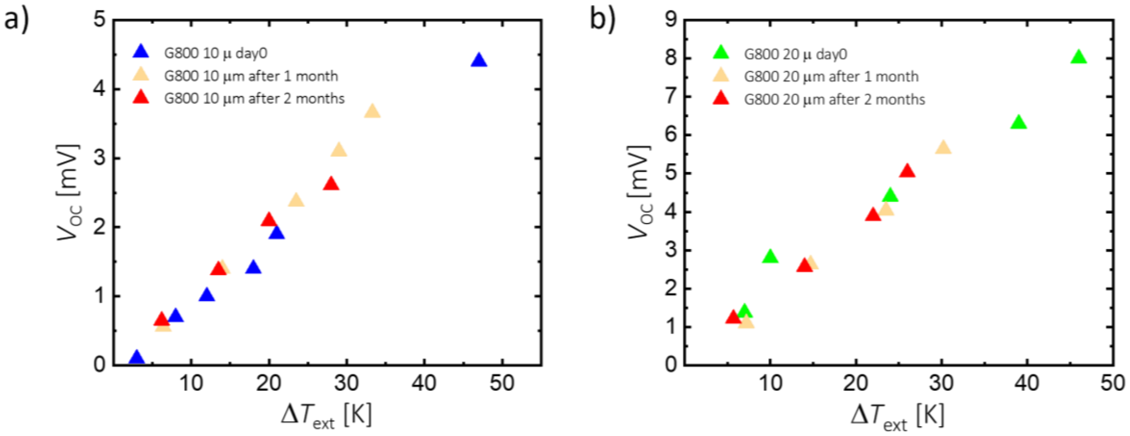

Figure 4.19: Open circuit voltage of the *G800* with a) a thickness of *10 µm* and b) a thickness of *20 µm* as a function of the ΔT_{ext} (between the plates of the hot press) over two months. Figure adapted from[151] Licence CC-BY.

Furthermore, to evaluate the reproducibility of the process, another *G800 µm* was fabricated. Figure 4.20 shows that the two *G800 µm* devices have nearly identical performance, suggesting the reliability and the scalability of the process at least up to tens of cm². Using the same screens employed in the fabrication of these TEGs, it would be easily possible to create TEGs with an area of up to m².

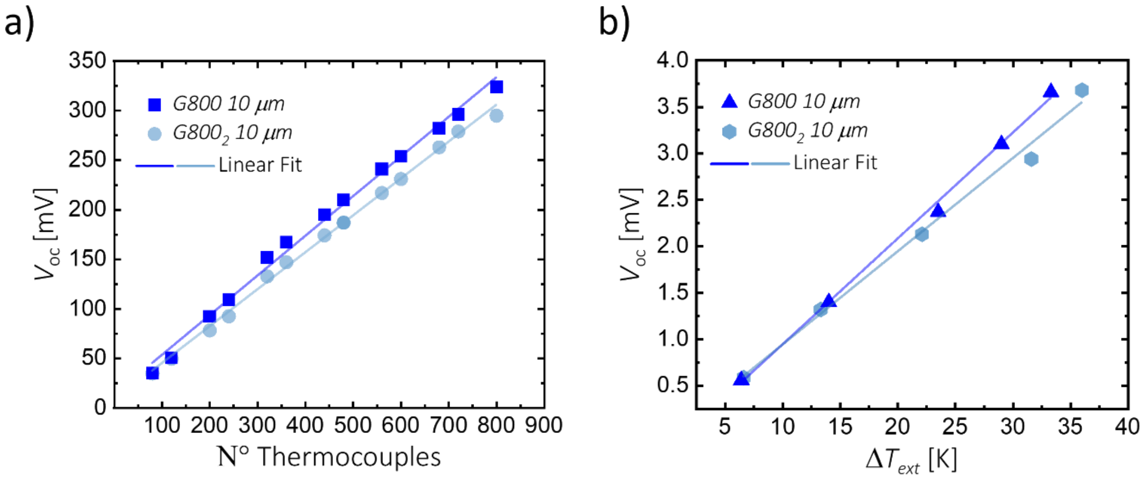

Figure 4.20: a) Internal resistance of two *G800* with a thickness of 10 µm as a function of the number of thermocouples. b) Open circuit voltage of two *G800* with a thickness of 10 µm as a function of the ΔT_{ext}. Figure adapted from[151] Licence CC-BY.

It is important to note that the V_{oc} and P_{out} measurements presented in this section were carried out in a simple setup in air, consisting of a hot press with two metal plates with controllable temperature (provided by the EURECAT Centre Tecnologic during the secondment). Additionally, in this case, the parylene insulating layer was not present, replaced by a thermal insulating paper, which certainly reduced the ΔT. This was due to the incompatibility of the TEG dimensions with the more complex and accurate setup used for the characterization of the *P8* and *G8*. In any case, all the devices were perfectly scalable when measured with the same setup and under the same conditions.

4.8 Summary

This work outlines a fabrication technique for producing robust, large-area, fully printed vertical organic TEGs. The method is simple, cost-effective, and capable of producing flexible, lightweight TEGs scalable to dimensions in the meters square range, a first for organic TEG devices. These TEGs show consistent performance that aligns with simulations based on the FoM of the materials and remain stable for up to 3 months.

The TEG design was initially validated using a common p-type thermoelectric material, PEDOT:PSS, combined with a commercially available conductive silver ink fabricating TEGs with either 4 or 8 thermocouples, each having an area of 0.5×1cm² or 1×1cm², respectively. After confirming the fabrication reliability of the fabrication method, an 8-thermocouple TEG was developed using an additive-free graphene as a p-type material. This lightweight, flexible graphene-based TEG demonstrated a $P_{\text{norm density}}$ of 1.7×10^{-5}μW cm^{-2} K^{-2}, one of the highest reported for fully-printed organic TEGs. Interestingly, the power density may be further improved, as suggested by the Comsol Multiphysics simulation. For instance, using a thinner or more thermally conductive substrate, such as metal foil with a passivation layer, the ΔT across the thermoelectric legs would increase, increasing the power output. Currently, the TEGs use short-circuited n-type legs made from silver ink due to the lack of stable organic n-type ink. Introducing an organic, screen-printable n-type ink with performance comparable to the graphene-based p-type material could potentially double the power output. In addition, the fabrication process is compatible with any screen-printable ink, including inorganic materials with superior thermoelectric properties (see Chapter 6). Using β-Ag_2Se[81] as the n-type and $Bi_{0.5}Sb_{1.5}Te_3$[77] as the p-type material, a 1×1 cm² TEG with legs 14 μm thick on 25 μm thick Kapton foil, could theoretically generate 10 μW of power at a ΔT_{ext} of 30 K, which would be sufficient to power low-power sensors or electronic devices. [167]

Finally, the ability to fabricate fully printed vertical organic TEGs with up to 800 thermocouples has been demonstrated, providing a clear path to significantly enhanced performance.

In conclusion, the versatility of this TEG architecture and fabrication process has been demonstrated through the use of multiple active inks and configurations, offering the ability to tailor the size, materials, and power output to meet specific application needs. This approach shows great potential for developing TEGs capable of harvesting sustainable energy to power distributed sensors and IoT devices under modest thermal gradients.

5.1 Folded Fully Printed Organic TEGs Based on a Stable n-type Polymer

As miniaturized electronics and sensors are increasingly widespread, the need for affordable and adaptable power sources becomes extremely important. Organic TEGs, which can harness waste heat sustainably and cost-effectively, could play an important role in powering future sensor networks. Until now, n-type organic thermoelectric materials have lagged significantly behind their p-type counterparts in terms of performance, especially stability. Recent advances in the development of a stable, highly conductive n-type polymer, poly(benzodifurandione) (PBFDO), are beginning to change this perspective; however, its validation as a suitable ink for scalable manufacturing processes for integration into an organic TEG has yet to be established.

This study focuses on the development, characterization, and optimization of a PBFDO ink adapted to a scalable inkjet printing process. The n-type ink is next incorporated into a screen-printed, folded origami-inspired design, creating a 21-leg PEDOT/PBFDO organic TEG. This device achieves a normalized power density of 0.718 nW cm^{-2} *K*$^{-2}$*, the highest reported for organic TEGs. Furthermore, the TEG demonstrates ambient stability for up to 90 days and proves its suitability for harsh environments, withstanding temperatures ranging from -8 ℃ to 200 ℃ and up to 90% relative humidity, a first for organic TEGs.*

The results presented in this chapter have been previously published as a journal article in Advanced Materials Technologies.[168,c]

5.2 Introduction

TEGs could play a role in future energy solutions as they do not require recharging, can operate without light, and contain no moving parts, overcoming the limitations of batteries, solar cells, piezoelectric, and triboelectric systems. Organic TEGs, offer flexibility and lightweight properties and can be produced using scalable printing techniques. Using non-rare and cost-effective materials, organic TEGs are ideal for use in wearables,[169] agricultural and industrial sensors,[170] and compact point-of-care devices,[171,172] where flexibility, affordability, and compact size are key benefits.

---

[c] collaboration with Dr. Nathan James Pataki supervised by Dr. Mario Caironi (istituto Italiano di tecnologia IIT). Partner of the Horates project

Although, not many devices have been demonstrated using high-throughput and large-area techniques, such as screen printing, roll-to-roll, and inkjet printing,[113,173] and the proposed devices do not generate enough energy to power even the most efficient low-power booster circuits, which require tens to hundreds of μW.[170,174] This is mainly due to the lack of air-stable n-type organic materials after doping, unlike p-type materials, which exhibit stability.[33,175] This is one of the reasons why the architectures presented are often not truly scalable,[173,176] the number of thermocouples is limited, and the device performance measurements are conducted only in controlled environments, often without mentioning any air stability.[129,173,177] As discussed, in Chapter 2, n-type materials generally have σ that are an order of magnitude lower than p-type materials, with maximum values below 100 S/cm.[177–181] The causes of instability and low σ a are many, but the main ones are poor doping efficiency and unstable radical anions due to insufficiently deep energy levels of the lowest unoccupied molecular orbitals (LUMOs).[182] Achieving maximum conversion efficiency in organic TEGs and advancing toward practical power outputs requires the development of both high-performance p-type and n-type materials. The gap between p-type and n-type has been bridged with the discovery of an air-stable, highly conductive n-type polymer, poly(benzodifurandione) (PBFDO), obtained by a simple synthesis, reported in refs.[32,183]

This air-stable n-type polymer, with an $\sigma > 2000$ S cm^{-1}, easy to synthesize, could have the potential to revolutionize the field of organic thermoelectric. Whereas the stability of the material and its high conductivity have been proven, its adaptability to printing techniques and the production of scalable application-focused TEGs remains a challenge.

This work demonstrates the printability of the material and its integration into an origami-inspired, fully printed TEG. The device printed on an ultra-thin parylene substrate achieves a record P_{density} of 2.69 μW cm^{-2} at $\Delta T = 61$ K, and the highest reported $P_{\text{norm density}}$ of 0.718 nW cm^{-2} K^{-2} among other reported organic TEGs. Furthermore, significantly, this work validates, for the first time, the long-term stability in harsh environments of an organic TEG with temperatures ranging from -8 to 200 °C and relative humidity up to 90%. The demonstrated power output and stability, even in challenging conditions, represent a significant advancement toward real-world applications.

5.3 Optimization of a stable printable n-type ink

PBFDO was synthesized according to the previously reported procedure,[32] aiming for a final concentration of 10 mg/mL of PH-BDFO polymer,[184,185] typical for inkjet-printable ink.[d] To obtain the polymer, monomer HBFO 3,7-dihydrobenzo[1,2-b:4,5-b′]difuran-2,6-dione and the radical initiator TMQ (Figure 5.1a,b) were dissolved in DMSO which then underwent quinone radical homocoupling reaction resulting in oxidative polymerization hence yielding PBDFO. The final solution was filtered using a 45 µm Teflon filter and transferred into dialysis sacks with an average molecular weight cutoff of 10 kDa, where it was purified for 2 weeks. The DMSO used for dialysis was replaced until it became colorless which indicated the end of purification (Figure 5.1c). Nearly 30 ml of PBFDO solution in DMSO- were synthesized, as shown in Figure 5.2a,b.

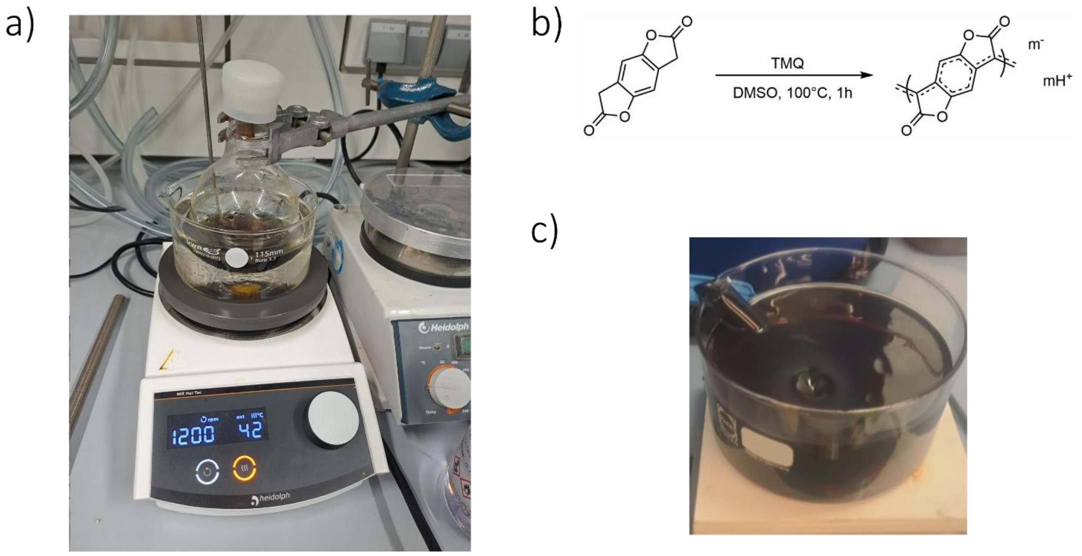

Figure 5.1: a) Photograph of the synthesis of PBFDO in DMSO using TMQ as the radical initiator. b) Reaction scheme of PBFDO. c) Photograph of an early stage of the dialysis.

As described in section 3.6.1 the ink must have specific physical characteristics to be printable. The printability of the ink depends on several factors, such as surface tension, density, and viscosity of the ink, together with the nozzle diameter of the cartridge and the droplet velocity during the print. All these factors are taken into account by the Reynolds *Re* and Weber *We* numbers, described by the equations 3.31 and 3.32. Generally, the quality of the droplet can be predicted from the value of the general dimensionless parameter Z_{print}, expressed in equation 3.33. Ideally, it should have a value between 1 and 10.

---

[d] Synthesis made with the collaboration of M.Sc. Angus Hawkey and M.Sc. Diego Ropero Hinojosa. Partner of the Horates Project.

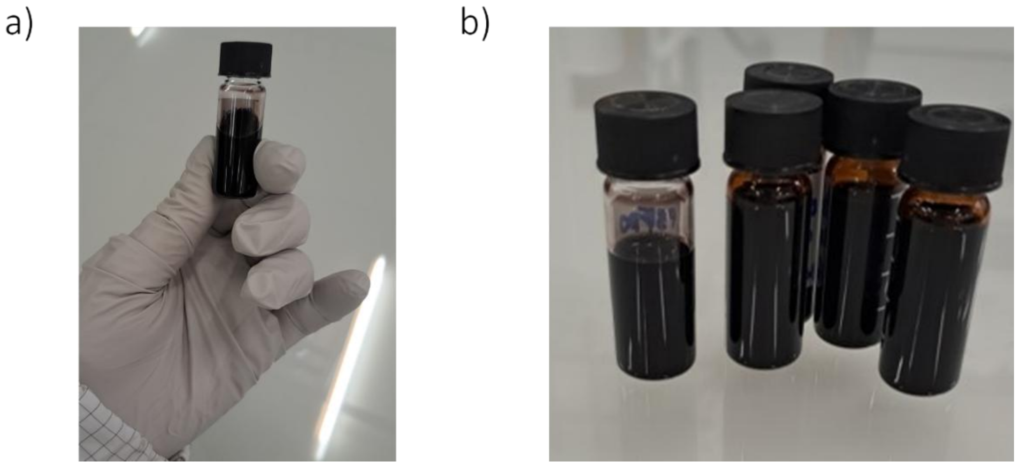

Figure 5.2: Photos of the milliliter-scale synthesis solution of the PBDFO ink. Figure adapted from[168] licence CC BY-NC.

The ink and the printing parameters of the PixDro LP50 printer were optimized to give a print droplet velocity of 5.4 m s^{-1} (Figure 5.3a), a viscosity of 7.5 mPa·s (Figure 5.3b), a surface tension of 47.38 mN m^{-1} (Figure 5.3c), and an ink density of 1.1 g cm^{-3}. It can be seen from Figure 5.3b that the ink is shear-thinning non-Newtonian and is therefore suitable for printing as described in section 3.6.1. The viscosity was measured with the m-VROC microchannel rheometer at T= 30 °C, while the surface tension was measured with a *Krüss* DSA100 drop-shape analyzer. The density of the ink was obtained by weighing different volumes of the ink with a *Sartorius* Analytical Lab balance at RT.

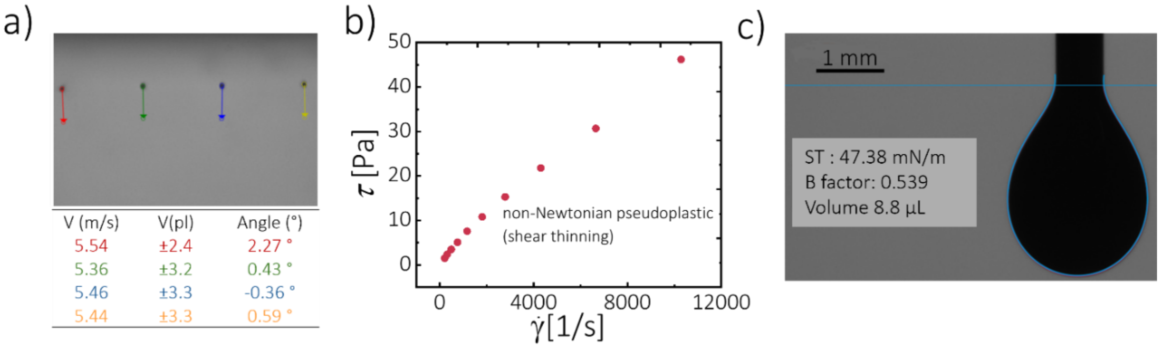

V (m/s)	V(pl)	Angle (°)
5.54	±2.4	2.27 °
5.36	±3.2	0.43 °
5.46	±3.3	-0.36 °
5.44	±3.3	0.59 °

Figure 5.3: a) Fluid drop velocity during the printing, together with the angle and the volume of the drop. The velocity is expressed in m/s, the volume in pl, and the angle in °. The colors of the rows correspond to the characteristics of the drops with the arrow of the same color. b) Measurement of ink viscosity: shear stress [Pa] as a function of the shear rate [1/s]. c) Surface tension of the droplet of the PBFDO ink. Figure adapted from[168] licence CC BY-NC.

The *Re* and *We* numbers of the ink are reported in Figure 5.4, which also shows that the ink has a $Z_{print} = 4.14$, in the desired range for optimum droplet formation, preventing the formation of satellite droplets and splashing. Other parameters were adjusted to improve the quality of the film on the substrate, such as the temperature of the plate, which was set at 80°C. The printability was proven on various surfaces: polyimide, parylene, ethyl cellulose, glass and silicon.

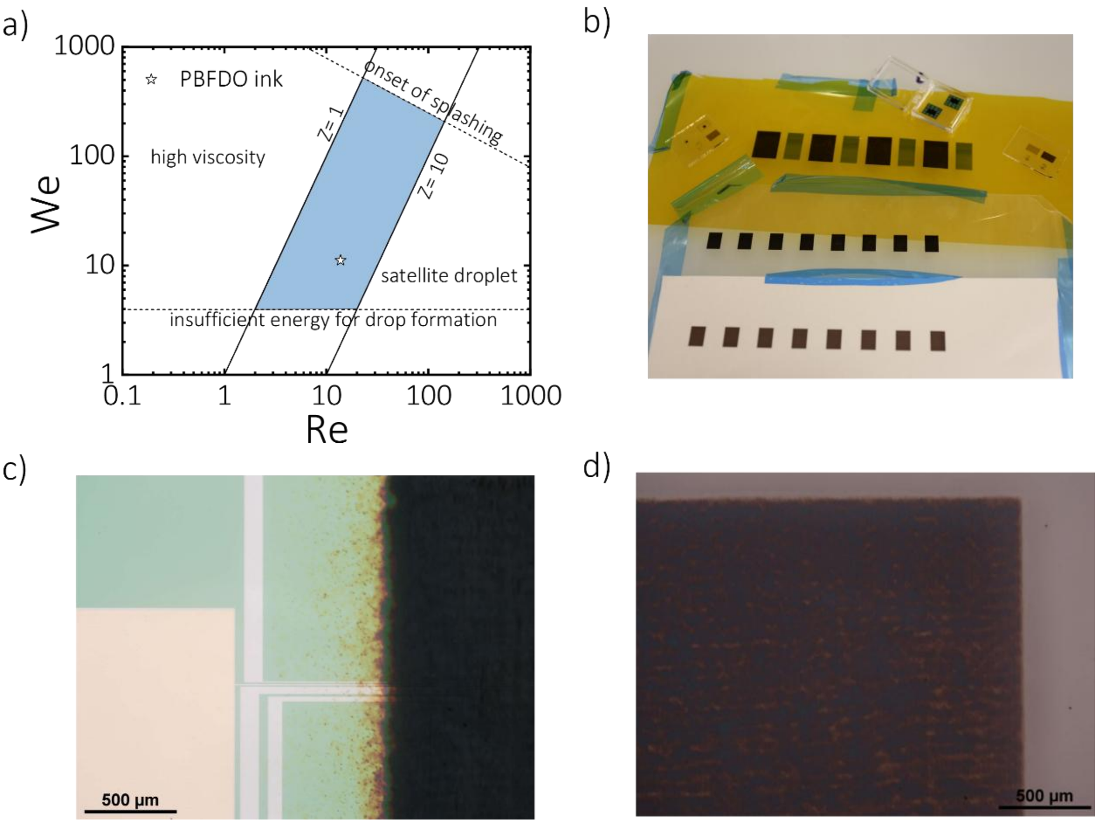

Figure 5.4: a) Weber *versus* the Reynolds number. The area of $1 < Z_{print} < 10$ is shown in blue and represents the area of good printability. The Z_{print} of the PBFDO ink is within the printability zone (white star). b) Photograph of PBFDO film on different substrates: polyimide, parylene, ethyl-cellulose, glass, and silicon. c) Optical micrograph of a printed PBFDO film on a silicon chip (Linseis chip). d) Optical micrograph of a printed PBFDO film on a laboratory slide. Figure adapted and integrated from[168] licence CC BY-NC.

5.4 Thermoelectric characterization of the printed PBFDO

To analyze the behavior of the printed layers, it was chosen inkjet-printed PBFDO films on glass, a substrate that allows for a more accurate profile thickness measurement, with various thicknesses ranging from 31 nm to 293 nm. The sheet resistance (R_s) was measured using a 2612B *Keithley* SourceMeter, and the σ was calculated as follows:[186]

$$\sigma = \frac{1}{R_S\, t} \tag{5.1}$$

Figure 5.5 shows that the in-plane σ of the printed films was constant as a function of the thickness of the layer, indicating that the behavior of the printed films remained unchanged despite the increasing number of printed layers, an important consideration for scalable manufacturing.

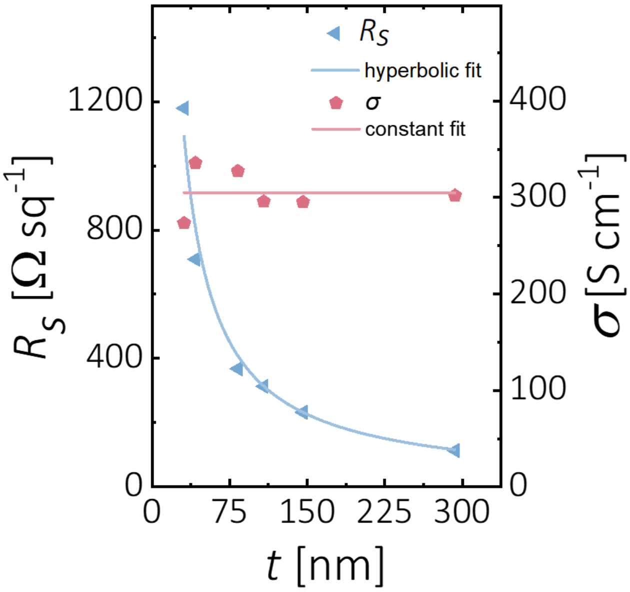

Figure 5.5: Electrical conductivity (red pentagons) with a constant fitting (red line) and sheet resistance (blue triangles) with a hyperbolic fitting of printed PBFDO films with respect to the thickness of the printed film. Figure adapted from[168] licence CC BY-NC.

The σ alone, however, does not allow for a full analysis of the material from a thermoelectric perspective. To calculate the zT, it is also necessary to measure the S and the k. A complete analysis of the material was conducted using the *LINSEIS* Thin Film Analyzer. 4 µm of PBFDO were printed onto the membrane of the chip provided by the manufacturer, and the S, σ, and k were measured as a function of the temperature. At RT the σ, S, and k were found to be σ=175 S cm^{-1}, S=–20 µV K^{-1}, and k=2.2 W m^{-1} K^{-1}. While the S and the σ were previously reported in ref (for spin-coated film),[32,183] k was measured here for the first time, and consequently, the dimensionless figure zT was also evaluated for the first time. All the measured parameters are reported in Figure 5.5 and Figure 5.6.

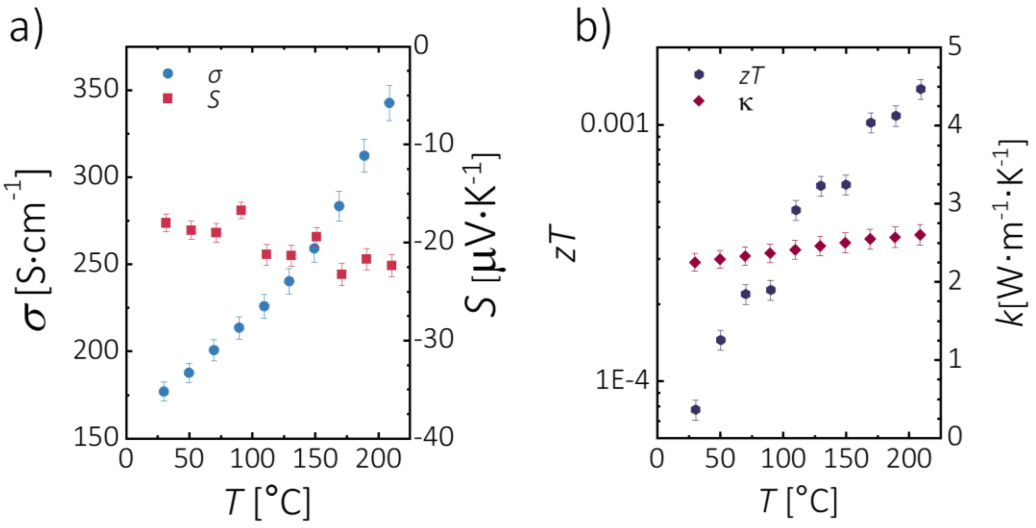

Figure 5.6: a) Measured electrical conductivity (blue circles, left-axis) and Seebeck coefficient (red squares, red-axis) of an inkjet printed PBFDO film as a function of the temperature. b) Evaluated zT (blue hexagons, left-axis), and measured thermal conductivity (red diamonds, right-axis) of the inkjet printed PBFDO film as a function of the temperature. Figure adapted from[168] licence CC BY-NC.

The relatively high thermal conductivity observed in this PBFDO printed film may be tentatively linked to the lack of soft, solubilizing side chains typically found in nearly all other organic thermoelectric polymers. Without these side chains, phonon-like waves can propagate over greater distances with no scattering, leading to a more significant thermal lattice contribution that can be demonstrated to be predominant. Figure 5.6c shows the behavior of the k as a function of T. The value of k is the result of two contributions: the lattice and electronic components (equation 2.22). The k_{lat} should be temperature-independent within the thermal range analyzed, making it possible to calculate the k_{lat} value by simply determining the intercept of the linear fit (1.67 W m^{-1} K^{-1}) and the electron contribution from the slope of the fit. According to the Wiedmann-Franz law (equation 2.24), if the slope of the linear fit m is known, the L can be calculated as:

$$L = \frac{m}{\sigma} \qquad (5.2)$$

Thus, the value of L was evaluated at RT, $L = 1.14\ 10^{-8}$, and it turns out to be close to the theoretical value $L_0 = 2.44\ 10^{-8}$, highlighting how the previous assumption of k_{lat} being independent of temperature was reasonable, and how, based on the obtained values, it is plausible to conclude that k_{lat} is predominant at room temperature (k_{lat} accounts for 70% of the total k).

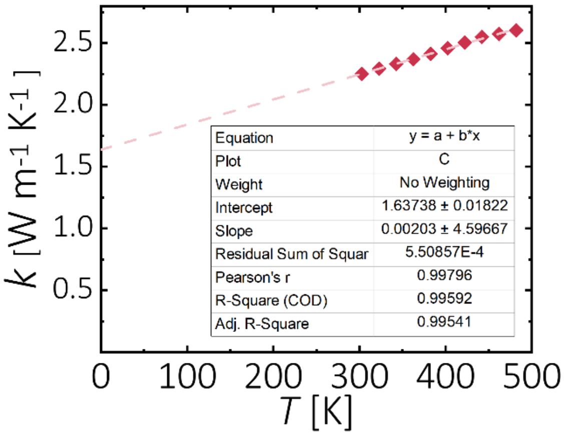

Figure 5.7: Measured thermal conductivity as a function of the temperature (red diamonds) for DMSO-based PBFDO printed film. The fit is a linear fit (light red dashed line). Figure from[168] licence CC BY-NC.

The S of the printed PBFDO film is very close to the value measured in the previously published article.[32] On the other hand, the σ of the printed film is lower than the value stated for spin-coated films in previous studies.[32,183]

The variation in measured σ is likely due to differences introduced by the deposition methods. For example, a recent study involving PBFDO-coated silk yarn for thermoelectric applications reported an electrical conductivity of only $\sigma = 13\ \mathrm{S\ cm^{-1}}$, attributing that to differences in nanostructure arising from processing techniques.[187]Another important factor that might contribute to the lower conductivity could be the introduction of structural defects along the polymer backbone, such as the isomerization from isoxindigo to dibenzonaphthyrone, which can occur if synthetic conditions are not precisely controlled.[183,188] This is likely the case in our work since we carried out the synthesis in a laboratory that is more focused on device fabrication rather than chemical synthesis. In other words, the imprecise synthesis conditions could lead to the incorporation of unwanted units being incorporated into the PBFDO backbone during polymerization, affecting the performance of the material.

Furthermore, we can observe that S, remains almost constant, Figure 5.6a (right-axis), while the σ changes, Figure 5.6a (left-axis), with temperature, albeit in a relatively moderate manner. A more detailed analysis of the temperature dependence of the conductivity for a better understanding of the transport mechanism shows that σ increases with increasing temperature, indicating a weak activation typical of low-doped disordered semiconductors, as previously observed.[189]

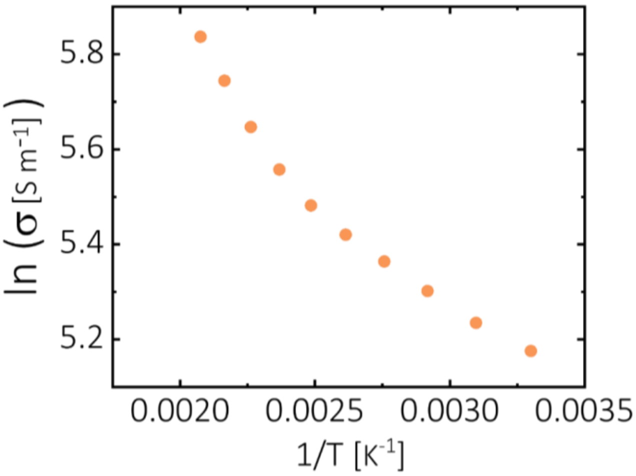

Figure 5.8: Natural logarithm of the measured electrical conductivity as a function of the inverse of temperature [K^{-1}] for DMSO-based PBFDO printed film. Figure from[168] licence CC BY-NC.

On the other hand, in the log-log plot of the reduced activation energy $W = [d(\ln\sigma)/d(\ln T)]$ *versus* temperature (see Figure 5.9), a positive trend emerges, pointing towards a metal-like behavior common for heavily doped disordered semiconductors. The apparent inconsistency in the attitude of the polymers shown in Figures Figure 5.8, and Figure 5.9 suggests that the material is in a critical regime, where common charge transport models cannot be applied, as already suggested by the article.[32]

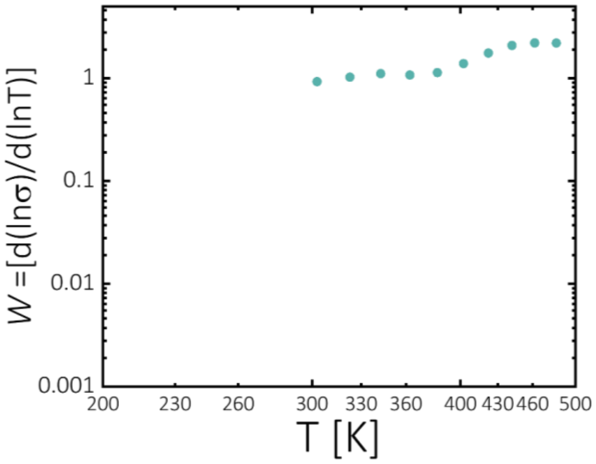

Figure 5.9: Log-log plot of reduced activation energy *versus* temperature for DMSO-based PBFDO printed film. Figure from[168] licence CC BY-NC.

5.5 Fabrication of the PBFDO-PEDOT:PSS TEG

After validating the printability of the PBDFO DMSO-based ink, we integrated it into a fully printed scalable organic TEG. The commercially available screen-printable Clevious™ SV4 PEDOT was chosen for the p-type counterpart, and the commercially available screen-printable *LOCTITE*® ECI 1010 E&C silver for printing the metallic interconnections. Both are already used in Chapter *4*.

The folded structure proposed in this work is an advance over previously reported folded structures.[131,150] Firstly, a parylene C layer, 3.8 µm thick, was deposited by chemical vapor deposition on a PEN carrier substrate. This ultra-thin parylene is ideal for minimizing the cross-section of the device (A_{teg}) and thus maximizing the P_{density}. Then the silver and the PEDOT:PSS layers were printed on top of the parylene employing a semi-automatic screen-printed machine (*RokuPrint* SD 05) with two different screen 125-35y/22° *SAATILENE Hi-tex* (Figure 5.10a). Specifically, two layers of silver were screen-printed with an intermediate annealing at 100°C for 5 minutes, followed by 8 layers of PEDOT with an intermediate annealing at 120°C for 15 minutes.

The n-type legs of PBFDO were patterned with a PixDro Lp50 inkjet printer, following a complementary layout to the p-type legs, as shown in Figure 5.10b. The printing was repeated 20 times (20 layers) with the printer plate at 80°C. After printing the last layer, the device was annealed at 90°C for 20 minutes on a hotplate.

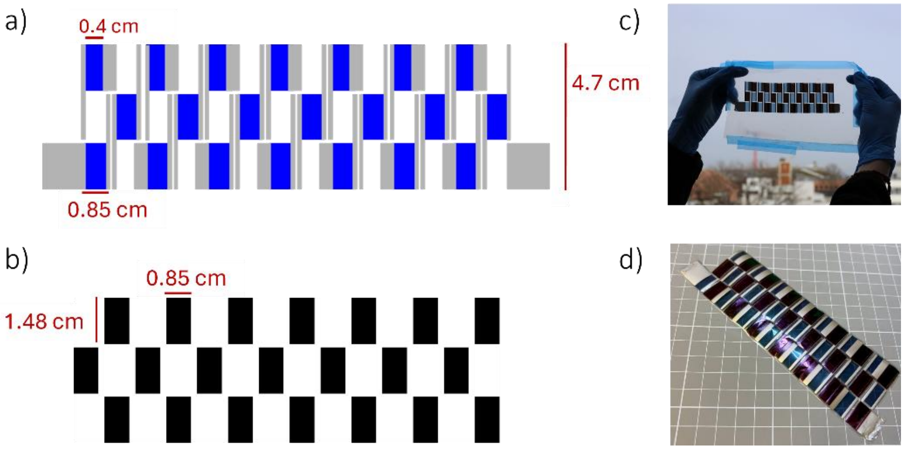

Figure 5.10: a) Layout of the PEDOT:PSS screen and the silver contacts layers, blue areas, and grey areas, respectively. b) Layout of the inkjet-printed PBFDO ink layer, black areas. c) Image of the PEDOT:PSS (blue legs)/PBFDO (black legs) TEG after printing on a thin parylene C layer while on a PEN carrier. d) Image of the PEDOT:PSS/PBFDO TEG after delamination from the PEN carrier. Figure adapted from[168] licence CC BY-NC.

To encapsulate the device, another layer of parylene (0.7 µm) was deposited on top of all the printed layers, as shown in Figure 5.10c. As a final fabrication step, the TEG was delaminated from the PEN carrier (Figure 5.10d) and folded into strips.

The final TEG consisted of 21 thermocouples (14 folded strips), with leg dimensions of 8.5×14.8 mm, and had an internal resistance of $R_{teg} = 1180\Omega$. The maximum thickness of the printed device was 1.7 µm, measured with a *Dektak* profilometer at the contact between the silver and the PEDOT:PSS.

5.6 Characterization of the PBFDO-PEDOT:PSS TEG

After the encapsulation, the delamination and the folding of the TEG (Figure 5.11a-b) it was characterized (in air) by a custom-built measurement setup, shown in Figure 5.11d. More details about this measurement setup are described in Ref. [150]

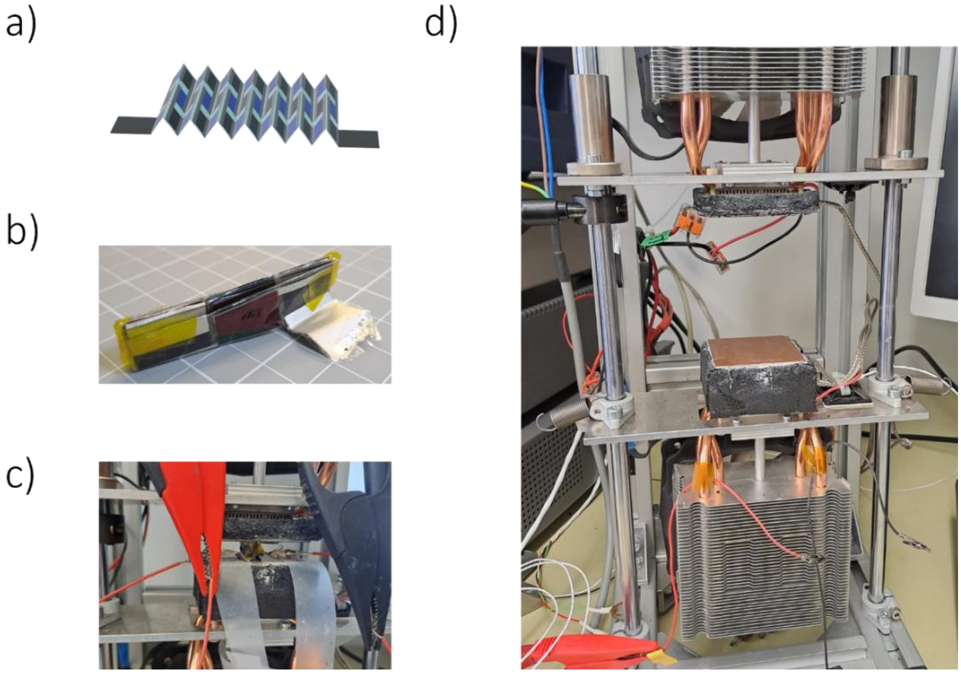

Figure 5.11: a) Sketch of the folding process of the 21-thermocouples TEG. b) Photograph of the folded PEDOT:PSS/PBFDO TEG. c) TEG device under test. d) Custom-built setup used for the measurements. Figure adapted and integrated from[168] licence CC BY-NC.

The current-voltage (*IV*) characteristic of the TEG was measured using the maximum power point tracking after establishing a stable ΔT_{ext} between the copper blocks. The organic TEG was measured with ΔT_{ext} from 17.7 K to 61.2 K with an accuracy of 0.1K, providing a $P_{\text{out max}} = 0.11 \mu\text{W}$ at $\Delta T_{ext} = 61.2$ K (Figure 5.12). As expected, a linear dependence between V and I was observed, as well as a parabolic dependence between P_{out} and I. The TEG characterization was performed with a cold side temperature ($T_{\text{c\_ext}}$) of approximately 20°C and a hot side temperature ($T_{\text{h\_ext}}$) varying from 20°C to 80°C for an extended duration (over 1 hour). These results demonstrate that the TEG functions effectively even at moderate-high average temperatures on the sample ($T_{\text{m}} = (T_{\text{h\_ext}} + T_{\text{c\_ext}})/2$) truly surprising, especially in the field of organic materials (Chapter 2), for prolonged periods, due to the relatively stable zTs of the organic printed materials. Each curve in Figure 5.12a represents the average of five cycles, repeated every 35 seconds after achieving a stable ΔT_{ext}. The cycles at $T_{\text{m}} = (T_{\text{h\_ext}} + T_{\text{c\_ext}})/2 = (19.9 + 72.6)/2\ °\text{C} = 46.3\ °\text{C}$ are shown in Figure 5.13. The congruence of the curves in the P_{out} of Figure 5.13

and the parabolic fitting of the $P_{\text{out max}}$ in Figure 5.12b (equation 3.6) demonstrated that the performance of the device remained stable even after nearly an hour of measurement.

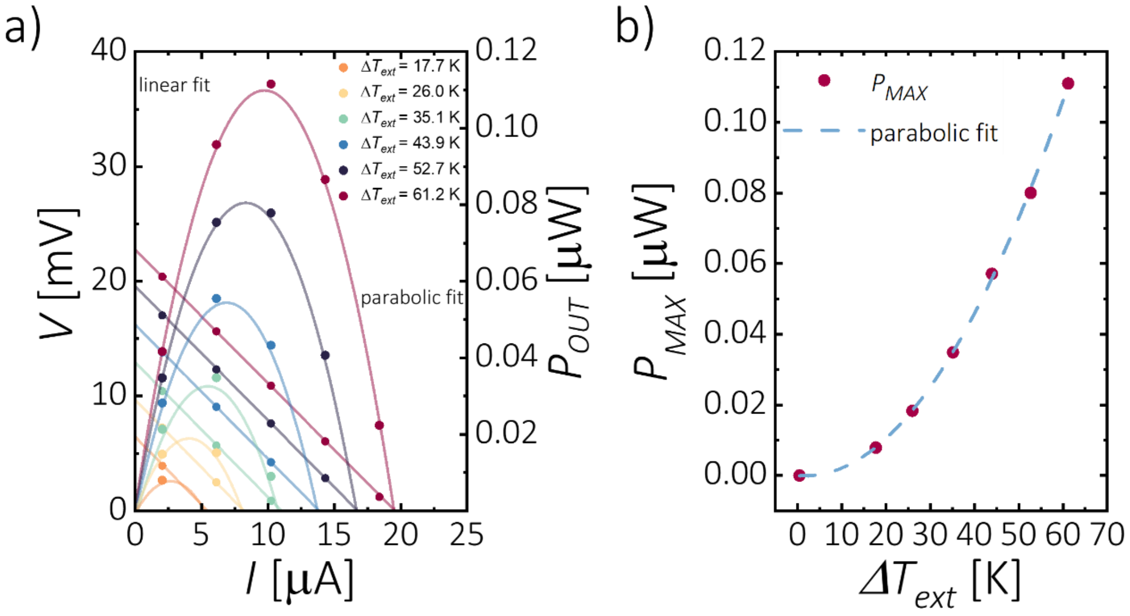

Figure 5.12: a) IV characteristics of the PEDOT:PSS/PBFDO TEG at $\Delta T_{\text{ext}} = 17.7$ K to $\Delta T_{\text{ext}} = 61.2$ K, and evaluated power output. The fits are parabolic (power) and linear (voltage). b) Evaluated maximum power density of the PEDOT:PSS/PBFDO TEG as a function of the temperature gradient. The fit is parabolic. Figure adapted from[168] licence CC BY-NC.

The P_{density} was evaluated with the cross-sectional area of the TEG, since is the area parallel to the heat flow. The theoretical $A_{\text{teg}} = 4.9\times10^{-6}$ m^2 was evaluated considering the width of the device (4.7 cm), the maximum thickness of the printed device (1.7 µm), and the parylene thicknesses (3.8+0.7 µm). The theoretical area was found to be in good agreement with the real area, which was measured using a µm-screw gauge, yielding $A_{\text{teg}} = 4.9\times10^{-6}$ m^2. Consequently, the maximum power density (equation 3.26), was calculated to be $P_{\text{densitity max}} = 2.69$ µW cm^{-2} at $\Delta T_{ext} = 61.2$ K, and the $P_{\text{norm densitity}} = 0.718$ nW cm^{-2} K^{-2} (equation 3.35). This value is significantly higher than those reported for other organic TEGs as shown in Table 5.2.

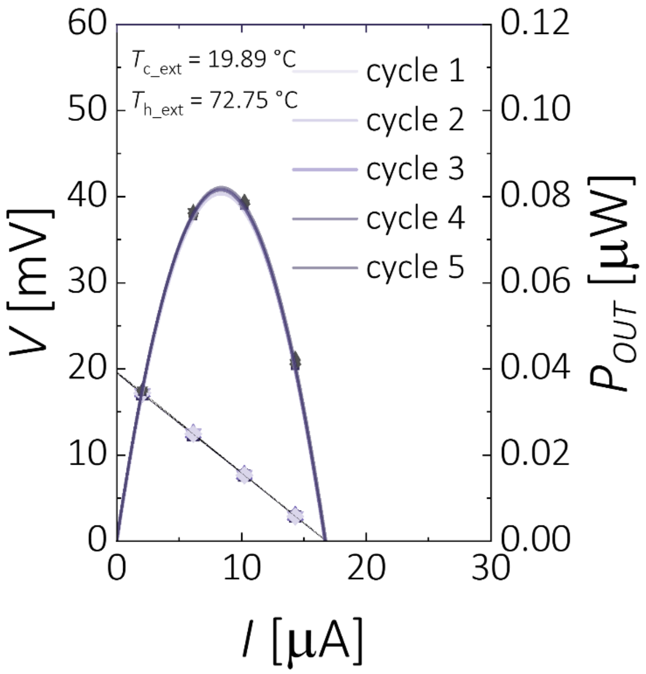

Figure 5.13: Details of Figure 5.12a. *IV* characteristics of the PEDOT:PSS/PBFDO TEG, which has been under test for more than an hour. The metal blocks in this case had a T_{c_ext} = 19.9 °C and a T_{h_ext} 72.6 °C. Figure adapted from[168] licence CC BY-NC.

5.7 Finite element simulations

Finite element analysis simulations were performed with a device consisting of three thermoelements (two folded strips) to verify that the experimental performance of the PEDOT/PBFDO module was consistent with the expected values based on the material properties listed in Table 5.1. A module with three thermoelements was simulated considering the symmetry and repetition of the device (Figure 5.14b). The copper blocks were imposed as heat transfer boundary conditions, with the cold sink block at a temperature of T_{c_ext} = 293K and the hot source block at three different T_{h_ext} = 354.19, T_{h_ext} = 345.72K, and T_{h_ext} = 336.93K. The electrical boundary conditions were set at the silver bottom and top contacts, with one assigned as the ground and the other as the active terminal. Also in this case, the simulations were carried out using the heat transfer in solids and electric currents interfaces from the thermoelectric Multiphysics package, more detail can be found in the reference.[150]

Table 5.1: Material properties used for the simulations.

	S **[µV/K]**	***σ*** **[S/cm]**	***k*** **[W/m K]**	***t*** **[µm]**
PBFDO	20	300	2.2	0.4
PEDOT:PSS	12	37	0.5	1

Figure 5.14a shows the simulated power output of the module, scaled by a factor of seven (2 folded strips, 3 thermocouples, ×7), compared to the experimental power output (14 folded strips, 21 thermocouples), while Figure 5.14b shows the temperature distribution throughout the simulated device geometry. The maximum power outputs from the simulations and experiments are in close agreement, differing by only 9.75% at a ΔT_{ext} of 61.2 K. This small difference is likely due to slight variations in the printed film thicknesses, which are difficult to measure accurately for thin films on flexible substrates, resulting in an overestimation of the simulated resistance. Consequently, the peak power point shifts to lower current values, as $P_{\mathrm{out\ max}}$, and R_{teg} are related by equation 3.6.

The close agreement between the experimental and simulated results reinforces both the scalability of the materials and the reproducibility of the device architecture.

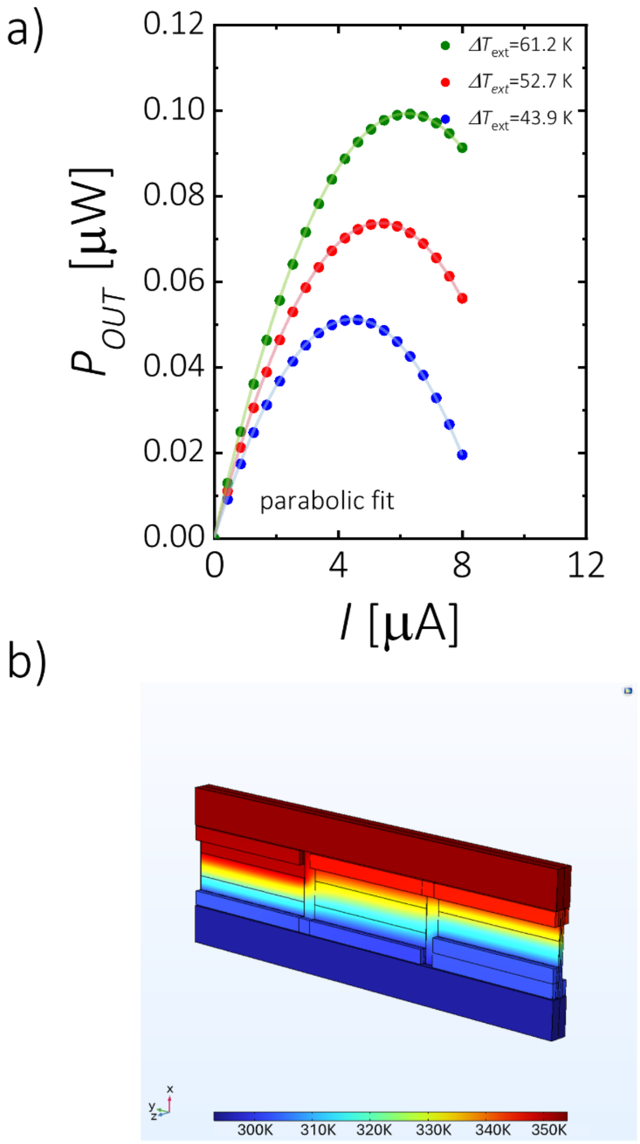

Figure 5.14: a) Simulated power output provided by the PEDOT:PSS/PBFDO module consisting of 2 folded stripes (3 thermocouples) multiplied by a factor 7 obtained using finite element analysis. b) Temperature distribution across the simulated PEDOT:PSS/PBFDO module with a ΔT_{ext} = 61.2 K. Note that the z-axis is magnified by a factor of 50 to give a better understanding of the structure. Figure from[168] licence CC BY-NC.

5.8 Stability in harsh environments

Validating the stability of organic TEGs over time and in environments that replicate potential real-world applications is essential for any device that is intended for practical use. Currently, the stability of p-type, and especially n-type, organic thermoelectric materials remains a challenge, with long-term stability tests rarely reported due to typically poor results.[190–192] The PEDOT/PBFDO TEG presented in this work not only exhibited ambient stability at room temperature for over three months, with less than a 5% change in R_{teg} (Figure 5.16a) but also showed good stability in harsh environments. To validate the stability in harsh environments, a TEG with 6-thermoelements was fabricated (Figure 5.15), on a Kapton substrate, 25 µm thick, following the same process used to print the 21-thermocouple device on parylene, including the parylene passivation layer. The Kapton substrate was selected for its ease of handling, and its flexibility.

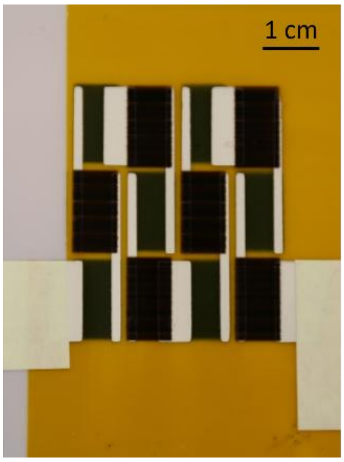

Figure 5.15: Picture of the PEDOT:PSS/PBFDO TEG (6 thermoelements) printed on top of a Kapton substrate after the encapsulation with a 0.7 µm of parylene. Figure from[168] licence CC BY-NC.

The resistance of the TEG was measured at $R_{\text{teg}} = 281\ \Omega$. The device was subjected to a series of environmental stress tests: it was stored in a *Liebherr* Comfort freezer at -8°C for 55 hours (Figure 5.16b), placed in a *Memmert* VO500 PMP500 oven at 200°C for 2.5 hours (Figure 5.16c), and kept in a *Binder GmbH* MKF 115 climate chamber at 90% relative humidity (and RT in a dark environment) for 60 hours (Figure 5.16d). The relative change in internal resistance ($(R\text{-}R_0)/R_0$) was minimal, showing variations of 0.2%, 0.2%, and 1.5%, respectively. This demonstrates that the TEG maintained its internal resistance across a wide range of extreme conditions, from freezing temperatures to high heat and humidity, without significant degradation.

To assess the operational stability of the TEG, *IV* characteristics of the 6-thermocouples device were measured after the environmental stress tests. The device endured 55 hours at -8°C, 2.5 hours at 200°C, 60 hours in 90% relative humidity, and more than four months in ambient RT conditions before showing a $P_{\text{out max}}$ of 0.028 µW and a V_{oc} of 5.8 mV at a ΔT of 55.7 K (Figure 5.17). The resulting $P_{\text{norm density}}$ was 0.771 nW cm^{-2} K^{-2}, which represents a 6.9% increase compared to the 21 thermocouples TEG measured without environmental stress testing. This result highlights the remarkable stability of the TEG under extreme conditions.

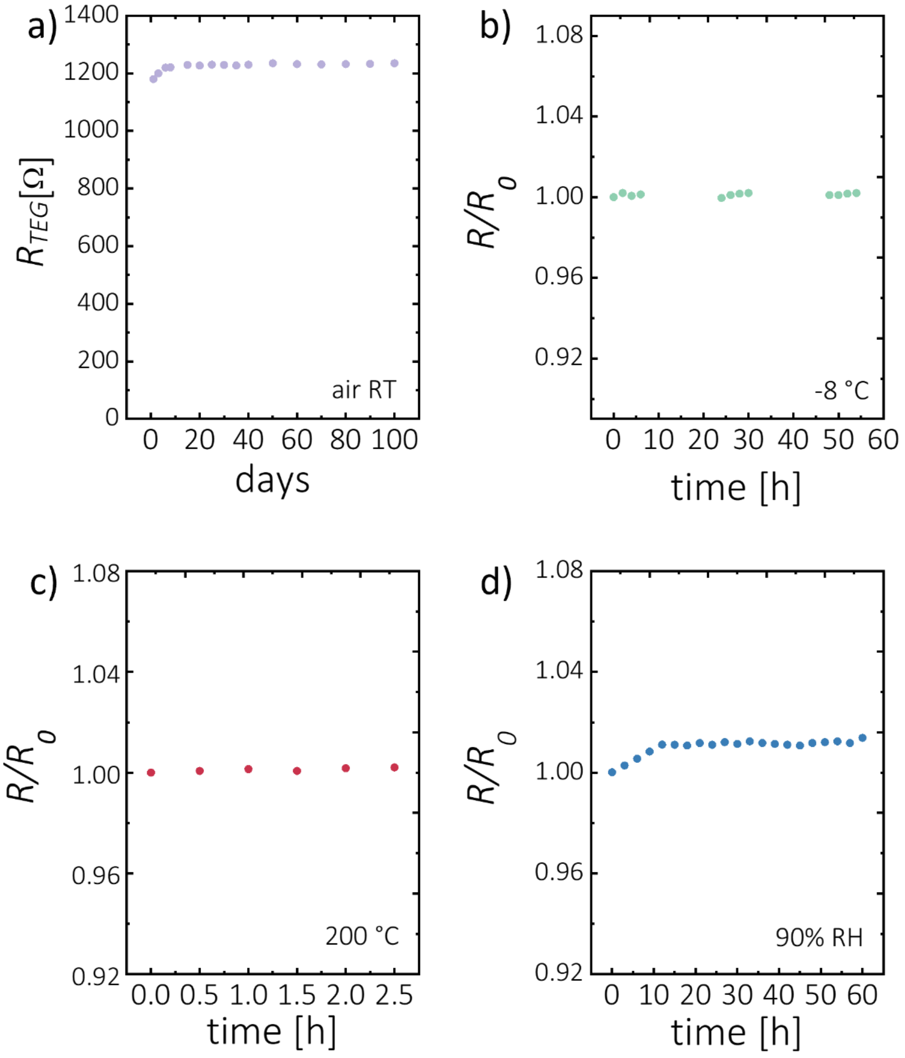

Figure 5.16: a) Internal resistance of the folded 21-thermocouples TEG stored at room temperature, over time. b) Change of internal resistance of the folded 6-thermocouples TEG stored at -8 °C. c) Change of internal resistance of the folded 6-thermocouples TEG stored at 200°C. d) Change of internal resistance of the folded 6-thermocouples TEG stored at 90% relative humidity at RT in a dark environment. Figure from[168] licence CC BY-NC.

This exceptional environmental durability makes this organic TEG particularly promising for use as a power supply in applications, such as wireless sensors used in industrial environments exposed to extreme heat, and remote monitoring devices operating in outdoor environments subject to wide temperature fluctuations and high humidity.

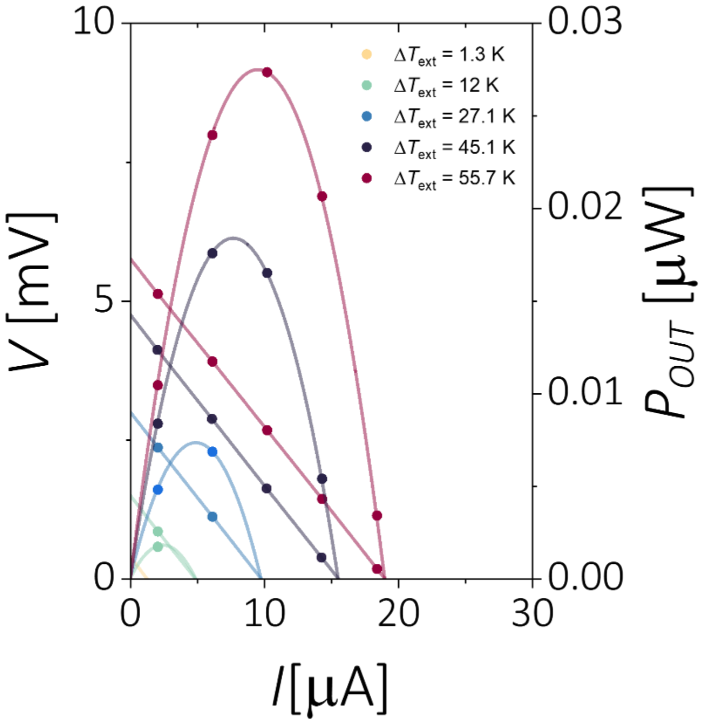

Figure 5.17: *IV* characteristics of the PEDOT:PSS/PBFDO TEG at $\Delta T_{ext} = 1.33$ K to $\Delta T_{ext} = 55.7$ K, and evaluated power output. The fits are parabolic (power) and linear (voltage). Figure from[168] licence CC BY-NC.

5.9 Comparison with the state of the art of organic TEG

A complete comparison with organic TEGs, as described in Chapter 3 requires the analysis of more parameters. Table 5.2 provides an adequate point of comparison between the best organic devices, fabricated by different methods (including non-large area), listing the number of thermocouples, device area, applied ΔT_{ext}, measured power, maximum power density (equation 3.6), maximum normalized power density for ΔT_{ext} = 1K (equation 3.26), operating temperatures, and air stability days.

Table 5.2: State of the art of organic TEG.

Ref	**p-type material**	**n-type material**	**Fabrication Method(s)**	n	A_{TEG} **[cm²]**	ΔT_{ext} **[K]**	$P_{\mathrm{out\ max}}$ **[W]**	$P_{\mathrm{density\ max}}$ **[μW cm⁻²]**	$P_{\mathrm{norm\ density\ max}}$ **[pW cm⁻² K⁻²]**	T **[°C]**	t **[d]**
193	PEDOT:PSS	-	Screen-printing	162	196	85.5	$3.20\cdot10^{-7}$	0.002	0.22	-	-
226	PEDOT:Tos	-	Dispenser printing	30	9	80	$0.4\cdot10^{-7}$	0.004	0.69	-	-
227	PEDOT:PSS	-	Submersion-coating of fibers	8	28.1	65	$1.22\cdot10^{-6}$	0.04	10.28	-	-
228	PEDOT:PSS	-	Thermal evaporation/ spray-coating	24	7.2	17.5	$1.00\cdot10^{-6}$	0.14	453.5	-	-
229	PEDOT:PSS	FBDPPV:TAM	Thermal evaporation/ photolithography/ drop-casting	3	13.2	46.5	$7.70\cdot10^{-8}$	0.01	2.70	-	-
209	TBDOPV-T-518:$FeCl_3$	TBDOPV-T-518:DMBI	Thermal evaporation/ drop-casting	3	21.6	45.1	$4.03\cdot10^{-7}$	0.02	9.17	-	-
32	PEDOT:PSS	PBFDO	Drop-casting	6	29.7	135	$1.95\cdot10^{-6}$	0.07	3.60	-	-
208	PEDOT:PSS	PTEG-1	Laser ablation/ inkjet printing	48	1	25.0	$3.05\cdot10^{-8}$	0.03	48.80	-	-
204	PEDOT:PSS	BBL:PEI	Inkjet printing/ spray-coating	4	0.001	50.0	$3.30\cdot10^{-10}$	0.15	60.83	-	-
This work	PEDOT:PSS	PBFDO	Screen printing/ inkjet printing	21	0.041	61.2	$1.1\cdot10^{-7}$	2.69	718	-8 to 200	>90

The organic folded TEG presented in this work not only provides the best normalized generated power, but also features a high number of thermocouples fabricated with a large-area technique, suggesting potential scalability of the device, exceptional air stability, and durability at extreme temperatures, which has never observed before. While comparisons based on a single parameter can be ambiguous, this multi-parameter analysis emphasizes the remarkable qualities of the reported TEG, especially its impressive performance, scalability, and strong environmental durability, all critical for real-world applications.

5.10 Summary

This work firstly demonstrated the processability of a DMSO-based PBFDO n-type polymer ink, which exhibits excellent performance, through a scalable printing technique. The ink is then incorporated into a 21-leg origami-inspired design, utilizing inkjet and screen-printing methods on an ultrathin, flexible parylene substrate to enhance the power density. The resulting TEG module achieves a record-breaking normalized power density of 0.718 nW cm^{-2} K^{-2}, the highest reported among polymer-based devices.

The importance of this study lies not only in the high performance of the device but also in its exceptional scalability and environmental durability. Impressively, the organic TEG shows no visible degradation over 90 days of shelf life and maintains unprecedented stability across temperatures ranging from -8°C to 200°C, withstanding up to 90% relative humidity. This paves the way for new applications of organic TEGs as power sources in environments with extreme temperatures and humidity. Potential uses include wearable electronics that must endure sweat and temperature variations, wireless sensors in industrial settings, and remote monitoring devices exposed to outdoor temperature fluctuations and high humidity.

Another aspect worth highlighting is the low cost of the device, given the affordability of the inks used and the entirely print-based manufacturing techniques. The cost could be further reduced in the future as the most expensive material, silver, can easily be replaced by either PBFDO or PEDOT:PSS, which would also increase the flexibility of the device.

In conclusion, the integration of high performance, scalable printability, and robust environmental stability marks a significant advancement, demonstrating the potential of organic TEGs to power next-generation sensor networks and IoT devices in challenging real-world conditions that were previously beyond reach for this evolving technology.

6.1 Energy Harvesting-system Based on Vertical Inorganic TEGs

This work presents a low-cost EH system incorporating a new flexible inorganic TEG, fabricated entirely by screen printing, together with an innovative self-powered oscillator.[e] *The TEG is fabricated by stacking seven layers through a simple printing process, without the need for complex additional steps. The fabricated TEG achieved a normalized power output of 6 nWcm*$^{-2}$*K*$^{-2}$*. With this performance, a 5cm x 5cm screen-printed TEG was able to activate the custom step-up circuit of the EH system with a temperature difference of only 7.5K. The custom step-up circuit, based on a Hartley oscillator design, required an input power of only 7.7 µW to begin operation and can amplify an input voltage above 20 mV by a factor of 60. The oscillator was built using low-cost commercial off-the-shelf (COTS) components, making it scalable for widespread use.*

Some of the results of this work are included in a pre-print article[194e] *and in the doctoral thesis of Dr. Matias Joglar.*[195]

Preliminary studies on these devices have been published in the doctoral thesis of Dr. Andres Georg Rösch.[196]

6.2 Introduction

In recent years, advancements in low-power electronics have significantly reduced the energy consumption of components, bringing their requirements down to the µW range.[28]

In the previous two Chapters, we explained how organic TEGs are gradually improving, with the development of new structures and materials, moving towards a more application-oriented approach. Despite this, the power provided by these devices is still too low to power a commercially available DC-DC converter, which requires a higher and more stable supply voltage. For this reason, it is also important to develop custom circuits that minimize input power and voltage. At this stage of the research, we can develop electronic interfaces capable of being powered by printed inorganic TEGs.

---

[e] collaboration with M.Sc. Matias Joglar supervised by Dr. Claudia Delgado Simao (Eurecat Centre Tecnologic). Partner of the Horates project.

Inorganic TEGs, as introduced in previous Chapters, offer higher performance and represent a more mature technology with greater reliability. However, traditional inorganic TEGs are hindered by high production costs, complex manufacturing techniques, and difficulties with integration and customization.[197]

This work presents a cost-effective, small-area application-oriented energy-harvesting system, powered by waste heat. A fully printed inorganic TEG with a similar architecture to the TEG described in Chapter 4 is fabricated, characterized, and validated, showing a great $P_{\text{norm density}}$ of 6 nWcm^{-2}K^{-2}. This TEG is capable of adapting to non-uniform surfaces, maximizing the harnessing of waste heat, and powering a novel ultra-low-voltage self-powered oscillator made entirely with COTS components. Thanks to the normalized power density of the device and the low V_{in} and P_{in} required to initiate oscillation of the custom circuit proposed, this low-cost EH system can start with a very small ΔT_{ext} of 7.5 K, suitable for the IoT network scenario.[92]

6.3 TEG layout

It was decided to replicate the entirely screen-printed structure presented in Chapter 4 [151] with the addition of two layers of carbon paste (Dycotec DM-CAP-4701S) with the same layout as the bottom contact and top contact silver layers to reduce the contact resistance between the silver and the thermoelectric legs.[151] This layer acts as a diffusion barrier, preventing corrosive chemical reactions between the silver and the thermoelectric materials during sintering. The structure has been enlarged, and the exact dimensions are shown in Figure 6.1. Each TEG fabricated measured 5 cm x 5 cm and consisted of 32 thermocouples made from n-type and p-type inorganic materials. Anodized aluminum foil (65 µm thick) supplied by *Steinert GmbH*, was used as the substrate to enhance the effective temperature gradient along the thermoelectric legs and maximize the power output, as the aluminum has a very high thermal conductivity (further information in section 3.5). The metallic substrate is compatible with all sintering processes, and thanks to the anodized passivation layer, which is 4.4-5.8 µm thick, prevents device short circuits.

The TEGs were fabricated by stacking seven screen-printed layers. Figure 6.1f illustrates the deposition of the final two layers. First, a commercially available silver bottom contact (*LOCTITE* ECI 1010 E&C) was screen-printed (2 layers), followed by a carbon paste layer using the same screen and layout (Figure 6.1a). Next, the insulator layer with square cavities to hold the thermoelectric legs was printed (Figure 6.1b). Then, the p-type and n-type thermoelectric legs were screen-printed with different layouts to alternately fill the cavities (Figure 6.1c-d). The print of the n-type and the p-type layout was repeated 8 times. Lastly, a layer of carbon paste and a silver top contact (2 layers) were printed sequentially, using the same screen and layout, to reduce the contact resistance (Figure 6.1e).

The devices were annealed for 5 minutes at 400 °C in a nitrogen-filled glovebox to sinter the inorganic materials. No additional fabrication steps were necessary.

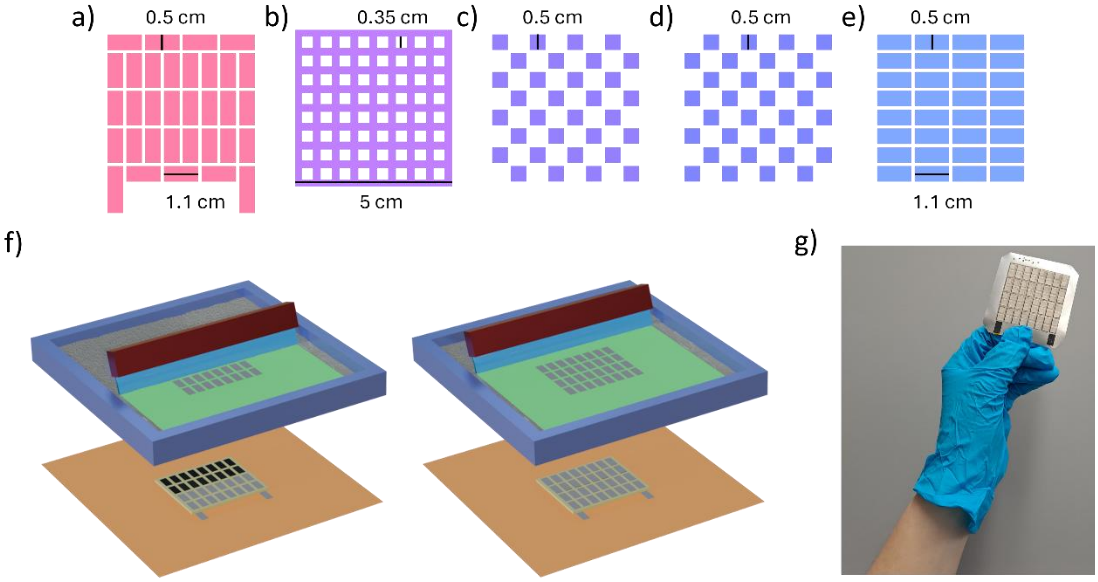

Figure 6.1: Layouts of the screen to make the TEG: a) Layout of the bottom contact silver and carbon layers. b) Layout of the insulator layer. c) Layout of the p-type legs layer. d) Layout of the n-type legs layer. e) Layout of the top contact silver and carbon layers. f) Sketch of the printing step of the silver top contact. g) Picture of the inorganic fully screen-printed TEG.

The geometric fill factor *FF* of the TEG design described by equation 3.17 can be adjusted for different application scenarios, and it depends on the resolution of the printing technique and the printer used. We aimed to keep the *FF* constant, even though a different printer was used compared to the one that fabricated the TEG presented in Chapter 4, without an automatic alignment. In this case, a semi-automatic screen-printing machine

(*RokuPrint* SD 05) was employed, and an *FF* of 0.3 was achieved. Figure 6.1f shows a photograph of a fully screen-printed TEG produced using this method.

To get an estimate of the total thickness of the device, a digital micrometer was used. Although it is a rough measurement, the thickness (without the substrate) was found to be 175 µm.

The n-type ($Bi_2Te_{2.7}Se_{0.3}$-based) and p-type ($Bi_{0.5}Sb_{1.5}Te_3$-based) inorganic pastes were prepared using the same one-pot in-house methods described in the article (Figure 6.2).[198]

Figure 6.2: Bismuth telluride ink, produced with a ball milling during the production. © 2022 Leonard Franke, reproduced with permission.

6.4 Characterization of the TEGs

Two different TEGs *dev A* and *dev B* were printed using the previously described process and characterized. The internal device resistances were measured as $R_{\mathrm{TEG}} = 5.5\ \Omega$ for *dev A* and $R_{\mathrm{TEG}} = 5.3\ \Omega$ for *dev B*, indicating a good reproducibility of the manufacturing process.

Both devices, each containing 32 thermocouples, were measured using the custom-built presented in Chapter 5. During the characterization, the devices were clamped between the two copper blocks with thermal paste applied to enhance thermal contact. The current-voltage *IV* curves were measured using a *Keithley* 2601B (SMU) after a steady temperature difference ΔT_{ext} was established. The P_{out} was calculated as the product of I and V. Small temperature differences of under 20 K were chosen to simulate realistic conditions for an IoT application.

Figure 6.3a-b illustrate the ideal behavior of the TEG. The V shows a linear relationship with I, and the P_{out} of the fully printed TEGs exhibits ideal performance, achieving a maximum value when the load resistance is matched to the internal resistance, as described by equation 3.6.

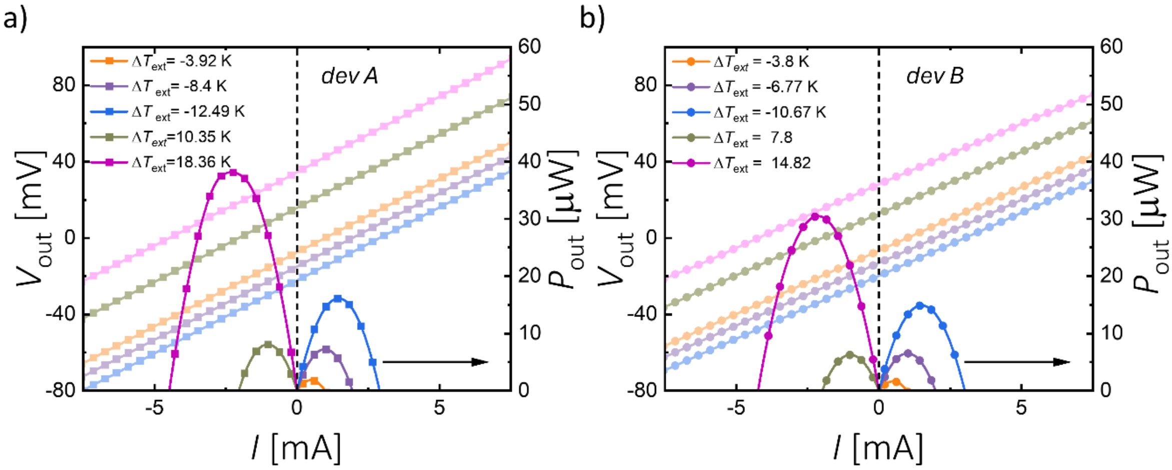

Figure 6.3: *IV* characteristic (left axis) and calculated power output (right axis) of a) *dev A* at ΔT_{ext} = -3.92 K to ΔT_{ext} = 18.36 K and b) *dev B* at ΔT_{ext} = -3.8 K to ΔT_{ext} = 14.82 K.

The $P_{\mathrm{out\,max}}$ for *dev A* and *dev B* as a function of the absolute ΔT_{ext} followed the same ideal parabolic trend, further highlighting the excellent reproducibility of the fully printed TEGs produced by the fabrication method proposed in this thesis, even for inorganic materials (Figure 6.4a).

In IoT applications the area occupied by the devices and the ΔT_{ext} are key factors. [199] In addition, conformability and durability are also required but are often not demonstrated in articles using inorganic materials, as they are typically brittle. The TEG presented in this work demonstrates remarkable flexibility, with resistance remaining unchanged even when the TEG was rolled into a cylinder with a bending radius of 2.75 cm (Figure 6.5).

Furthermore, the *IV* characteristics of *dev B* were repeated 1 month after the printing process, and the $P_{\mathrm{out\,max}}$ followed the same parabola with an R-square (COD) of 0.99297, showing encouraging stability over time (Figure 6.4b).

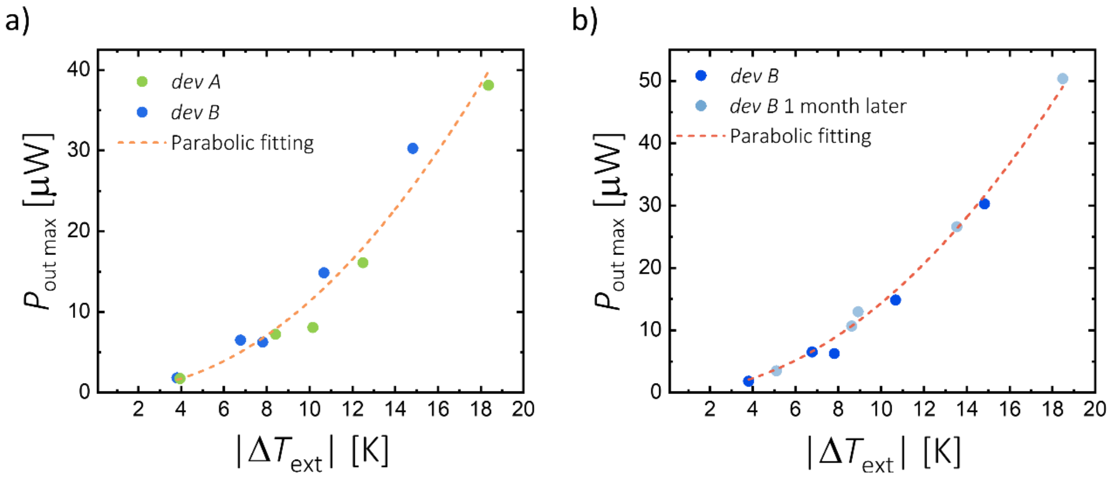

Figure 6.4: a) Maximum power output as a function of the absolute value of the ΔT_{ext} of *dev A* (green dots) and *dev B* (blue dots). b) Maximum power output as a function of the absolute value of the ΔT_{ext} of *dev B* (blue dots) and *dev B* one month later (light blue dots). The fits are parabolic.

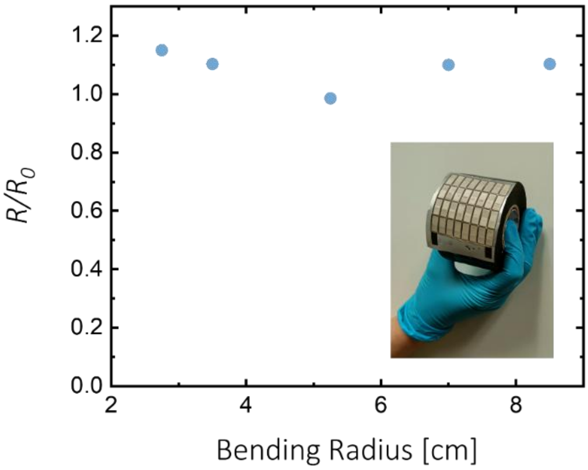

Figure 6.5: Resistance change ratio of the inorganic fully printed TEG as a function of the bending radius.

6.5 Finite element simulations

The behavior of the device was simulated using COMSOL Multiphysics to predict its performance and give an idea of the device dimension and the applied temperature difference required to power the startup circuit, as well as the behavioral differences from the organic device described in Chapter 4, particularly due to the use of a thermally conductive substrate and materials with higher TE properties.[f] The performance of the devices, in this case, was only estimated, as it was not possible to measure the thickness of the individual printed layers, and the thermoelectric properties were measured on another batch of inks (made from the same recipe). Furthermore, the carbon paste layers were not included in the model. The values used for these qualitative simulations are summarized in Table 6.1 and Table 6.2. All simulations were carried out using the heat transfer in solids and electric currents interfaces from the thermoelectric Multiphysics package, as described in Chapter 4.

Table 6.1: Thicknesses of the screen-printed layers used in the simulation.

Thicknesses	**[µm]**
t_{sub}	65
t_{leg}	70
t_{silver}	50
t_{par}	1

---

[f] performed by M.Sc.Federico Ferrari supervised by prof. Dr. Jan Anton Koster (Groningen university). Partner of the Horates project.

Table 6.2: Material properties of the materials used in the simulation.

Materials Properties	
S_{p}	128 μV/K
S_{n}	-160 μV/K
S_{silver}	1.5 μV/K[92]
σ_{p}	660 S/cm
σ_{n}	250 S/cm
σ_{silver}	6×10^5 S/cm [92]
k_{p}	0.6 W/mK[198]
k_{n}	0.45 W/mK[198]
k_{silver}	400 W/mK [92]
k_{ins}	0.3 W/mK [164]
k_{sub}	400 W/mK
k_{par}	0.09 W/mK[165]

All simulations were performed with a ΔT_{ext} of 10 degrees, and focused on simulating the V_{oc}, to estimate the condition to provide the minimum V_{in} at the startup stage. The simulated device has the same dimensions as the printed devices (Figure 6.1a). The simulations also included a layer of parylene, which was present during the measurements, to electrically insulate the device (t_{par}).

The parameters were varied one by one to try to match the measured V_{oc} for a $\Delta T_{\mathrm{ext}} = 10$ of the 5×5 cm TEG, i.e. $V_{\mathrm{oc}} = 17.5$ μV/K. The results are shown in Figure 6.6, Figure 6.7, and Figure 6.8.

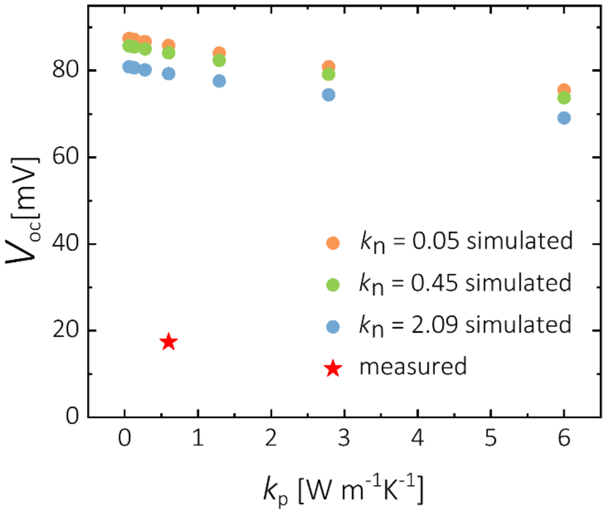

Figure 6.6: Simulated open circuit voltage as a function of the thermal conductivities of the TE materials. All the values of the other parameters used in these simulations are described in Tables 6.1 and 6.2. The red star is the measured V_{oc} with the assumed value of k_p listed in the table.

One of the most critical measurements is certainly the k of the materials, so the first step was to run a simulation varying the values of k_p and k_n. As can be seen from Figure 6.6, the V_{oc} shows limited change with the variation of the k of the materials. This is because, unlike the substrate used in Chapter 4, the aluminum substrate has a high k, making ΔT and ΔT_{ext} similar, as the thermal resistance of the device is the dominant factor. In the second simulation, the S of the p-type and n-type TE materials were varied. As can be observed from Figure 6.7a, these variations resulted in a more significant change in V_{oc}. Therefore, an error in measuring the Seebeck coefficient can significantly affect the estimation of the V_{oc} provided by the device. Figure 6.7b shows that the measurement of the leg thickness is also sensitive; even a small error in measuring l_{teg} can cause a large error in V_{oc}, at least up to l = 250 µm. Beyond this point, the thermal resistance of the device becomes dominant, and V_{oc} becomes almost independent of l_{teg}. Remember that in any case, as l_{teg} increases, so does R_{teg}, which is inversely proportional to maximum power.

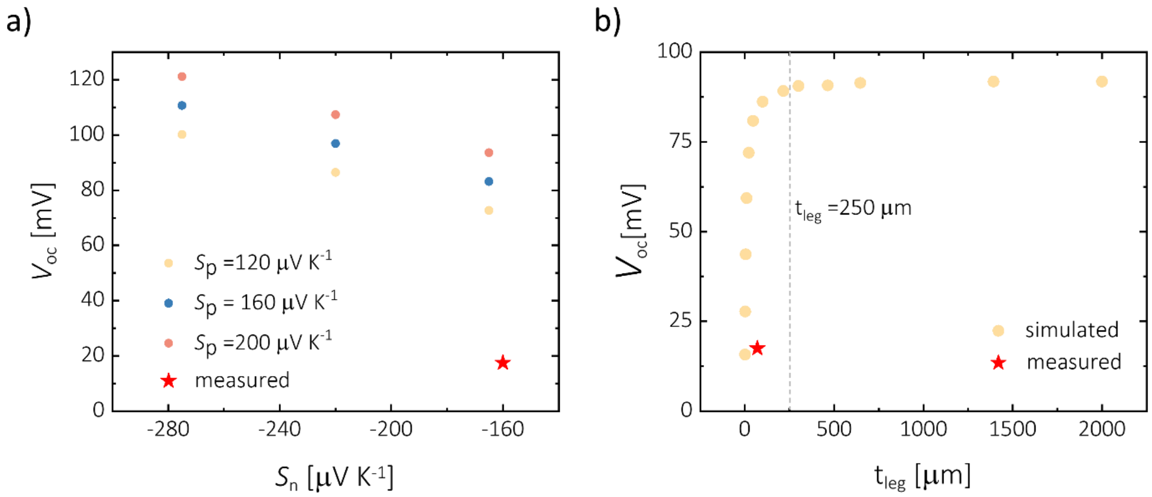

Figure 6.7: a) Simulated open circuit voltage as a function of the Seebeck coefficients of the TE materials. b) Simulated open circuit voltage as a function of the leg thickness. All the values of the other parameters used in these simulations are described in Table 6.1 and Table 6.2. The red star is the measured V_{oc} with the assumed k_p and the k_{ins} listed in the table.

A simulation was also conducted considering the geometric parameters of the device to observe how the *FF* influences the V_{oc}. The dimensions of the rectangular p-leg and n-leg were varied simultaneously changing the value of the *FF*. As can be seen in Figure 6.8, the V_{oc} does not change significantly. However, it is important to note that, when *FF* increases the R_{teg} decreases, as the legs become wider, leading to an increase in power since the V_{oc} remains almost constant.

Finally, a simulation was performed varying the thickness of the parylene layer t_{par} required for electrical insulation and at the same time the thickness of the legs. Note that in this case the parylene is only placed on top and not deposited on the device. As expected, the smaller the leg thickness, the greater the influence of the parylene thickness. In our hypothesis, with a leg thickness of 70 µm, if the thickness of the parylene layer varies from 1 µm to 5 µm, V_{oc} changes by 14%, but it is still far from the measured value (17.5 mV). It should also be noted that these simulations did not take into account the anodized aluminum layer, which acts as an insulating layer and has a non-negligible thickness of 5 µm, certainly lowering the simulated open circuit voltage.

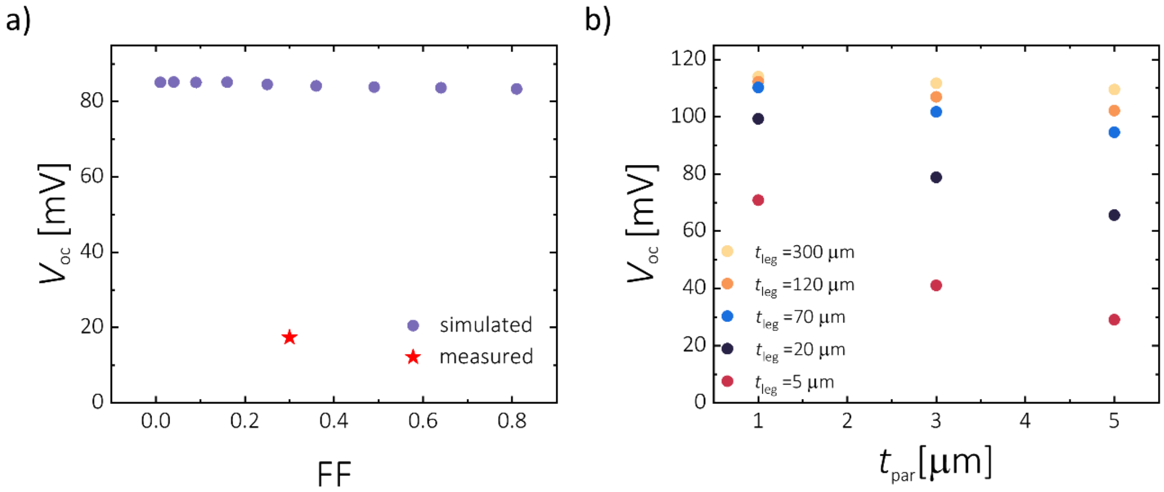

Figure 6.8: a) Simulated open circuit voltage as a function of the Fill factor of the device. The red star is the measured Voc with the assumed dimensions described in Figure 6.1a. b) Simulated open circuit voltage as a function of the leg thickness from 5µm to 300µm and the parylene thickness from 1µm to 5 µm. All the values of the other parameters used in these simulations are described in Table 6.1 and Table 6.2.

These qualitative simulations give higher values than the measured performance of the devices. This discrepancy is likely due to variations in the thermoelectric properties of homemade inks produced in different batches, a challenge faced by both organic and inorganic materials. Significant progress has been made in the field of organic materials, particularly with the introduction of PBFDO, which, when synthesized correctly, appears to maintain consistent performance across batches, and the improvement of PEDOT inks, which have long been commercially available. However, the thermoelectric properties of inorganic materials remain superior, with devices offering higher normalized power densities in the µW range compared to the nW range of organic devices. Nevertheless, the use of PBFDO and the development of the device presented in Chapter 5 is a step forward in bridging the gap between organic and inorganic devices.

Given the discrepancy between the simulations and the measurements, it was not possible to use these simulations to estimate the V_{oc} and, consequently, to estimate the condition to provide the minimum V_{in} necessary to initiate the startup stage. Therefore, it was decided to experimentally measure the ΔT_{ext} required to activate the start-up circuit, using the 5 x 5 cm device with a *FF* of 0.3 presented in the previous sections, and varying the ΔT_{ext} until the V_{oc} was sufficient to trigger the start-up stage (Figure 6.9).

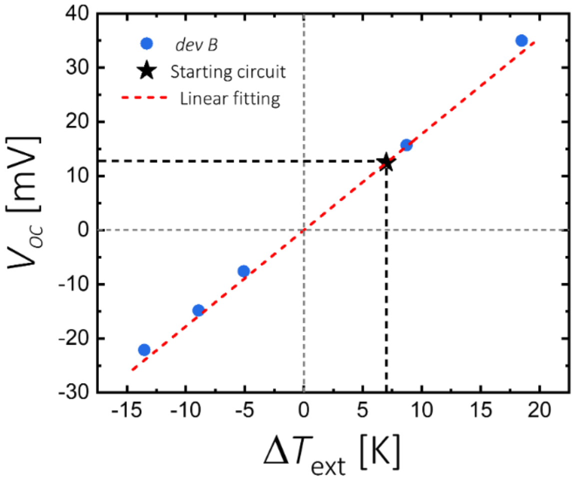

Figure 6.9: Measured open circuit voltage of the *dev B* as a function of ΔT_{ext} (blue dots) and the linear fitting (red dashed line). The black start shows the V_{oc} necessary to start the start-up stage. Also reproduced in the thesis (licence CC BY NC SA).[195]

6.6 Customized step-up stage

The successful integration of the printed and scalable TEG presented in this work into a real-world application requires the implementation of an electronic booster circuit. DC-DC converters are the most commonly used booster circuit. They can be classified into two groups. The first group works with low voltage (around 20 mV),[200] low resistance (<10 Ω), and has a low efficiency. The second group operates with higher voltages (>100mV), a wider range of input resistances, and generally has higher efficiencies due to the application of the maximum power point tracking (MPPT) method.[201,202]

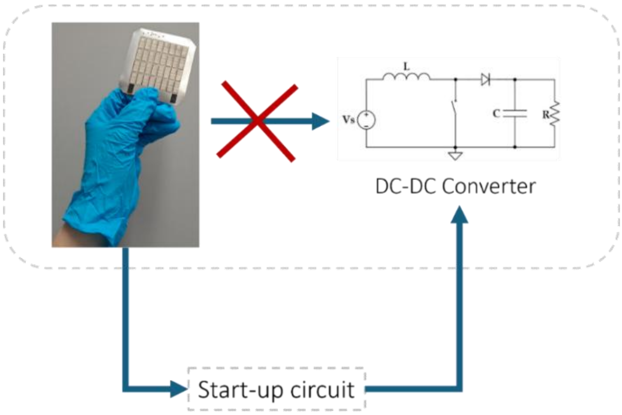

Figure 6.10: Diagram showing the impossibility of powering a DC-DC converter directly with the TEG without the use of a start-up circuit.

If we consider the use of printed TEGs, especially in the case of organic, the first group cannot be used due to the high internal resistance of the devices, which could provide sufficient values of V_{in}. Moreover, the use of the second group is also not possible because the generators cannot provide the necessary power at low or moderate temperatures (Figure 6.10). In this work, we concentrated on developing a start-up circuit designed to operate at very low voltages and to provide high voltage amplification to reach a voltage level suitable for starting the main DC-DC converter.

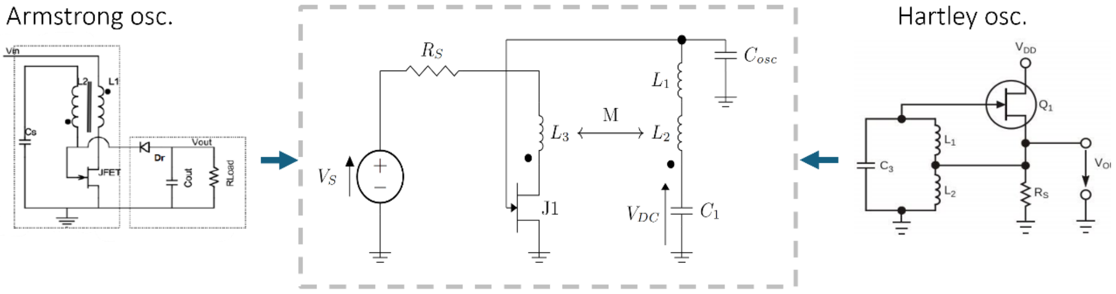

Figure 6.11: Start-up circuit schematic (within the dashed grey box). This circuit is a combination of the Armstrong oscillator and Hartley oscillator topologies. Also reproduced in the thesis (licence CC BY NC SA).[195]

Typically, the start-up circuits are self-power oscillators, that enhance the V_{in} thanks to positive feedback. These start-up circuits amplify the input signal by generating oscillations, usually using resonant circuits. By employing active components naturally on, as the JFET, is possible to start the oscillator with very low V_{in}.[203]

Most of the oscillator start-up stages presented in the literature use Hartley[203] and Armstrong oscillators.[203–207] In this work, we introduced a novel typology, which is a mix between these two types. Figure 6.11 shows the proposed circuit. The circuit consists of two inductors in series, which amplify the voltage by a factor of L_1/L_2, and at the same time are part of the resonance tank (Hartley topology). Additionally, the design incorporates coupled inductors within the feedback loop, characteristic of an Armstrong oscillator. This combination results in two stages of amplification. Thanks to the mutually coupled inductors, the start-up voltage of the primary is reduced because the voltage is amplified in the secondary by a factor of N (the turn ratio of inductors L_3 and L_2). The second amplification, which is necessary to achieve a better conversion ratio (CR) i.e., the difference between the DC output voltage and the DC input voltage comes from the presence of L_1. When L_2 discharges (during resonance), the voltage on L_1 will be equal to $V_{L1} = V_{L2} (L_1/L_2)$.

The start-up method of the circuit proposed is the same as that of the classical Armstrong oscillator,[206,208] and can be summarized as follows:

1. The JFET J_1 is naturally on with V_{GS}=0, when the TEG is connected the V_{L3} from the maximum value starts to decrease, and the current start I_1 starts to increase. At the same time, the positive voltage is transferred to the secondary and the V_{GS} becomes positive. This activates the gate-source diode, which causes a current I_2 to flow, charging the capacitor C_1 negatively.

2. After a time t_1, I_1 reaches its maximum value, remaining stable. At this point, V_1 will be close to zero, and the voltage on the secondary will also approach zero. The V_{GS} will then be negative, and the JFET channel approaches pinch-off, which causes a reduction in I_1 and accelerates the complete shutdown of the JFET.

3. When the JFET is off, the secondary sees an LC circuit, with the series of $L_1 + L_2 = L_{eq}$ and C_{osc} (C_1 is specifically chosen to be much larger than C_{osc} and acts as a short circuit at the resonance frequency). The LC circuit starts oscillating until the V_{GS} is high enough to turn the JFET back on and restart phase 1.

For this to occur, the V_{DS} of the JFET must be much lower than the V_p, and the JFET must be operating in the linear ohmic region. Figure 6.12 shows the small-signal circuit of architecture proposed (assuming ideal components) necessary to derive the minimum value of V_{in} required to start the oscillation.

As is possible to see, since the JFET is operating in the ohmic region it can be represented by a current source $g_m V_{gs}$ and a resistance R_{DSon} between drain and source.

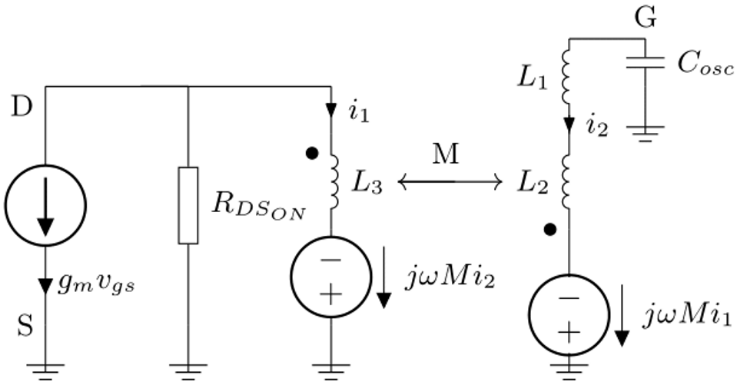

Figure 6.12: Small-signal circuit at the start-up. Also reproduced in the thesis (licence CC BY NC SA).[195]

For the complete circuit solution, please refer to the reference.[194] For the Barkhausen criterion the possible oscillating steady-state frequency is obtained by equalizing the real part of the poles of the system to zero (pure imaginary poles):[209]

$$w_0 = \frac{1}{\sqrt{L_{eq}C_{osc}}} \tag{6.1}$$

However, to trigger the oscillation the poles should have a real part greater than zero (oscillation with increasing amplitude in frequency) this condition allows the calculation of the minimum input voltage V_{in} required to initiate oscillation. Considering $V_{\text{DS}} \cong V_{\text{in}}$:

$$V_{in} > \frac{C\sqrt{L_3L_2}}{(L_1+L_2)}|V_p| \tag{6.2}$$

Where C is the coupling factor $C = \text{M}/(\text{L}_2\text{L}_3)^{1/2}$, and V_{p} is the pinch-off voltage of the JFET.

Unfortunately, when considering non-ideal components, we have to consider the resistances to the inductors and the source, and the equation that describes the start-up becomes more complex. Considering that when the system starts to oscillate L_3 can be simplified with its small r_3, and $r_3 << R_{\text{S}}$, R_{Dson} the non-ideal component circuit can be slightly simplified, and the V_{DS} can be described as a function of V_{in} as follows:

$$V_{DS} = V_{in}\frac{R_{DSon}}{R_{DSon}+R_S} \tag{6.3}$$

By simplifying $C = 1$, and defining r_1 as the resistance series of L_1 and L_2, the minimum V_{in} can be expressed:

$$V_{in} > \frac{R_{DSon}+R_S}{R_{DSon}}\,\frac{R_{DSon}+r_1(\frac{1}{N^2}+C_{osc}r_1(R_{DSon}+R_S)L_2+\frac{C_{osc}L_{eq}(R_{DSon}+R_S)^2N^2}{{L_2}^2})}{\frac{r_1}{N}+R_{DSon}L_{eq}N/L_2}\,|V_p| \tag{6.4}$$

Note that also the oscillation frequency is no longer exactly the same as that described by equation 6.1:

$$ {w_0}^2 = \frac{L_3(R_S+R_{DSon})-Mg_mR_{DSon}R_S}{C_{osc}({L_3}^2r_1+L_{eq}L_3(R_S+R_{DSon})-M^2R_S} \tag{6.5} $$

The components of the circuit have been selected to minimize the start-up voltage, maintain a not-too-high oscillation frequency, and achieve a good conversion ratio.

First of all, since the TEG used in this project has a low resistance, a JFET (6 JFETs in parallel) with a high I_{dss} (saturation current at zero gate-source volgate) was chosen to electrically match the source, knowing that the $R_{\mathrm{DSon}} = |V_{\mathrm{p}}|/(2I_{\mathrm{dss}})$.

The choice of V_{p} is very delicate, as to reduce the minimum voltage needed to start the circuit, it should be as low as possible (see equations 6.4 and 6.2). However, at the same time, this reduces the time during which the JFET is on, decreasing the output voltage and consequently lowering the *CR*. The capacitance C_{osc} in the real circuit is the C_{iss} capacitance ($C_{\mathrm{gd}} + C_{\mathrm{gs}}$, the input capacitance) of the JFET. According to equation 6.4, it should be chosen as low as possible. However, if we choose a C_{osc} that is too small, the oscillation frequency (equation 6.5) would become too high, increasing the parasitic resistances of the inductors. Looking at equation 6.3, we can see that the ratio of L_2/L_{eq} should be as small as possible, and a high value of N improves both the minimum start-up voltage and the *CR*. Therefore, a small L_3 was chosen with the maximum available N, to maintain L_2 small. Finally, the inductor L_1 was selected using equation 6.4 (two inductors were used in series to increase the value of L while maintaining a high self-resonance frequency). The value of C_1 has been chosen high enough to not influence the resonance frequency of the circuit. Table 6.3 summarizes the components used in the circuit.

Table 6.3 List of components used in the start-up circuit.

Component	**Reference name**
JFET	2SK3320-BL (Toshiba) ×6
L1	17335C (Murata) ×2
L2	LPR4012-202LMR_ (Coilcraft)
L3	LPR4012-202LMR_ (Coilcraft)
C1	UKL1A221MPD (Nichicon)

6.6.1 Step-up circuit characterization

The start-up circuit was initially tested using the 2604B *Keithley* Sourcemeter as a source (negligible R_s) to calculate the minimum start-up voltage and the *CR*. The V_{out} was measured with a 34410A *Agilent* multimeter (R_L=10 MΩ). The input voltage V_{in} was increased in small steps to find the minimum V_{in}. The circuit started oscillating at V_{in} = 9.92 mV. In this case, the *CR* was found to be 30. By increasing V_{in} up to 100 mV in steps of 10 mV, the maximum *CR* was then calculated. For input voltages higher than 20 mV, the circuit can amplify by a factor of 60.

6.7 System integration

After validation with the ideal source voltage, the flexible TEG presented was used as a voltage source to verify the performance of the two elements in the cascade as shown in Figure 6.13. The TEG was placed in the custom-built setup and connected to the start-up circuit. The ΔT_{ext} was then increased until the circuit began to oscillate, generating a V_{out}. The oscillation started when the ΔT_{ext} reached the value of 7.5 K (highlighted in Figure 6.9).

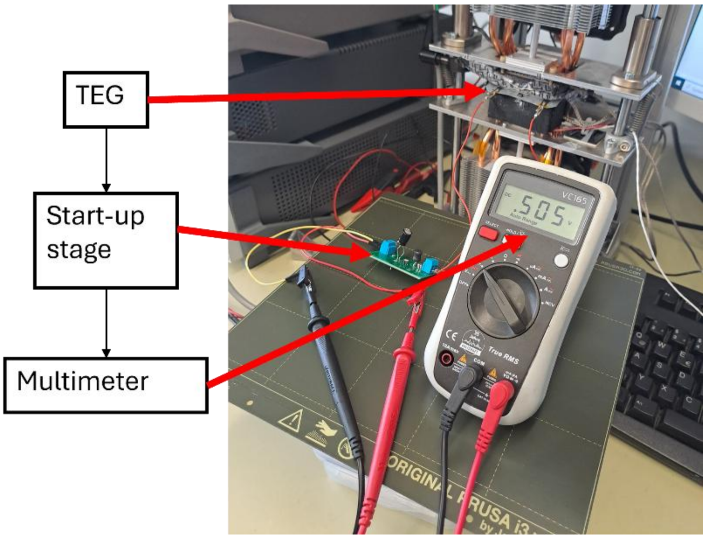

Figure 6.13: Start-up stage powered by the flexible TEG. Also reproduced in the thesis (licence CC BY NC SA).[195]

Because of the inefficiency of the oscillator circuit, the oscillator is not able to directly power an electronic board, but it should be used as a start-up circuit to initiate a DC-DC converter. The potential of the system could be demonstrated by designing a custom DC-DC that can be powered by the oscillator.

6.8 Summary

In this work, a very low-cost and versatile EH system has been presented. The system consists of a scalable fully-printed flexible TEG and an ultra-low-voltage self-oscillator start-up circuit, showing a good *CR*, made entirely with COTS discrete components.

The TEG was fabricated using the same manufacturing method presented in Chapter 4, but with inorganic materials to provide higher power output. Both long-term stability and reproducibility were tested and validated. Additionally, since the design is versatile it can be adapted based on the required power needs.

Afterward, the start-up circuit was designed and analyzed. It was initially tested with an ideal voltage generator, and then directly with the device. A minimum $V_{\mathrm{in}} = 9.92$ mV was necessary to start the oscillation, and the start-up stage exhibited a maximum *CR* of 60.

The TEG was capable of starting the start-up circuit with a ΔT of only 7.5 K, demonstrating how this system can be suitable for low-power applications.

At this stage of the research, we could not use organic TEG to power the electronic interfaces, but since the start-up circuit was designed with COTS discrete components, it can be adapted at low cost in the near future for use with organic TEGs.

As discussed in Chapter 5 the organic TEGs have significantly increased power density, achieving high V_{oc} values, but still exhibit excessively high resistances, to be used with the start-up circuit proposed. One possibility would be to replace the JFET in the oscillator to increase the input resistance and electrically match the TEG (inevitably increasing the V_{in}).

7. Conclusion and Outlook

Although conventional TEGs based on rigid bulk materials dominate the energy harvesting market due to their high performance, they are limited by inherent rigidity, complex fabrication processes, and high production costs. Therefore, their application is often limited to rigid and stationary surfaces. Printed TEGs are a complementary technology to traditional bulk materials-based TEG, and are designed to be flexible, lightweight, and cost-effective, enabling their use in portable and wearable devices. These unique advantages make printed TEGs a promising solution for energy harvesting in applications such as wearable electronics, remote sensors, and IoT devices. Among the various materials used in printed TEGs, inorganic materials achieve a high thermoelectric FoM zT of up to 1.2,[77] approaching the values of bulk materials and enabling high-performance devices. However, their flexibility remains limited due to brittleness, and the inorganic materials themselves are rare. In contrast, organic materials provide greater flexibility and are more eco-friendly because of their abundance, although they generally exhibit thermoelectric performance showing zT nearly an order of magnitude lower than inorganics (Chapter 2). Nevertheless, significant progress has been made in the scalability and stability of organic solutions, such as graphene[68] and PBFDO,[32] as well as the widely used and commercially available PEDOT:PSS, materials employed in this thesis. This opens the door to the optimization and large-scale fabrication of devices beyond small proof-of-concept prototypes (Chapter 3).

In this work, as a significant contribution to the field, high-throughput additive fabrication techniques are employed to demonstrate the feasible large-scale production of organic devices taking a step toward practical applications. By streamlining the process to the essential steps of printing and annealing, the transition from lab-scale validation to a manufacturing prototype was achieved. This pilot process, conducted at mid-volume using semi-automated methods, represents a critical step toward scalable production, demonstrating for the first time in a large-area TE device the use of two promising inks, free-additive graphene (Chapter 4) and a stable, highly conductive n-type material, PBFDO (Chapter 5). Two different device architectures were successfully developed with performance in line with finite element simulations, with devices up to 800 thermocouples (Chapter 4) and record performance for organic TEGs, along with unprecedented stability in harsh environments (Chapter 5).

Chapter 4 presents a fabrication technique for robust, large-area, fully-printed vertical organic TEGs, in which the layers are simply stacked on top of each other. The method is simple, cost-effective, and scalable to meter-square dimensions, marking a first for organic TEGs. These devices show consistent performance aligned with material simulations. The TEG design was validated using a common p-type material, PEDOT:PSS, and conductive silver ink, creating TEGs with either 4 or 8 thermocouples (0.5×1 cm^2 or 1×1 cm^2). Afterward, a TEG was developed using additive-free graphene as the p-type material, achieving a power normalized density of 1.7×10^{-5} $\mu W\ cm^{-2}\ K^{-2}$. Power density could be further enhanced with design modifications, such as using a thinner, thermally conductive substrate (as shown in Chapter 6). These TEGs feature short-circuited n-type legs made from silver ink due to the absence of stable organic n-type inks. Introducing a comparable organic n-type ink (as introduced in Chapter 5) could potentially double the power output. The fabrication process is compatible with any screen-printable ink, including inorganic materials with superior thermoelectric properties (Chapter 6). Additionally, the ability to fabricate TEGs with up to 800 thermocouples has been demonstrated, paving the way to a m^2 scaling.

Chapter 5 demonstrates the processability of a DMSO-based PBFDO n-type polymer ink with excellent performance through a scalable printing technique. The ink is used in a 21-leg origami-inspired TEG design, utilizing inkjet and screen printing on an ultrathin, flexible parylene substrate to enhance power density. This TEG module achieves a record-breaking normalized power density of 0.718 $nW\ cm^{-2}\ K^{-2}$, the highest reported for organic devices. Notably, the organic TEG shows no visible degradation over 90 days and maintains stability across temperatures from -8°C to 200°C, withstanding up to 90% relative humidity. This opens up new applications for organic TEGs in real-environment conditions, such as wearable electronics, wireless sensors in industrial settings, and remote monitoring devices exposed to outdoor temperature fluctuations.

Unfortunately, despite the progress made, printed organic TEGs cannot yet be used in real applications. This is because, although progress has been made, these devices are still unable to power a COST low-power electronic interface, which is the only sensible option for the niche market of TEGs, capable of boosting voltage and functioning as a battery. For this reason, we still need to make progress in material development and work on increasing the zT of organic materials. At the same time, it is crucial to develop a COST low-power electronic interface capable of minimizing the required input voltage, which can currently only be achieved with inorganic materials.

Chapter 6 presents a low-cost and versatile EH system, consisting of a scalable fully-printed flexible TEG and an ultra-low-voltage self-oscillator start-up circuit, both made entirely with COST components. The TEGs were fabricated using the method described in Chapter 4, using inorganic materials for higher performance. Long-term stability and reproducibility were tested and validated. At the same time, the start-up circuit was designed and analyzed. It was tested first with an ideal voltage generator and later with the TEG, a minimum input voltage of 9.92 mV was required to initiate oscillation, with a maximum conversion ratio of 60. Remarkably, the TEG could start the circuit with a temperature difference of just 7.5 K, demonstrating the suitability of the system for low-power applications.

In conclusion, this thesis represents a first step toward the lab-to-fab transition for organic TEGs, setting the stage for the potential evolution of printed electronics toward large-scale application.

In an ideal scenario, a fully organic device could offer 100% recyclability, a low thermal budget, and a reduced environmental footprint in line with modern sustainability standards. A possible evolution of the architectures presented in Chapters 4 and 5 could include the use of all organic materials, such as PBFDO and PEDOT (or free-additive graphene). However, current performance remains limited. Nonetheless, the reliability of the fabrication process and the performance predictions from finite element simulations offer promising insights into what could be possible with advanced materials and optimized substrates. To facilitate the practical adoption of these materials, it is crucial to demonstrate their large-scale processability and minimize batch-to-batch variability an ongoing challenge in printable electronics.[210]

As a next step, developing a screen-printable PBFDO ink could enable thicker printed films, which would reduce the total resistance of the organic folded TEG presented in Chapter 5 and expand the design possibilities for new architectures.

Furthermore, a comprehensive characterization of thin printed films, including standardized measurements of in-plane and out-of-plane TE properties, is needed to refine performance predictions and improve the device design, together with a better understanding of the TE transport mechanism of solution-processable (in)organic materials.

Finally, to take a further step toward potential commercialization, it would be necessary to incorporate more rigorous device testing, such as Highly Accelerated Life Testing, which would extend the basic testing performed in this thesis.

List of Figures

List of Tables

Abbreviations

EH	Energy Harvesting
TEG	Thermoelectric Generator
TE	Thermoelectric
FoM	Figure of Merit
IoT	Internet of things
MEMS	Microelectromechanical System
CVD	Chemical Vapor Deposition
CMOS	Complementary Metal-Oxide-Semiconductor
DIW	Direct Ink Writing
RT	Room Temperature
DPI	Drop Per Inch
TPI	Threads Per Inch
LUMO	Lowest Unoccupied Molecular Orbital
FF	Fill Factor
PCB	Printed Circuit Board
NIST	National Institute of Standards and Technology
IV	Current-Voltage
MPPT	Maximum Power Point Tracking
COST	Commercially available off-the-shelf
CR	Conversion Ratio
PF	Power Factor

Materials

PEDOT:PSS	Poly(3,4-ethylenedioxythiophene): poly(styrenesulfonic acid)
PEDOT:Tos	Poly(3,4-ethylenedioxythiophene):tosylate
P3HT	Poly(3-hexylthiophene)
Ag	Silver
PBFDO	Poly(benzodifurandione)
CNT	Carbon nanotube
TMQ	Tetramethylquinone
H-BDFO	3,7-dihydrobenzo[1,2-b:4,5-b′]difuran-2,6-dione
DMSO	Dimethyl sulfoxide
Ag_2Se	Silver selenide
Cu_2Se	Copper selenide
$Bi_2Te_{2.7}Se_{0.3}$	Bismuth tellurium selenide
$Bi_{0.5}Sb_{1.5}Te_3$	Bismuth antinomy telluride

References

1. Hassan, Q. *et al.* The renewable energy role in the global energy transformations. *Renewable Energy Focus* **48**, 100545 (2024).
2. Arto, I., Capellán-Pérez, I., Lago, R., Bueno, G. & Bermejo, R. The energy requirements of a developed world. *Energy for Sustainable Development* **33**, 1–13 (2016).
3. Helmers, H. *et al.* Advancing solar energy conversion efficiency to 47.6% and exploring the spectral versatility of III-V photonic power converters. in *Physics, Simulation, and Photonic Engineering of Photovoltaic Devices XIII* (eds. Freundlich, A., Hinzer, K., Collin, S. & Sellers, I. R.) 36 (SPIE, 2024). doi:10.1117/12.3000352.
4. Tabak, A., Safaei, B., Memarzadeh, A., Arman, S. & Kizilors, C. An Extensive Review of Piezoelectric Energy-Harvesting Structures Utilizing Auxetic Materials. *Journal of Vibration Engineering & Technologies* **12**, 3155–3192 (2024).
5. Ali, A. *et al.* Advancements in piezoelectric wind energy harvesting: A review. *Results in Engineering* **21**, 101777 (2024).
6. Firth, A., Zhang, B. & Yang, A. Quantification of global waste heat and its environmental effects. *Appl Energy* **235**, 1314–1334 (2019).
7. Kumar, A. & Rakshit, D. A critical review on waste heat recovery utilization with special focus on Organic Rankine Cycle applications. *Clean Eng Technol* **5**, 100292 (2021).
8. Jiménez-García, J. C., Ruiz, A., Pacheco-Reyes, A. & Rivera, W. A Comprehensive Review of Organic Rankine Cycles. *Processes* **11**, 1982 (2023).
9. Li, Y. *et al.* Recent development in structural designs and thermal enhancement technologies of thermoelectric generator with different types of heat sources: A review. *e-Prime - Advances in Electrical Engineering, Electronics and Energy* **4**, 100180 (2023).
10. Jaziri, N. *et al.* A comprehensive review of Thermoelectric Generators: Technologies and common applications. *Energy Reports* **6**, 264–287 (2020).
11. Dhawan, R. *et al.* Si0.97Ge0.03 microelectronic thermoelectric generators with high power and voltage densities. *Nat Commun* **11**, 4362 (2020).
12. Hu, G., Edwards, H. & Lee, M. Silicon integrated circuit thermoelectric generators with a high specific power generation capacity. *Nat Electron* **2**, 300–306 (2019).

13. Soman, K. Design and Development of a MEMS Stacked Thermoelectric Microwatt Generator. in *2018 3rd International Conference On Internet of Things: Smart Innovation and Usages (IoT-SIU)* 1–5 (IEEE, 2018). doi:10.1109/IoT-SIU.2018.8519925.

14. Yan, J., Liao, X., Ji, S. & Zhang, S. MEMS-Based Thermoelectric–Photoelectric Integrated Power Generator. *Journal of Microelectromechanical Systems* **28**, 1–3 (2019).

15. Kamyshny, A. & Magdassi, S. Conductive Nanomaterials for Printed Electronics. *Small* **10**, 3515–3535 (2014).

16. Huang, Q. & Zhu, Y. Printing Conductive Nanomaterials for Flexible and Stretchable Electronics: A Review of Materials, Processes, and Applications. *Adv Mater Technol* **4**, 1800546 (2019).

17. Kwon, K.-S. *et al.* Review of digital printing technologies for electronic materials. *Print. Electron.* **5**, 043003 (2020).

18. Jun, H.-Y., Kim, S.-J. & Choi, C.-H. Ink Formulation and Printing Parameters for Inkjet Printing of Two Dimensional Materials: A Mini Review. *Nanomaterials* **11**, 3441 (2021).

19. Pinilla, S., Coelho, J., Li, K., Liu, J. & Nicolosi, V. Two-dimensional material inks. *Nat Rev Mater* **7**, 717–735 (2022).

20. Ren, P. *et al.* Recent advances in inorganic material thermoelectrics. *Inorg Chem Front* **5**, 2380–2398 (2018).

21. Shi, X.-L., Zou, J. & Chen, Z.-G. Advanced Thermoelectric Design: From Materials and Structures to Devices. *Chem Rev* **120**, 7399–7515 (2020).

22. Sarbajna, A., Rösch, A. G., Franke, L., Lemmer, U. & Mallick, M. M. Inorganic-Based Printed Thermoelectric Materials and Devices. *Adv Eng Mater* **25**, 2200980 (2023).

23. Selenium periodic table Royal society of Chemistry. https://www.rsc.org/periodic-table/element/34/selenium.

24. Tellurium periodic table Royal society of Chemistry. https://www.rsc.org/periodic-table/element/52/tellurium.

25. Khan, Y. *et al.* A New Frontier of Printed Electronics: Flexible Hybrid Electronics. *Advanced Materials* **32**, 1905279 (2020).

26. Buga, C. S. & Viana, J. C. A Review on Materials and Technologies for Organic Large-Area Electronics. *Adv Mater Technol* **6**, 2001016 (2021).

27. Corzo, D., Tostado-Blázquez, G. & Baran, D. Flexible Electronics: Status, Challenges and Opportunities. *Frontiers in Electronics* **1**, (2020).

28. Rahmani, H. *et al.* Next-Generation IoT Devices: Sustainable Eco-Friendly Manufacturing, Energy Harvesting, and Wireless Connectivity. *IEEE Journal of Microwaves* **3**, 237–255 (2023).
29. Nisato G., Lupo D. & Rudolf S. *Organic and Printed Electronics: Fundamentals and Applications*. (Jenny Stanford, 2024).
30. Liu, H., Liu, D., Yang, J., Gao, H. & Wu, Y. Flexible Electronics Based on Organic Semiconductors: from Patterned Assembly to Integrated Applications. *Small* **19**, (2023).
31. Scaccabarozzi, A. D. *et al.* Doping Approaches for Organic Semiconductors. *Chem Rev* **122**, 4420–4492 (2022).
32. Tang, H. *et al.* A solution-processed n-type conducting polymer with ultrahigh conductivity. *Nature* **611**, 271–277 (2022).
33. Brunetti, I., Dash, A., Scheunemann, D. & Kemerink, M. Is the field of organic thermoelectrics stuck? *J Mater Res* **39**, 1197–1206 (2024).
34. Scheunemann, D. & Kemerink, M. Thermoelectric properties of doped organic semiconductors. in *Organic Flexible Electronics: Fundamentals, Devices, and Applications* 165–197 (Elsevier, 2020). doi:10.1016/B978-0-12-818890-3.00006-0.
35. Mecholsky, N. A., Resca, L., Pegg, I. L. & Fornari, M. Theory of band warping and its effects on thermoelectronic transport properties. *Phys Rev B* **89**, 155131 (2014).
36. Fritzsche, H. A general expression for the thermoelectric power. *Solid State Commun.* **9**, 1813–1815 (1971).
37. Scheunemann, D. & Kemerink, M. Non-Wiedemann-Franz behavior of the thermal conductivity of organic semiconductors. *Phys Rev B* **101**, (2020).
38. Ziman, J. M. PHONONS. in *Electrons and Phonons* 1–61 (Oxford University Press, 2001). doi:10.1093/acprof:oso/9780198507796.003.0001.
39. Fistul', V. I. Transport Phenomena in Heavily Doped Semiconductors. in *Heavily Doped Semiconductors* 77–205 (Springer New York, Boston, MA, 1969). doi:10.1007/978-1-4684-8821-0_4.
40. Zevalkink, A. *et al.* A practical field guide to thermoelectrics: Fundamentals, synthesis, and characterization. *Appl Phys Rev* **5**, 021303 (2018).
41. N.W. Ashcroft, N. D. M. *Solid State Physics*. (Cengage Learning, 2011).
42. Zuo, G., Abdalla, H. & Kemerink, M. Conjugated Polymer Blends for Organic Thermoelectrics. *Adv Electron Mater* **5**, 1800821 (2019).

43. Dongmin Kang, S. & Jeffrey Snyder, G. Charge-transport model for conducting polymers. *Nat Mater* **16**, 252–257 (2017).

44. Martens, H. C. F. *et al.* Understanding the doping dependence of the conductivity of conjugated polymers: Dominant role of the increasing density of states and growing delocalization. *Phys Rev B* **67**, 121203 (2003).

45. Zuo, G., Abdalla, H. & Kemerink, M. Impact of doping on the density of states and the mobility in organic semiconductors. *Phys Rev B* **93**, 235203 (2016).

46. Ihnatsenka, S., Crispin, X. & Zozoulenko, I. V. Understanding hopping transport and thermoelectric properties of conducting polymers. *Phys Rev B* **92**, 035201 (2015).

47. Schmechel, R. Hopping transport in doped organic semiconductors: A theoretical approach and its application to *p* -doped zinc-phthalocyanine. *J Appl Phys* **93**, 4653–4660 (2003).

48. Rahman, M. A. & Saghir, M. Z. Thermodiffusion or Soret effect: Historical review. *Int J Heat Mass Transf* **73**, 693–705 (2014).

49. Rossella, F., Pennelli, G. & Roddaro, S. Measurement of the Thermoelectric Properties of Individual Nanostructures. *Semiconductors and Semimetals*, **98**, 409–444 (2018).

51. Snyder, G. J. & Snyder, A. H. Figure of merit ZT of a thermoelectric device defined from materials properties. *Energy Environ Sci* **10**, 2280–2283 (2017).

52. Kishore, R. A. & Priya, S. A Review on Low-Grade Thermal Energy Harvesting: Materials, Methods and Devices. *Materials* **11**, 1433 (2018).

53. Singh, R. *et al.* Advancements in thermoelectric materials for efficient waste heat recovery and renewable energy generation. *Hybrid Advances* **5**, 100176 (2024).

54. Sharma, S. & Schwingenschlögl, U. Thermoelectric Response in Single Quintuple Layer Bi2Te3. *ACS Energy Lett* **1**, 875–879 (2016).

55. Sun, F.-H. *et al.* Review of current ZT > 1 thermoelectric sulfides. *Journal of Materiomics* **10**, 218–233 (2024).

56. Bubnova, O. *et al.* Optimization of the thermoelectric figure of merit in the conducting polymer poly(3,4-ethylenedioxythiophene). *Nat Mater* **10**, 429–433 (2011).

57. Bubnova, O., Berggren, M. & Crispin, X. Tuning the thermoelectric properties of conducting polymers in an electrochemical transistor. *J Am Chem Soc* **134**, 16456–16459 (2012).

58. Xuan, Y. *et al.* Thermoelectric properties of conducting polymers: The case of poly(3-hexylthiophene). *Phys Rev B Condens Matter Mater Phys* **82**, 115454 (2010).

59. Glaudell, A. M., Cochran, J. E., Patel, S. N. & Chabinyc, M. L. Impact of the doping method on conductivity and thermopower in semiconducting polythiophenes. *Adv Energy Mater* **5**, 1401072 (2015).

60. Zuo, G., Li, Z., Wang, E. & Kemerink, M. High Seebeck Coefficient and Power Factor in n-Type Organic Thermoelectrics. *Adv Electron Mater* **4**, 1700501 (2018).

61. Rodríguez-Martínez, X. *et al.* On The Thermal Conductivity of Conjugated Polymers for Thermoelectrics. *Adv Energy Mater* **14**, 2401705 (2024).

62. HORATES_ITN. Database of Thermoelectric Data for Organic p- and n-Type Materials, 2024.

63. Dörling, B., Rodríguez-Martínez, X., Álvarez-Corzo, I., Reparaz, J. S. & Campoy-Quiles, M. Soluble alkali-metal carbon nanotube salts for n-type thermoelectric composites with improved stability. *Appl Phys Lett* **118**, 213901 (2021).

64. Kanahashi, K., Pu, J. & Takenobu, T. 2D Materials for Large-Area Flexible Thermoelectric Devices. *Adv Energy Mater* **10**, 1902842 (2020).

65. Hu, G. *et al.* Functional inks and printing of two-dimensional materials. *Chem Soc Rev* **47**, 3265–3300 (2018).

66. Hu, G. *et al.* Black phosphorus ink formulation for inkjet printing of optoelectronics and photonics. *Nat Commun* **8**, 278 (2017).

67. Jafarpour, M., Nüesch, F., Heier, J. & Abdolhosseinzadeh, S. Functional Ink Formulation for Printing and Coating of Graphene and Other 2D Materials: Challenges and Solutions. *Small Science* **2**, 2200040 (2022).

68. Abdolhosseinzadeh, S. *et al.* A Universal Approach for Room-Temperature Printing and Coating of 2D Materials. *Advanced Materials* **34**, 2103660 (2022).

69. Madan, D., Wang, Z., Chen, A., Wright, P. K. & Evans, J. W. High-performance dispenser printed MA p-type Bi0.5Sb 1.5Te3 flexible thermoelectric generators for powering wireless sensor networks. *ACS Appl Mater Interfaces* **5**, 11872–11876 (2013).

70. Chen, A., Madan, D., Wright, P. K. & Evans, J. W. Dispenser-printed planar thick-film thermoelectric energy generators. *Journal of Micromechanics and Microengineering* **21**, 104006 (2011).

71. Madan, D. *et al.* Dispenser printed circular thermoelectric devices using Bi and Bi 0.5Sb1.5Te3. *Appl Phys Lett* **104**, 013902 (2014).

72. Varghese, T. *et al.* Flexible Thermoelectric Devices of Ultrahigh Power Factor by Scalable Printing and Interface Engineering. *Adv Funct Mater* **30**, 1905796 (2020).

73. Madan, D., Wang, Z., Wright, P. K. & Evans, J. W. Printed flexible thermoelectric generators for use on low levels of waste heat. *Appl Energy* **156**, 587–592 (2015).

74. Liu, Y. *et al.* Boron-Doped Single-Walled Carbon Nanotubes with Enhanced Thermoelectric Power Factor for Flexible Thermoelectric Devices. *ACS Appl Energy Mater* **3**, 2556–2564 (2020).

75. Mallick, M. M. *et al.* Ultra-flexible β-Cu2-δSe-based p-type printed thermoelectric films. *Appl Mater Today* **26**, 101269 (2022).

76. Hou, W. *et al.* Fabrication and excellent performances of Bi0.5Sb1.5Te3/epoxy flexible thermoelectric cooling devices. *Nano Energy* **50**, 766–776 (2018).

77. Mallick, M. M. *et al.* Realizing High Thermoelectric Performance of Bi-Sb-Te-Based Printed Films through Grain Interface Modification by an in Situ-Grown β-Cu2-δSe Phase. *ACS Appl Mater Interfaces* **13**, 61386–61395 (2021).

78. Madan, D., Chen, A., Wright, P. K. & Evans, J. W. Printed Se-doped MA n-Type Bi 2Te 3 thick-film thermoelectric generators. *J Electron Mater* **41**, 1481–1486 (2012).

79. We, J. H., Kim, S. J., Kim, G. S. & Cho, B. J. Improvement of thermoelectric properties of screen-printed Bi 2Te3 thick film by optimization of the annealing process. *J Alloys Compd* **552**, 107–110 (2013).

80. Saeidi-Javash, M., Kuang, W., Dun, C. & Zhang, Y. 3D Conformal Printing and Photonic Sintering of High-Performance Flexible Thermoelectric Films Using 2D Nanoplates. *Adv Funct Mater* **29**, 1901930 (2019).

81. Mallick, M. M. *et al.* New frontier in printed thermoelectrics: Formation of β-Ag2Se through thermally stimulated dissociative adsorption leads to high: ZT. *J Mater Chem A Mater* **8**, 16366–16375 (2020).

82. Shin, S. *et al.* High-Performance Screen-Printed Thermoelectric Films on Fabrics. *Sci Rep* **7**, 7317 (2017).

83. Mallick, M. M. *et al.* High-Performance Ag-Se-Based n-Type Printed Thermoelectric Materials for High Power Density Folded Generators. *ACS Appl Mater Interfaces* **12**, 19655–19663 (2020).

84. Feng, J., Zhu, W., Deng, Y., Song, Q. & Zhang, Q. Enhanced Antioxidation and Thermoelectric Properties of the Flexible Screen-Printed Bi2Te3 Films through Interface Modification. *ACS Appl Energy Mater* **2**, 2828–2836 (2019).

85. Madan, D. *High Performance Dispenser Printed Thermoelectric Generators*. PhD thesis, University of California, Berkeley (2013).

86. Wei, J. *et al.* Review of current high-ZT thermoelectric materials. *J Mater Sci* **55**, 12642–12704 (2020).

87. Ledoux, M. & El Hami, A. Heat Transfer 1: The Physics of Conduction. John Wiley & Sons, Ltd. ISBN: 9781119818236 (2021).

88. Yazawa, K. & Shakouri, A. Optimization of power and efficiency of thermoelectric devices with asymmetric thermal contacts. *J Appl Phys* **111**, 024509 (2012).

89. Jouhara, H. *et al.* Thermoelectric generator (TEG) technologies and applications. *International Journal of Thermofluids* **9**, 100063 (2021).

90. Poole, C. P., Farach, H. A., Creswick, R. J. & Prozorov, R. Transport Properties. *Superconductivity* 489–529 (Elsevier, 2007).

91. Goupil, C., Ouerdane, H., Zabrocki, K., Seifert, W., Hinsche, N. F. & Müller, E. Continuum Theory And Modeling of Thermoelectric Elements. (John Wiley & Sons, 2016).

92. Beretta, D., Perego, A., Lanzani, G. & Caironi, M. Organic flexible thermoelectric generators: From modeling, a roadmap towards applications. *Sustain Energy Fuels* **1**, 174–190 (2017).

93. Yazawa, K. & Shakouri, A. Cost-efficiency trade-off and the design of thermoelectric power generators. *Environ Sci Technol* **45**, 7548–7553 (2011).

94. Rösch, A. G., Franke, L., Mallick, M. M. & Lemmer, U. Optimizing printed thermoelectric generators with geometry and processibility limitations. *Energy Convers Manag* **279**, 116776 (2023).

95. Bonnassieux, Y. *et al.* The 2021 flexible and printed electronics roadmap. Flex. Print. Electron. **6**, 023001 (2021).

96. Martins, P. *et al.* Advances in Printing and Electronics: From Engagement to Commitment. *Adv Func Mater* **33**, 2213744 (2023).

97. Larson, R. G. & Rehg, T. J. Spin Coating. In: Liquid Film Coating: Scientific Principles and Their Technological Implications, pp. 709–734 (Springer Netherlands, 1997).

98. Berni, A., Mennig, M. & Schmidt, H. Doctor Blade. In Sol-Gel Technologies for Glass Producers and Users, pp. 89–92 (Springer US, 2004).

99. Shah, M. A., Lee, D. G., Lee, B. Y. & Hur, S. Classifications and Applications of Inkjet Printing Technology: A Review. *IEEE Access* vol. 9 140079–140102 (2021).

100. Dimatix Manuals. Fujifilm. https://www.fujifilm.com/de/en/business/inkjet-solutions/deposition-products/dmp-2850/support.

101. Friedlander, S. & Serre, D. Handbook of Mathematical Fluid Dynamics **1** (Elsevier, 2002).

102. Medina Rodríguez, B. Inkjet and screen printing for electronic applications. PhD thesis, Universitat de Barcelona (2016).

103. Fromm, J. E. Numerical calculation of the fluid dynamics of drop-on-demand jets. *IBM J. Res. Dev.* **28**, 322–333 (1984).

104. Derby, B. Inkjet printing of functional and structural materials: Fluid property requirements, feature stability, and resolution. *Annu Rev Mater Res* **40**, 395–414 (2010).

105. Reis, N. & Derby, B. Ink jet deposition of ceramic suspensions: Modelling and experiments of droplet formation. in *Materials Research Society Symposium - Proceedings* **624**, 65–70 (2000).

106. Zhang, Y. *et al.* Suppression and Utilization of Satellite Droplets for Inkjet Printing: A Review. *Processes* **10**, 932 (2022).

107. An experimental investigation of fluid flow resulting from the impact of a water drop with an unyielding dry surface. *Proceedings of the Royal Society of London. A. Mathematical and Physical Sciences* **373**, 419–441 (1981).

108. Hitchcock, S. J., Carroll, N. T. & Nicholas, M. G. Some effects of substrate roughness on wettability. *J. Mater. Sci.* **16**, 714–732 (1981).

109. Tian, D., Song, Y. & Jiang, L. Patterning of controllable surface wettability for printing techniques. *Chem Soc Rev* **42**, 5184 (2013).

110. Suresh, R. R. *et al.* Fabrication of screen-printed electrodes: opportunities and challenges. *Journal of Materials Science* **56**, 8951–9006 (2021).

111. Zavanelli, N. & Yeo, W. H. Advances in Screen Printing of Conductive Nanomaterials for Stretchable Electronics. *ACS Omega*. **6**, 9344–9351 (2021).

112. Suikkola, J. *et al.* Screen-Printing Fabrication and Characterization of Stretchable Electronics. *Sci Rep* **6**, 25784 (2016).

113. Zhang, Y. *et al.* Ink formulation, scalable applications and challenging perspectives of screen printing for emerging printed microelectronics. *Journal of Energy Chemistry* **63**, 498–513 (2021).

114. Potts, S. J. *et al.* High-speed imaging the effect of snap-off distance and squeegee speed on the ink transfer mechanism of screen-printed carbon pastes. *J Coat Technol Res* **17**, 447–459 (2020).

115. Riemer, D. E. The theoretical fundamentals of the screen printing process. *Microelectron. Int.* **6**, 8–17 (1989).

116. Lin, H. W., Chang, C. P., Hwu, W. H. & Ger, M. Der. The rheological behaviors of screen-printing pastes. *J Mater Process Technol* **197**, 284–291 (2008).

117. Xu, C. & Willenbacher, N. How rheological properties affect fine-line screen printing of pastes: a combined rheological and high-speed video imaging study. *J Coat Technol Res* **15**, 1401–1412 (2018).

118. Yang, C.-Y. *et al.* A high-conductivity n-type polymeric ink for printed electronics. *Nat Commun* **12**, 2354 (2021).

119. Ryan, J. D. *et al.* All-Organic Textile Thermoelectrics with Carbon-Nanotube-Coated n-Type Yarns. *ACS Appl Energy Mater* **1**, 2934–2941 (2018).

120. Shakeel, M. *et al.* A low-cost printed organic thermoelectric generator for low-temperature energy harvesting. *Renew Energy* **167**, 853–860 (2021).

121. Yvenou, E. *et al.* Spray-coated PEDOT:OTf films: thermoelectric properties and integration into a printed thermoelectric generator. *Mater Chem Front* **4**, 2054–2063 (2020).

122. Ferhat, S. *et al.* Organic thermoelectric devices based on a stable n-type nanocomposite printed on paper. *Sustain Energy Fuels* **2**, 199–208 (2018).

123. Dani, I. *et al.* Energy Turnaround: Printing of Thermoelectric Generators. *IFIP Int. Conf. Digital Product and Process Development Systems*, 201–208 (2013).

124. Juntunen, T. *et al.* Inkjet Printed Large-Area Flexible Few-Layer Graphene Thermoelectrics. *Adv Funct Mater* **28**, (2018).

125. Tkachov, R. *et al.* A Printable Paste Based on a Stable n-Type Poly[Ni-tto] Semiconducting Polymer. *Coatings* **9**, 764 (2019).

126. Kee, S., Haque, M. A., Corzo, D., Alshareef, H. N. & Baran, D. Self-Healing and Stretchable 3D-Printed Organic Thermoelectrics. *Adv Funct Mater* **29**, (2019).

127. Søndergaard, R. R., Hösel, M., Espinosa, N., Jørgensen, M. & Krebs, F. C. Practical evaluation of organic polymer thermoelectrics by large-area R2R processing on flexible substrates. *Energy Sci Eng* **1**, 81–88 (2013).

128. Mytafides, C. K., Tzounis, L., Karalis, G., Formanek, P. & Paipetis, A. S. High-Power All-Carbon Fully Printed and Wearable SWCNT-Based Organic Thermoelectric Generator. *ACS Appl Mater Interfaces* **13**, 11151–11165 (2021).

129. Massetti, M. *et al.* Fully direct written organic micro-thermoelectric generators embedded in a plastic foil. *Nano Energy* **75**, 104983 (2020).

130. Ferhat, S. *et al.* Flexible thermoelectric device based on TiS2(HA)x n-type nanocomposite printed on paper. *Org Electron* **68**, 256–263 (2019).

131. Rösch, A. G. *et al.* Fully printed origami thermoelectric generators for energy-harvesting. *npj Flexible Electronics* **5**, 1 (2021).

132. He, R., Schierning, G. & Nielsch, K. Thermoelectric Devices: A Review of Devices, Architectures, and Contact Optimization. *Adv Mater Technol* **3**, 1700256 (2018).

133. Varghese, T. *et al.* High-performance and flexible thermoelectric films by screen printing solution-processed nanoplate crystals. *Sci Rep* **6**, 33135 (2016).

134. Danaei, R. *et al.* Ultrafast Fabrication of Thermoelectric Films by Pulsed Light Sintering of Colloidal Nanoparticles on Flexible and Rigid Substrates. *Adv Eng Mater* **21**, 1800800 (2019).

135. Feng, J. *et al.* Enhanced Electrical Transport Properties via Defect Control for Screen-Printed Bi_2Te_3 Films over a Wide Temperature Range. *ACS Appl Mater Interfaces* **12**, 16630–16638 (2020).

136. Kato, K., Kuriyama, K., Yabuki, T. & Miyazaki, K. Organic-Inorganic Thermoelectric Material for a Printed Generator. *J Phys Conf Ser* **1052**, 012008 (2018).

137. Kim, S. J., We, J. H. & Cho, B. J. A wearable thermoelectric generator fabricated on a glass fabric. *Energy Environ Sci* **7**, 1959 (2014).

138. Madan, D. *et al.* Enhanced Performance of Dispenser Printed MA n-type Bi_2Te_3 Composite Thermoelectric Generators. *ACS Appl Mater Interfaces* **4**, 6117–6124 (2012).

139. Madan, D., Chen, A., Wright, P. K. & Evans, J. W. Dispenser printed composite thermoelectric thick films for thermoelectric generator applications. *J Appl Phys* **109**, 075206 (2011).

140. Pires, A. L. *et al.* Printed Flexible μ-Thermoelectric Device Based on Hybrid Bi $_2$ Te $_3$ /PVA Composites. *ACS Appl Mater Interfaces* **11**, 8969–8981 (2019).

141. Qiu, J. *et al.* 3D Printing of highly textured bulk thermoelectric materials: mechanically robust BiSbTe alloys with superior performance. *Energy Environ Sci* **12**, 3106–3117 (2019).

142. Lee, J. *et al.* Doping-Induced Viscoelasticity in PbTe Thermoelectric Inks for 3D Printing of Power-Generating Tubes. *Adv Energy Mater* **11**, 2100190 (2021).

143. Kim, F. *et al.* Direct ink writing of three-dimensional thermoelectric microarchitectures. *Nat Electron* **4**, 579–587 (2021).

144. Chen, B. *et al.* Flexible thermoelectric generators with inkjet-printed bismuth telluride nanowires and liquid metal contacts. *Nanoscale* **11**, 5222–5230 (2019).

145. Kim, F. *et al.* 3D printing of shape-conformable thermoelectric materials using all-inorganic Bi2Te3-based inks. *Nat Energy* **3**, 301–309 (2018).

146. Zeng, W. *et al.* Defect-engineered reduced graphene oxide sheets with high electric conductivity and controlled thermal conductivity for soft and flexible wearable thermoelectric generators. *Nano Energy* **54**, 163–174 (2018).

147. Saeidi-Javash, M., Kuang, W., Dun, C. & Zhang, Y. 3D Conformal Printing and Photonic Sintering of High-Performance Flexible Thermoelectric Films Using 2D Nanoplates. *Adv Funct Mater* **29**, 1901930 (2019).

148. Lu, Z. *et al.* Fabrication of Flexible Thermoelectric Thin Film Devices by Inkjet Printing. *Small* **10**, 3551–3554 (2014).

149. Burton, M. R. *et al.* 3D Printed SnSe Thermoelectric Generators with High Figure of Merit. *Adv Energy Mater* **9**, 1900201 (2019).

150. Franke, L. *et al.* High Power Density Ag $_2$ Se/Sb $_{1.5}$ Bi $_{0.5}$ Te $_3$ -Based Fully Printed Origami Thermoelectric Module for Low-Grade Thermal Energy Harvesting. *Adv Funct Mater* **34***,* 2403646 (2024)

151. Brunetti, I. *et al.* Fully Screen-Printed, Flexible, and Scalable Organic Monolithic Thermoelectric Generators. *Adv Mater Technol* **9**, 2302058 (2024).

152. Hong, C. T., Kang, Y. H., Ryu, J., Cho, S. Y. & Jang, K. S. Spray-printed CNT/P3HT organic thermoelectric films and power generators. *J Mater Chem A Mater* **3**, 21428–21433 (2015).

153. Wei, Q., Mukaida, M., Kirihara, K., Naitoh, Y. & Ishida, T. Polymer thermoelectric modules screen-printed on paper. *RSC Adv* **4**, 28802–28806 (2014).

154. Jiao, F. *et al.* Inkjet-printed flexible organic thin-film thermoelectric devices based on p- and n-type poly(metal 1,1,2,2-Ethenetetrathiolate)s/polymer composites through ball-milling. *Philos. Trans. R. Soc.* **372**, 20130008 (2014).

155. Andersson, H. *et al.* PEDOT: PSS thermoelectric generators printed on paper substrates. *J. Low Power Electron. Appl.* **9**, 14 (2019).

156. Zhang, Q. H. *et al.* Thermoelectric Devices for Power Generation: Recent Progress and Future Challenges. *Adv Eng Mater* **18**, 194–213 (2016).

157. Masoumi, S., O'Shaughnessy, S. & Pakdel, A. Organic-based flexible thermoelectric generators: From materials to devices. *Nano Energy* **92**, 106774 (2022).

158. Beretta, D., Bruno, P., Lanzani, G. & Caironi, M. Reliable measurement of the Seebeck coefficient of organic and inorganic materials between 260 K and 460 K. *Review of Scientific Instruments* **86**, 075104 (2015).

159. Beretta, D., Massetti, M., Lanzani, G. & Caironi, M. Thermoelectric characterization of flexible micro-thermoelectric generators. *Review of Scientific Instruments* **88**, 015103 (2017).

160. Burns, G. W., Scroger, M. G., Strouse, G. F., Croarkin, M. C. & Guthrie, W. F. Temperature-electromotive force reference functions and tables for the letter-designated thermocouple types based on the ITS-90. *NASA STI/Recon Tech. Rep.* **93**, 31214 (1993).

161. COMSOL. Heat Transfer Module User's Guide (https://doc.comsol.com/5.4/doc/com.com.help.heat/HeatTransferModuleUsersGuide.pdf).

162. COMSOL. How to Simulate Thermoelectric Devices and TECs. (https://www.comsol.com/blogs/how-to-simulate-thermoelectric-devices-and-tecs).

163. MatWeb. Material DuPont™ Kapton® (https://www.matweb.com/search/datasheet_print.aspx?matguid=338573ad1bdf4586aa17fab95f3a57d7)

165. Guermoudi, A. A., Cresson, P. Y., Ouldabbes, A., Boussatour, G. & Lasri, T. Thermal conductivity and interfacial effect of parylene C thin film using the 3-omega method. *Journal of Thermal Analysis and Calorimetry* vol. 145 Preprint at https://doi.org/10.1007/s10973-020-09612-z (2021).

166. Kapton® MT+ High Performance Polyimide Films. DuPont. https://www.dupont.com/electronics-industrial/kapton-mt-plus.html.

167. Shirvanimoghaddam, M. *et al.* Towards a Green and Self-Powered Internet of Things Using Piezoelectric Energy Harvesting. IEEE Access **7**, 94533-94556. (2017).

168. Brunetti, I. *et al.* A Scalable Fully Printed Organic Thermoelectric Generator for Harsh Environments Enabled by a Stable n-type Polymer. *Adv Mater Technol* **10,** 2400968 (2024).

169. Zaia, E. W., Gordon, M. P., Yuan, P. & Urban, J. J. Progress and Perspective: Soft Thermoelectric Materials for Wearable and Internet-of-Things Applications. *Adv Electron Mater* **5**, 11 (2019).

170. Campoy-Quiles, M. Will organic thermoelectrics get hot? *Philos. Trans. R. Soc. A* **377**, 20180352 (2019).

171. Chen, G. *et al.* Electronic Textiles for Wearable Point-of-Care Systems. *Chem Rev* **122**, 3259–3291 (2022).

172. Huang, L., Chen, J., Yu, Z. & Tang, D. Self-Powered Temperature Sensor with Seebeck Effect Transduction for Photothermal–Thermoelectric Coupled Immunoassay. *Anal Chem* **92**, 2809–2814 (2020).

173. Pataki, N. J. *et al.* A Rolled Organic Thermoelectric Generator with High Thermocouple Density. *Adv Funct Mater* **34**, 2400982 (2024).

174. Qi, L. *et al.* Recent Progress in Application-Oriented Self-Powered Microelectronics. *Adv Energy Mater* **13**, 2302699 (2023).

175. Li, Q. *et al.* A Highly Conductive *n* -Type Conjugated Polymer Synthesized in Water. *J Am Chem Soc* **146**, 15860–15868 (2024).

176. Petsagkourakis, I. *et al.* Improved Performance of Organic Thermoelectric Generators Through Interfacial Energetics. *Advanced Science* **10**, 2206954 (2023).

177. Yu, Z.-D. *et al.* High n-type and p-type conductivities and power factors achieved in a single conjugated polymer. *Sci Adv* **9**, eadf3495 (2023).

178. Liu, J. *et al.* N-type organic thermoelectrics: demonstration of ZT > 0.3. *Nat Commun* **11**, 5694 (2020).

179. R. Hinojosa, D. *et al.* Solubilizing Benzodifuranone-Based Conjugated Copolymers with Single-Oxygen-Containing Branched Side Chains. *ACS Appl Polym Mater* **6**, 457–465 (2024).

180. Li, Q. *et al.* Regulation of High Miscibility for Efficient Charge-Transport in n-Doped Conjugated Polymers. *Angewandte Chemie International Edition* **61**, e202200221 (2022).

181. Wang, S. *et al.* A Chemically Doped Naphthalenediimide-Bithiazole Polymer for n-Type Organic Thermoelectrics. *Advanced Materials* **30**, 1801898 (2018).

182. Yuan, D., Liu, W. & Zhu, X. Efficient and air-stable n-type doping in organic semiconductors. *Chem Soc Rev* **52**, 3842–3872 (2023).

183. Ke, Z. *et al.* Highly Conductive and Solution-Processable n-Doped Transparent Organic Conductor. *J Am Chem Soc* **145**, 3706–3715 (2023).

184. 2,5-DIHYDROXY-p-BENZENEDIACETIC ACID. *Organic Syntheses* **26**, 24 (1946).

185. Lei, T., Dou, J.-H., Cao, X.-Y., Wang, J.-Y. & Pei, J. Electron-Deficient Poly(*p* -phenylene vinylene) Provides Electron Mobility over 1 cm ^{2} V $^{-1}$ s $^{-1}$ under Ambient Conditions. *J Am Chem Soc* **135**, 12168–12171 (2013).

186. Seshan, K. Handbook of Thin Film Deposition. (William Andrew, 2012).

187. Craighero, M. *et al.* Poly(benzodifurandione) Coated Silk Yarn for Thermoelectric Textiles. *Advanced Science* **11**, 2406770 (2024).

188. Hwang, J. *et al.* Reductive Doping Inhibits the Formation of Isomerization-Derived Structural Defects in N-doped Poly(benzodifurandione) (n-PBDF). *Angewandte Chemie International Edition* **63**, e202401465 (2024).

189. Scheunemann, D. *et al.* Charge transport in doped conjugated polymers for organic thermoelectrics. *Chemical Physics Reviews* **3**, 021309 (2022).

190. Villalva, D. R., Haque, M. A., Nugraha, M. I. & Baran, D. Enhanced Thermoelectric Performance and Lifetime in Acid-Doped PEDOT:PSS Films Via Work Function Modification. *ACS Appl Energy Mater* **3**, 9126–9132 (2020).

191. Zapata-Arteaga, O. *et al.* Closing the Stability–Performance Gap in Organic Thermoelectrics by Adjusting the Partial to Integer Charge Transfer Ratio. *Macromolecules* **53**, 609–620 (2020).

192. Liu, Y., Villalva, D. R., Sharma, A., Haque, M. A. & Baran, D. Molecular Doping of a Naphthalene Diimide–Bithiophene Copolymer and SWCNTs for n-Type Thermoelectric Composites. *ACS Appl Mater Interfaces* **13**, 411–418 (2021).

193. Zheng, C. *et al.* A Flexible Self-Powered Sensing Element with Integrated Organic Thermoelectric Generator. *Adv Mater Technol* **4**, 1900247 (2019).

194. Joglar, M. et al. Printed TEG based energy harvesting system driven by self-powered low-power oscillator. SSRN Preprint 4890153 (2024). https://doi.org/10.2139/ssrn.4890153.

195. Joglar, M. N. Low-power step-up circuits for energy harvesting. PhD thesis, Universitat Autònoma de Barcelona (2024).

196. Rösch, A. G. Modellierung und Design gedruckter thermoelektrischer Materialien und Generatoren für Energy Harvesting und Abwärmerückgewinnung. PhD thesis, Karlsruhe Institute of Technology (2024).

197. LeBlanc, S., Yee, S. K., Scullin, M. L., Dames, C. & Goodson, K. E. Material and manufacturing cost considerations for thermoelectrics. *Renewable and Sustainable Energy Reviews* **32**, 313–327 (2014).

198. Mallick, M. M. *et al.* High Figure-of-Merit Telluride-Based Flexible Thermoelectric Films through Interfacial Modification via Millisecond Photonic-Curing for Fully Printed Thermoelectric Generators. *Advanced Science* **9**, 2202411 (2022).

199. Kumar, S., Tiwari, P. & Zymbler, M. Internet of Things is a revolutionary approach for future technology enhancement: a review. *J Big Data* **6**, 111 (2019).

200. Analog Devices. LTC3108: Ultralow Voltage Step-Up Converter and Power Manager. https://www.analog.com/media/en/technical-documentation/data-sheets/LTC3108.pdf.

201. Analog Devices. MAX17220: Ultralow Quiescent Current Step-Up DC-DC Converter. https://www.analog.com/media/en/technical-documentation/data-sheets/MAX17220-MAX17225.pdf.

202. Texas Instruments. BQ25504: Ultra Low-Power Boost Converter with Battery Management for Energy Harvester Applications. https://www.ti.com/lit/ds/symlink/bq25504.pdf.

203. Lallart, M., Phung, L. V. & Massot, B. Transformer-Free, Off-the-Shelf Electrical Interface for Low-Voltage DC Energy Harvesting. *IEEE Transactions on Industrial Electronics* **65**, 5580–5589 (2018).

204. Im, J.-P., Wang, S.-W., Ryu, S.-T. & Cho, G.-H. A 40 mV Transformer-Reuse Self-Startup Boost Converter With MPPT Control for Thermoelectric Energy Harvesting. *IEEE J Solid-State Circuits* **47**, 3055–3067 (2012).

205. Reindl, L., Grgić, D., Ungan, T., Kostić, M. & Reindl, L. M. *Ultra-Low Input Voltage DC-DC Converter for Micro Energy Harvesting*. (2009).

206. Adami, S.-E. *et al.* Ultra-Low Power, Low Voltage, Self-Powered Resonant DC–DC Converter for Energy Harvesting. *J Low Power Electron* **9**, 103–117 (2013).

207. Patra, S., Muthe, K. P. & Singh, A. Low Voltage and Low Power Self-Startup Oscillator-Driven Boost Converter for Thermoelectric Generator Operating at Low Temperature. *IEEE Transactions on Industrial Electronics* **71**, 12457–12467 (2024).

208. Degrenne, N. *et al.* A 140 mV Self-Starting 10 mW DC/DC Converter for Powering Low-Power Electronic Devices from Low-Voltage Microbial Fuel Cells. *J Low Power Electron* **8**, 485–497 (2012).

209. Schubert, T. F. & Kim, E. M. Fundamentals of Electronics. (Springer International Publishing, Cham, 2016).

210. Dell'Erba, G. The scale-up of printed electronics is more than just technical challenges. *Nature Reviews Electrical Engineering* **1**, 634–636 (2024).

Acknowledgments

The work presented in this thesis was financially supported by the Marie Skłodowska-Curie Grant Agreement No. 955837 HORATES, which allows 15 Early-Stage Researchers to create a scientific network, collaborating between different fields and countries. I would like to thank the European Union for making this possible.

My sincere gratitude to Prof. Dr. Martijn Kemerink and Dr. Dorothea Scheunemann for organizing this great project and giving me the opportunity to discuss with international and interdisciplinary researchers, it has enriched me in every possible way. Many thanks also to Prof. Dr. Martijn Kemerink for allowing me to join his research group and supervising my research during these years. I will never forget the scientific support and help you gave me.

I am also very grateful to Prof. Dr. Uli Lemmer for accepting me into his thermoelectric group and giving me the opportunity to do this PhD. Thank you for all the supervision and scientific guidance.

I would also like to thank Dr. Mario Caironi for supervising and helping me during my secondment in Milan and later for being a valuable guide when I needed it.

I would like to express my sincere gratitude to Prof. Dr. Gerardo Hernandez-Sosa for welcoming me into his research group and for his advice and bureaucratic support.

Thank you to all the people involved in HORATES, it has been an incredible journey. Special thanks to all the ERS. I will miss our meetings around the world, from the craziest Barcelona to Strasburg karaoke, thank you for all the happy memories I will jealously keep.

The Heidelberg crew was numerous Aditya, Angus, Federico, Nate, Matias, Jiali, Diego, Joost, Shubhradip, I enjoyed every moment with you guys! Thank you for all the scientific discussions, but also for the company and the light-hearted evenings. Grazie Federico per il supporto che mi hai dato all'inizio di questo percorso, in un momento non troppo facile, mi hai aiutata molto, dandomi la forza di continuare. Thank you Adi and Angus, I am really happy that we were all here together, I am waiting for you for an English breakfast, right Angus? Thanks also to the MRS crew Mavi, Qifan, Nate and Diego, it was my first international conference and you made it special, you've made me feel less pressure, and have more fun around Seattle, despite the sleepiness. Grazie Mavi

per le parole di conforto, i lunghi messaggi vocali, A volte basta un pensiero, per risollevarsi un po’, ci vediamo persto in italia!

My secondments in Milan and Barcelona were simply fantastic and that is also thanks to Nate and Matias. Thank you for the scientific collaboration, the support and the company.

Thank you to all my colleagues at the Karlsruhe Institute of Technolog/InnovationLab with whom I have shared wonderful times over the last three years: Rainer, Peter, Ozan, Chris (and Chris 4.0), Luis, Kai, Ali, Johannes, Srikanth, the "Basque infiltrator" Mikel (gracias por leer mi tesis), and the newcomers Uma and Theresa. The fond memories I have of the office and the events with my colleagues will stay with me forever, thank you for all the lunches, long evenings in the clean room and evenings in the pub that you shared with me. Special thanks to Ozan, my coffee/sports mate, and more recently Pizza mate (specifically only from Rossini), you made my days happier. I really appreciated your support, especially during the periods of frustration, and they were a loot. I am looking forward to the Eurolega game, I am waiting for you!

Thanks also to Nassima, the lunches were never boring thanks to you, I will miss our multilingual chats and discussions, I wish you all the best for the next steps, Grazie!

I would like to express my gratitude to my friend Pariya, for your countless help, you simplified and eased all the difficult bureaucratic steps and always supported me when I was a bit down, I wish you the best too, you deserve it.

I'd like to thank the KIT Thermoelectrics Group for the valuable weekly discussions that have contributed to my research perspectives.

I am deeply grateful to my lovely flatmate Sophia, you have become one of my closest friends, you are a fantastic person, thank you for everything, I cannot sum up in a few lines the help you have given me, you have always had a smile on your face despite everything. I couldn't have asked for a better friend, you made every day brighter. I will miss living with you but I will wait for you wherever I go and I will visit you wherever you are. Vielen Dank, meine Liebe.

Non è mai facile vivere lontano da amici e familiari. Vorrei ringraziare tutti i miei amici per i messaggi e il supporto che mi avete dato in questi anni. Tornare a casa e trovare cene in compagnia, risate e chiacchiere senza fine è stato bellissimo. Lo so, adesso siamo un po' tutti sparsi per l'Italia e l'Europa e diventa sempre più complicato vederci tutti insieme, ma è ancora più bello ritrovarci. Siamo cresciuti insieme, molte cose sono cambiate, ma il sorriso che ci scambiamo ad ogni incontro è sempre lo stesso. Grazie per le vacanze che aspettavo con ansia e per l'accoglienza che non mi avete mai fatto mancare.

Un grazie speciale alla mia amica d'infanzia Eugenia, che mi ha spesso offerto un posticino a Parigi, non vedo l'ora di festeggiare con te, sei un tesoro, arrivo presto.

Grazie ai miei ex-colleghi Lorenzo e Silvia, mi avete insegnato molto, non so come avrei fatto senza i vostri consigli.

A mamma e papà, non cel'avrei mai fatta senza di voi, siete un esempio per tutto. Grazie per avermi sempre sostenuta, e capita. Mi avete fatto sentire a casa, anche quando non ero lì. Vi voglio bene.

Ad Adele, la mia sorellina, scusa se non sono stata lì in questi anni, so che ne avevi bisogno, spero che mi perdonerai e spero di poter rimediare presto. Grazie di essere venuta a trovarmi, anche se non è stato facile, e di essere stata con me, sempre.

A Piero, grazie per avermi supportata sempre, nonstante la distanza, delle chiamate ogni giorno, dei pensieri.. grazie per avermi spinta a vivere quest'avventura ed essere stato al mio fianco sempre, delle risate, dei pianti.. Ti ho sentito vicino ogni giorno, spero di esserlo stata anche io, anche solo la metà di quello che sei stato tu. Scusami se non sono potuta tornare così spesso, ci ho provato, ma è sempre stato troppo breve, adesso torno per restare.

Thank you to everyone who crossed paths with me on this journey.